Optical Phase Conjugation and Its Applications in Biology

Thesis by

Mooseok Jang

In Partial Fulfillment of the Requirements

for the Degree of

Doctor of Philosophy

Caltech

California Institute of Technology

Pasadena, California

2016

(Defended May 9, 2016)

ii

Acknowledgements

I would like to thank my advisor, Professor Changhuei Yang. His guidance has been essential to my development as a scientist. I have been able to learn diverse aspects of biophotonics from his extensive insight and knowledge. The lessons I learned from him are not only bound to science. He has patiently taught me the importance of communication and diligence, which I had not realized earlier. I expect the values that I have learned from him will stay with me throughout my future career.

I would also like to thank my thesis committee members Professor Amnon Yariv, Professor P. P. Vaidyanathan, Professor Viviana Gradinaru, and Professor Ivo M. Vellekoop. Their advice and support has been invaluable in guiding me through the doctoral program. In particular, it was my honor to have three researchers - Professor Amnon Yariv, Professor Changhuei Yang, and Professor Ivo M. Vellekoop - who have made major contributions in the development of my research field.

Haowen Ruan has been a wonderful lab mate. He and I have worked as a team on several of the projects presented in this thesis. Throughout the collaborations, he has been a great teacher, especially in his ultrasound expertise. I have realized through my work with him that research becomes more enjoyable with a good friend. I also thank Ivo M. Vellekoop for providing great insights during our collaboration. My scientific interactions with him were one of my greatest joys during my graduate study.

The collaboration with the team at Gwangju Institute of Science and Technology has been very fruitful as well. Professor Euiheon Chung and Taejoong Eom have been supportive of pursuing new directions and provided essential guidance to implement the ideas. Jihee Ryu and Yeonsu Jung have been a great addition to the team.

Abstract

Optical phase conjugation is a process where an incoming electromagnetic wave is reflected with a reversed phase. The propagation direction of an incoming beam (equivalently, local phase gradient) can thereby be precisely reversed by the phase conjugate beam. This intriguing effect, so called "time-reversal of electromagnetic waves," allows cancellation of spatial distortion introduced into the incoming beam. Recently, this concept has provided a new avenue to overcome or utilize random scattering in the field of biophotonics.

This thesis discusses a number of interrelated topics regarding optical phase conjugation and its applications in biology. First, two examples of exploiting optical phase conjugation for light focusing are presented. The first example shows that the axial resolution can be improved based on the counter-propagating property of the phase-conjugate beam, and the second example demonstrates how the random scattering media can be used to enhance the flexibility in focusing range. We then discuss a new class of techniques that involves the use of guidestars in the phase conjugation process for deep tissue ($> 1\,\mathrm{mm}$) light focusing and imaging. In the context of *in vivo* application, we model and estimate the penetration depth limit of one prominent example of this approach, time-reversed ultrasonically encoded (TRUE) optical focusing. Based on the analysis, we show that the iteration of phase conjugation operation can improve the contrast and resolution of the focal spot created inside deep tissue. We also present a new kind of guidestar-assited method, time-reversed ultrasound microbubble encoded (TRUME) light focusing, which can focus light with sub-ultrasound wavelength resolution. At last, the effect of dynamic scatterers on time-reversal fidelity is studied to explore the possibility of applying the

optical phase conjugation techniques in living tissue.

Published Content and Contributions

Jang, M.*, Ruan, H.*, Zhou, H., Judkewitz, B. & Yang, C. Method for auto-alignment of digital optical phase conjugation systems based on digital propagation. Opt. Express 22, 14054 (2014). DOI: 10.1364/OE.22.014054.

*: equal contributions. MJ contributed to developing the idea, implementing the auto-alignment algorithm, designing and conducting the experiments, analyzing the experimental results, and preparing the manuscript.

Jang, M., Sentenac, A. & Yang, C. Optical phase conjugation (OPC)-assisted isotropic focusing. Opt. Express 21, 8781 (2013). DOI: 10.1364/OE.21.008781.

*: equal contributions. MJ contributed to designing and conducting the experiments, analyzing the experimental results, and preparing the manuscript.

Ryu, J.*, Jang, M.*, Eom, T. J., Yang, C. & Chung, E. Optical phase conjugation assisted scattering lens: variable focusing and 3D patterning. Sci. Rep. 6, 23494 (2016). DOI: 10.1038/srep23494.

*: equal contributions. MJ contributed to developing the idea, designing the experiments, analyzing the experimental results, and preparing the manuscript.

Jang, M., Ruan, H., Judkewitz, B. & Yang, C. Model for estimating the penetration depth limit of the time-reversed ultrasonically encoded optical focusing technique. Opt. Express 22, 5787807 (2014). DOI: 10.1364/OE.22.005787.

MJ contributed to developing the idea, implementing the computational model, analyzing the numerical results, and preparing the manuscript.

Ruan, H.*, Jang, M.*, Judkewitz, B. & Yang, C. Iterative time-reversed ultrasonically encoded light focusing in backscattering mode. Sci. Rep. 4, 7156 (2014). DOI: 10.1038/srep07156.

*: equal contributions. MJ contributed to developing the idea, designing and conducting the experiments, analyzing the experimental results, and preparing the manuscript.

Ruan, H.*, Jang, M.* & Yang, C. Optical focusing inside scattering media with time-reversed ultrasound microbubble encoded light. Nat. Commun. 6, 8968 (2015). DOI: 10.1038/ncomms9968.

*: equal contributions. MJ contributed to developing the idea, designing and conducting the experiments, analyzing the experimental results, and preparing the manuscript.

Jang, M.*, Ruan, H.*, Vellekoop, I. M., Judkewitz, B., Chung, E. & Yang, C. Relation between speckle decorrelation and optical phase conjugation (OPC)-based turbidity suppression through dynamic scattering media: a study on in vivo mouse skin. Biomed. Opt. Express 6, 72 (2014). DOI: 10.1364/BOE.6.000072.

*: equal contributions. MJ contributed to developing the idea, deriving the theoretical relations, designing and conducting the experiments, analyzing the experimental results, and preparing the manuscript.

Contents

List of Figures

Chapter 1

Introduction

The scattering of electromagnetic radiation is a physical process where localized non-uniformities in a media causes the radiation to deviate from its incident path. Biological tissue is composed of cells and sub-cellular structures sized at sub-microns to tens of microns, and thus is highly non-uniform. In the visible spectrum, the average distance between scattering events is 10–100 microns. As the scattering characteristic of biological tissue restricts the utility of conventional optical techniques to superficial layers ($< 1\,\mathrm{mm}$), it has long been considered one of the biggest challenges in the field of biomedical optics.

We start this chapter with a review of the basic theories of electromagnetic radiation and light-tissue interaction. We describe the scattering and absorption characteristics of different kinds of electromagnetic radiation in tissue and discuss existing optical tools in the area of biomedicine. Then, we provide some essential mathematical tools for understanding and modeling the electromagnetic field propagation through scattering media. Finally, we describe a new approach to tackle the problem of scattering, which will be discussed in detail through the subsequent sections.

1.1 Electromagnetic Radiation

Electromagnetic fields can be described by a set of partial differential equations, called Maxwell's equations. The space and time derivatives of the electric and magnetic field are interrelated in a manner expressed in the following divergence and curl

equations [1–3]:

$$\nabla \cdot \mathbf{E} = \frac{\rho}{\epsilon},$$

$$\nabla \cdot \mathbf{B} = 0,$$

$$\nabla \times \mathbf{E} = -\frac{\partial \mathbf{B}}{\partial t}, \tag{1.1}$$

$$\nabla \times \mathbf{B} = \mu \left(\mathbf{J} + \epsilon \frac{\partial \mathbf{E}}{\partial t} \right),$$

where $\mathbf{E}$ is the electric field, $\mathbf{B}$ is the magnetic field, ρ is the electric charge density, $\mathbf{J}$ is the electric current density, ϵ and μ are the permittivity and permeability of the media. Assuming the medium is uniform (ϵ and μ are uniform over space) and the medium is nonconducting and free from charge ($\mathbf{J} = 0$ and $\rho = 0$), Maxwell's equations simplify to the following form:

$$\nabla \cdot \mathbf{E} = 0,$$

$$\nabla \cdot \mathbf{B} = 0,$$

$$\nabla \times \mathbf{E} = -\frac{\partial \mathbf{B}}{\partial t}, \tag{1.2}$$

$$\nabla \times \mathbf{B} = \mu\epsilon \frac{\partial \mathbf{E}}{\partial t}.$$

Then, the wave equation can be derived by the vector identity $\nabla \times (\nabla \times \mathbf{E}) = \nabla(\nabla \cdot \mathbf{E}) - \nabla^2 \mathbf{E}$ as follows:

$$\nabla^2 \mathbf{E} = \mu\epsilon \frac{\partial^2 \mathbf{E}}{\partial^2 t} = \frac{1}{v^2} \frac{\partial^2 \mathbf{E}}{\partial^2 t},$$

$$\nabla^2 \mathbf{B} = \mu\epsilon \frac{\partial^2 \mathbf{B}}{\partial^2 t} = \frac{1}{v^2} \frac{\partial^2 \mathbf{B}}{\partial^2 t}, \tag{1.3}$$

where $v = 1/\sqrt{\mu\epsilon}$ is the propagation speed of the electromagnetic wave. Because the different components (e.g. E_x and E_y) of the field vectors in Cartesian coordinates are not coupled, wave equations can be expressed with a complex scalar function $\psi(\mathbf{r}, t)$ which is a solution of the scalar analog of Eq. (1.3):

$$\nabla^2 \psi(\mathbf{r}, t) = \frac{1}{v^2} \frac{\partial^2 \psi(\mathbf{r}, t)}{\partial^2 t}. \tag{1.4}$$

Assuming the wave function $\psi(\mathbf{r}, t)$ is time-harmonic (i.e. $\psi(\mathbf{r}, t) = A(\mathbf{r}) \exp(-iwt)$), we obtain the Helmholtz equation, which is also referred as the time-independent form of the wave equation:

$$\nabla^2 A(\mathbf{r}) + k^2 A(\mathbf{r}) = 0, \tag{1.5}$$

where $k \equiv \frac{w}{v}$. It can be easily verified that the plane wave $A(\mathbf{r}) = A_{\mathbf{k}} \exp(i\mathbf{k} \cdot \mathbf{r})$, where $|\mathbf{k}| = k$, is a solution of the Helmholtz equation. Thus, in a homogeneous medium, a plane wave can propagate through an entire space (i.e. for any $\mathbf{r}$) without any deviation from its straight trajectory.

A solution of Eq. (1.4) can be expressed as a linear combination of plane waves $\psi(\mathbf{r}, t) = A_{\mathbf{k}} \exp[i(\mathbf{k} \cdot \mathbf{r} - wt)]$ in every propagation direction. The coefficient $A_{\mathbf{k}}$ depends on the initial and boundary conditions of the wave. k is known as the wave number, which is the reciprocal of the wavelength (λ, the distance for one complete cycle). w is known as the angular frequency, which is the reciprocal of the period (T, the time for one complete cycle).

Electromagnetic radiation is classified into radio waves, microwave, infrared, visible (light), ultraviolet, X-rays, and gamma rays by its wavelength (λ) or oscillating frequency ($\frac{w}{2\pi}$). The wavelength spans from subpicometer to hundreds of megameters and the oscillating frequency ranges from several hertz to hundreds of exahertz (Shown in Fig. 1.1).
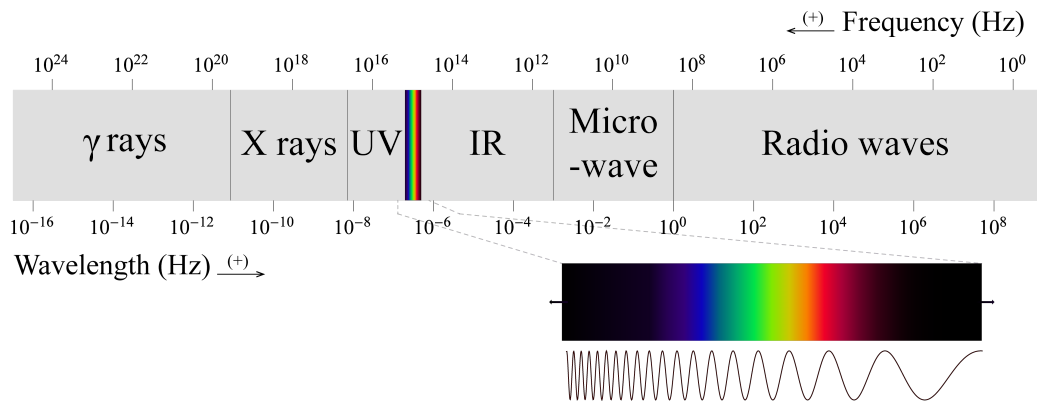
Figure 1.1: The electromagnetic spectrum

1.2 Light-Tissue Interaction

1.2.1 Interaction between Electromagnetic Radiation and Matter

The atomic and molecular energy levels are quantized. If a photon energy matches the energy spacings in between the quantized levels, the photon can be absorbed and excite the molecule into a higher energy state. In the visible spectrum, photon energy ranges from $1\,\mathrm{eV}$ to $3\,\mathrm{eV}$, which typically corresponds to the energy spacing of electrons in different principal energy levels (may be thought as an orbital shell).
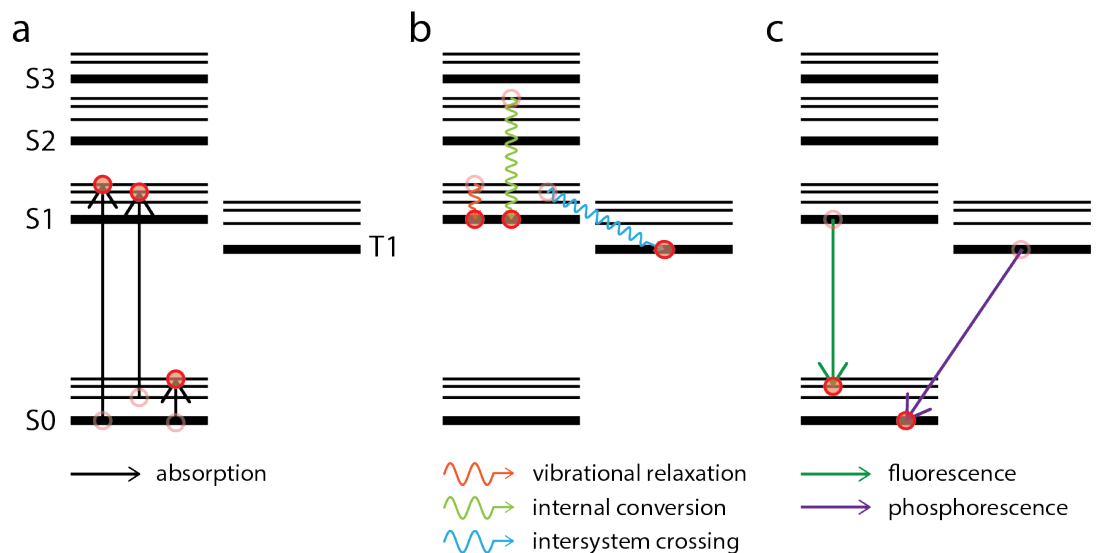
Figure 1.2: Jablonski diagram and possible transitions between energy levels. (a) Absorption transitions. (b) Non-radiative relaxation processes. (c) Radiative relaxation processes.

The energy transfer from photon to molecule can be generally illustrated by a Jablonski diagram where the electronic states of the molecule are arranged along the vertical axis (shown in Fig. 1.2) [4]. Each horizontal line represents the quantized energy states for a particular molecule. Bold horizontal lines and thin horizontal lines represent the principal and vibrational energy levels respectively. There are actually a massive number of possible vibrational modes and each vibrational mode can be divided into a smaller energy spacing which corresponds with the quantum states of

molecular rotation and torsion. However, typical Jablonski diagrams present several representative states for clarity.

The majority of molecules occupy low energy states at room temperature. The Boltzmann distribution ($\propto \exp(-E/kT)$) states that molecules prefer the lower energy states. Thus, when the electromagnetic radiation is absorbed, the molecules are typically excited from these low lying levels to higher electronic or vibrational states. The absorption process is a very fast transition, which takes around 10^{-15} seconds.

The excited molecules can relax down to lower energy states either through radiative or non-radiative processes. Non-radiative transitions are indicated by squiggly arrows and radiative transitions by straight arrows. The following summarizes the relaxation processes:

(1) Non-radiative processes include vibrational relxation, internal conversion, and intersystem crossing. Vibrational relaxation is the process where the excited molecule undergoes a transition into its lower vibrational or rotational energy levels in the same principal energy levels. This is very fast process that happens in 10^{-11} to 10^{-14} seconds. Internal conversion is the transition between principal energy levels in the same spin multiplicity. The internal conversion occurs in the same time scale as vibrational relaxation. Therefore, the two relaxation processes are very likely ways for molecules to dissipate energy. Intersystem crossing, which is one of the slowest transitions (10^{-8} to 10^{-3} seconds) in the Jablonski diagram, is the process involving a transition between two electronic states with different spin multiplicity.

(2) Radiative processes include fluorescence and phosphorescence. Both processes are pathways involving emission of photons in the course of relaxation. Florescence is the transition between states with the same spin mulitiplicity. Because it is a slow process (10^{-9} to 10^{-7} seconds), it mostly happens when the molecules relax from the first principal states to the ground states (as the internal conversion associated with the transition happens in a relatively longer time period so that the fluorescence process can compete). Similarly, phosphorescence is a radiative transition, but from an excited triplet state to a singlet ground state. As it involves a forbidden transition as an intersystem crossing, it takes a long time (10^{-4} to 10^{-1} seconds). In intact

biological tissue, the most common electronic relaxation mechanism is radiationless transitions such as vibrational relaxation and internal conversion.

In addition, there are non-resonant forms of interaction between radiation and molecule which do not involve energy matching. One is elastic (Rayleigh) scattering and the other is Raman (inelastic) scattering. In most cases, molecules act as a simple dipole and re-emit the electromagnetic radiation with the same frequency as it had when it was received. However, in Raman scattering, the molecule is excited by the radiation energy such as in the fluorescence process. The difference is that the molecule is excited to virtual states (not the stationary states related with a particular principal energy level) and relaxes to the ground states which have either higher or lower energy than the original vibrational states (almost instantaneously). Thus, the radiation energy is either lower (Stokes scattering) or higher (anti-Stokes scattering) than the energy of the original radiation. As different molecules have different energy spacings in their ground states, the Raman scattering process is often used to identify the molecular composition of substances.

1.2.2   Light Absoprtion in Biological Tissue

Photon energy of visible light ranges from $1\,\text{eV}$ to $3\,\text{eV}$, which typically corresponds with the energy spacing of electrons in different principal energy levels. The radiation energy is not enough to cause ionization.

In biological tissue, the primary sources of absorption are water, hemoglobin (oxygenated and deoxygenated), melanin, and fat. Different components have different absorption spectra [5, 6]. For example, water has a absorption peak in the infrared region, but hemoglobin has its absorption peak in the violet wavelengths.

A bulky absorptive material can be characterized with a macroscopic quantity called the absorption coefficient (μ_a). Assuming a single light absorber has a geometric cross-section of σ_g and the light is propagating along z-axis, the light attenuation

through a thin slab of media (thickness of dz) is given by

$$I(z + dz) - I(z) = -n_a Q_a \sigma_g dz$$
$$= -N_a \sigma_a dz \qquad (1.6)$$
$$= -\mu_a dz,$$

where σ_a is the absorption cross section and N_a is the number density of absorbers. Here, μ_a is defined as $N_a \sigma_a$. Q_a is absorption efficiency, the ratio between the effective absorption cross section and the geometric cross section. Assuming the light intensity of I_0 at $z = 0$, integration of Eq. (1.6) leads to

$$I(z) = I_0 \exp(-\mu_a z). \qquad (1.7)$$

1.2.3 Light Scattering in biological tissue

A non-absorptive heterogeneous dielectric medium can be expressed by a spatially varying permittivity:

$$\epsilon(\mathbf{r}) = \bar{\epsilon} + \delta\epsilon(\mathbf{r}), \qquad (1.8)$$

where $\bar{\epsilon}$ is an average permittivity, $\delta\epsilon(\mathbf{r})$ is a fluctuation, and $\epsilon(\mathbf{r})$ is real and positive. Then, through the derivation used in Eq. (1.2) – (1.5), the wave equation is given by

$$\nabla^2 A(\mathbf{r}) + k^2 A(\mathbf{r}) = -k^2 \zeta(\mathbf{r}) A(\mathbf{r})$$
$$= V(\mathbf{r}) A(\mathbf{r}), \qquad (1.9)$$

where $\zeta(\mathbf{r}) = \delta\epsilon(\mathbf{r})/\bar{\epsilon}$ and $k \equiv w/v = w/\sqrt{\mu\bar{\epsilon}}$. $V(\mathbf{r})$ $(\equiv -k^2 \zeta(\mathbf{r}))$ plays a role similar to the disordered potential in the Schrödinger equation. The plane wave solution obtained for the Helmholtz equation in a homogeneous medium is no longer a solution of Eq. (1.8). The solution of Eq. (1.9) can be obtained from the associated free Green function $G_0(\mathbf{r}, \mathbf{r}', k)$ defined by

$$\left(\nabla^2 A(\mathbf{r}) + k^2 \right) G_0(\mathbf{r}, \mathbf{r}', k) = \delta(\mathbf{r} - \mathbf{r}'). \qquad (1.10)$$

The solution perturbed by the random permittivity fluctuation can be written as [7]

$$A_{\mathbf{k}}(\mathbf{r}) = \exp\left(i\mathbf{k} \cdot \mathbf{r}\right) + \int G_0(\mathbf{r}, \mathbf{r}', k)V(\mathbf{r}')A_{\mathbf{k}}(\mathbf{r}')d\mathbf{r}'. \tag{1.11}$$

This solution can be expressed in a form of a perturbative expansion:

$$
\begin{aligned}
A_{\mathbf{k}}(\mathbf{r}) = {} & \exp\left(i\mathbf{k} \cdot \mathbf{r}\right) + \int G_0(\mathbf{r}, \mathbf{r}', k)V(\mathbf{r}')\exp\left(i\mathbf{k} \cdot \mathbf{r}'\right)d\mathbf{r}' \\
& + \int\int G_0(\mathbf{r}, \mathbf{r}', k)V(\mathbf{r}')G_0(\mathbf{r}', \mathbf{r}'', k)V(\mathbf{r}'')\exp\left(i\mathbf{k} \cdot \mathbf{r}''\right)d\mathbf{r}'d\mathbf{r}'' \\
& + \cdots
\end{aligned}
\tag{1.12}
$$

The first, second, and third terms on the right side of Eq. (1.12) are the decomposition of the total wave field into an unperturbed, single-scattered, double-scattered wave. As $V(\mathbf{r})$ is randomly fluctuating over space, the scattered terms on the right side of Eq. (1.12) are random, and thus the resultant perturbed field $A_{\mathbf{k}}(\mathbf{r})$ is random.

Scattering in tissues can be largely attributed to the heterogeneity $V(\mathbf{r})$ due to the nuclei and sub-cellular content. The lipid bilayer, which comprises membranes of cells and numerous sub-cellular structures, plays an important role in light scattering inside tissues. It has a refractive index of ~ 1.48 which is significantly higher than that of cytoplasm (refractive index of $\sim$1.37) and extracelullar fluid (refractive index of $\sim$1.35). Specifically, the compartments such as mictochondria, golgi apparatus, and endoplsmic reticlum have membrane-folded structures, and will disrupt $V(\mathbf{r})$ in a more complex manner. As a reference, eukaryotic cells average 10–30 microns in diameter, nuclei average 3–10 microns in diameter, and mitochondria average 0.3–0.7 microns in diameter.

A macroscopic scattering property can also be characterized with a quantity called the scattering coefficient (μ_s). Assuming a single light scatterer has a geometric cross-section of σ_g and the light is propagating along the z-axis, the ballistic component of

the light through thin slab of media (thickness of dz) is reduced by

$$
\begin{aligned}
I(z + dz) - I(z) &= -N_s Q_s \sigma_g dz \\
&= -N_s \sigma_s dz \\
&= -\mu_s dz,
\end{aligned}
\tag{1.13}
$$

where σ_s is the scattering cross section and N_s is the number density of scatterers. Here, μ_s is defined as $N_s \sigma_s$. Q_s is scattering efficiency, the ratio of effective scattering cross section to geometric cross section. Assuming the light intensity of I_0 at $z = 0$, integration of Eq. (1.13) leads to the following expression for the ballistic light intensity at $z > 0$:

$$
I(z) = I_0 \exp(-\mu_s z).
\tag{1.14}
$$

Another essential piece of information about scattering events is the scattering phase function, which describes the angular distribution of the scattered light. Typically, a large scatterer (slowly-varying structure) deflects the light in a forward direction and a small scatterer tends to act as a single dipole so that it scatters light in a more isotropic manner. When the scatterer is a perfect sphere, its interaction with an incident plane wave can be analytically solved through Mie theory (based on Maxwell's equation) and the precise scattering phase function can be obtained.

Typically, in the field of biophotonics, the anisotropy coefficient, which is defined as the mean of the cosine of scattering angle, is more widely used to describe the angular deflection from scattering events. It relates the scattering coefficient to the reduced scattering coefficient by the following relation:

$$
\mu'_s = (1 - g)\mu_s.
\tag{1.15}
$$

The inverse of the reduced scattering coefficient is called transport mean free path, the average length over which the direction of propagation of the photon is completely randomized.

1.2.4 Attenuation Coefficient of Electromagnetic Radiation in Tissue
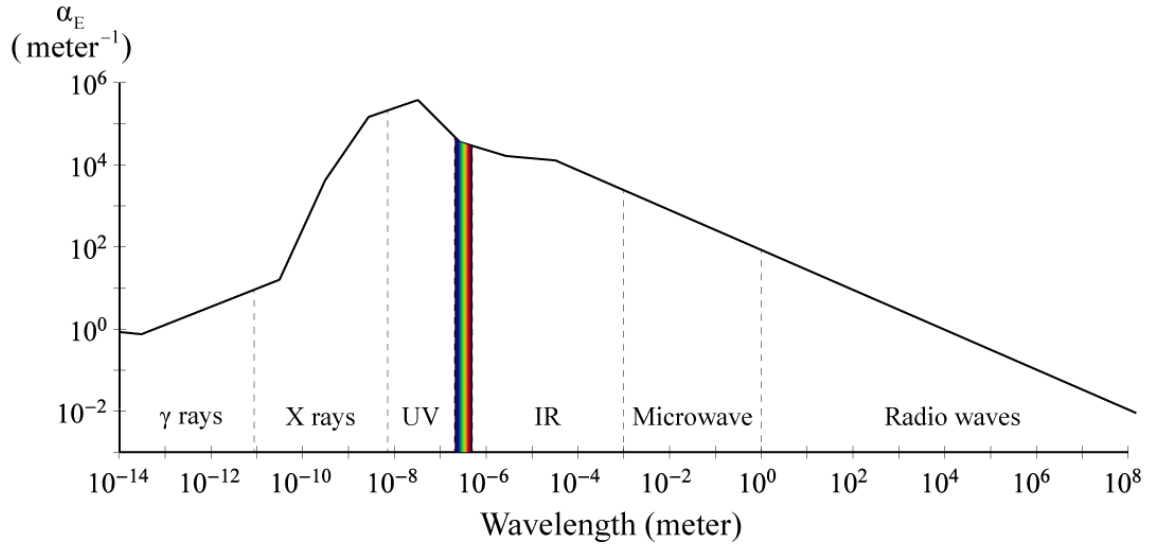
Figure 1.3: Attenuation coefficient of electromagnetic radiation in tissue.

How easily a certain form of electromagnetic wave can penetrate a tissue is character-ized by the attenuation coefficient (μ), the sum of the absorption (μ_a) and scattering (μ_s) coefficients. Assuming the radiation intensity of I_0 at $z = 0$, the unperturbed portion of radiation at $z > 0$,

$$I(z) = I_0 \exp(-\mu z). \tag{1.16}$$

Different classes of electromagnetic radiation have different frequencies, wavelengths, and energies so that they have different amounts of interaction with biological tissue. Radio waves, which are the weakest form of electromagnetic radiation, have a photon energy smaller than $1\,\mu\mathrm{eV}$. Considering the rotational energy states are most closely spaced quantum states and the associated energy spacing is on the order of 0.1–$1\,\mathrm{meV}$, the photon energy of radio waves is not enough to cause a transition in molecular energy levels. Also, as the wavelength is too long to be effectively scattered by tissue, the attenuation coefficient is relatively low.

As the frequency becomes higher in the microwave and infrared regime, the electromagnetic radiation is effectively absorbed by tissue as it is subjected to the dielectric loss through water, and the photon energy is in the range of energies separating the quantum states of molecular vibrations (ranged in $10\,\mu\mathrm{eV}$ – $1\,\mathrm{eV}$). In the visible regime, the absorption by water is dramatically reduced. However, the overall attenuation coefficient is increased as the scattering coefficient is increased. Ultraviolet is strongly absorbed by water as its energy is matched with the energy associated with electronic transition in water molecules. Also, the absorption peak of biological macromolecules such as proteins and nucleic acids are located in the ultraviolet range.

The forms of radiation in higher energy ranges such as X-rays and gamma rays are classified as ionizing radiation, which means that the photon energy is high enough to remove electrons from an atom. X-rays and gamma rays interact with tissues through the photoelectric effect and Compton scattering. While the Compton scattering effect is about constant for different energies, photoelectric absorption has the following dependence on the radiation energy: $(Z/E)^3$, where Z is the atomic number of the composing tissue and E is the photon energy.

Figure 1.3 outlined the overall attenuation spectrum of electromagnetic radiation [8]. The attenuation coefficient in the X-ray and radio wave regime can be as low as $1\,\mathrm{m}^{-1}$. Therefore, X-rays and radio waves can be directly used for deep tissue applications. The most prominent examples are medical imaging methods such as X-ray computed tomography (CT) and magnetic resonance imaging (MRI) [9]. The attenuation coefficient of light is as high as $10^5\,\mathrm{m}^{-1}$. Thus, the conventional optical applications are limited to the superficial layers of biological tissues ($< 1\,\mathrm{mm}$).

However, as the light-tissue interaction is dominated by scattering (the scattering coefficient is two to three orders of magnitude larger than the absorption coefficient), it is in principle possible to directly utilize or manipulate multiply scattered light for deep tissue applications. Optical imaging is useful in biomedical applications as it provides structural and biochemical information about tissue in different dimensions than conventional imaging modalities using X-rays and radio waves [5, 6]. For example, the contrast (or specificity) can be from the absorption spectra, refractive

index map, fluorescence, or Raman scattering. Also, importantly, light is non-ionizing radiation and thus safer than X-rays or gamma rays.

1.3 Speckle and Transmission Matrix

1.3.1 Speckle
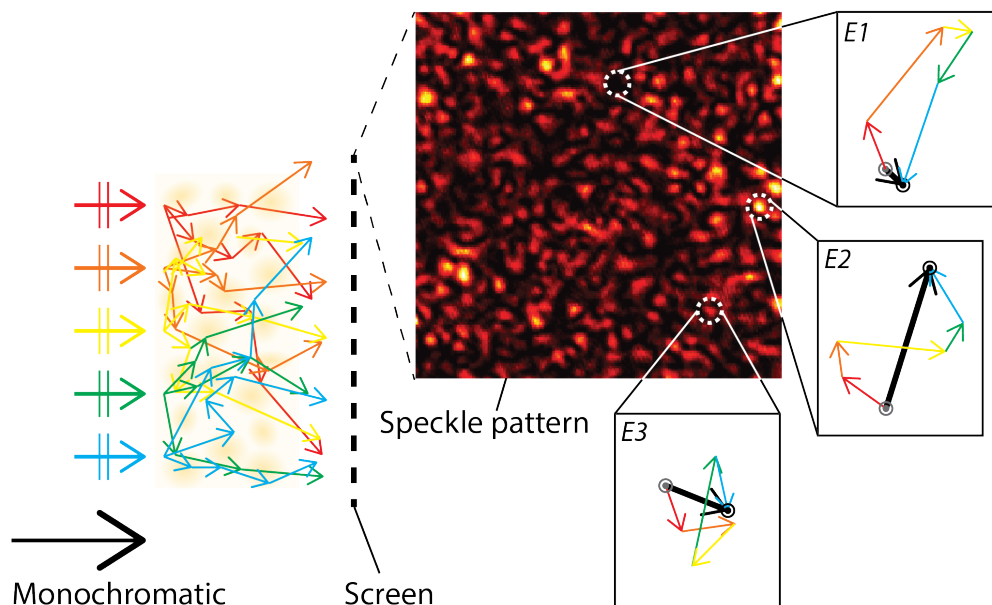
Figure 1.4: Mutual interference of a set of random wavefronts (illustrated with arrows in different colors) results in a random intensity pattern, known as a "speckle pattern" [10]. The output field as different positions can be described as a sum of contributions from different input positions. In the insets ($E1$–$E3$), the independent random contributions are illustrated as a set of random phasors in different colors.

When the light is multiply scattered through the complex medium, a random intensity pattern, known as a "speckle pattern", is produced (shown in Fig. 1.4). It is the result of mutual interference of a set of random wavefronts. Assuming a plane monochromatic light wave propagates through the scattering media, the output field at a specific point behind the scattering media can be decomposed into contributions from the input fields at different incident positions. As each contribution is independently random, the output field can be described as a sum of many random

phasors:

$$E = \sum_{n=1}^{N} a_n e^{i\phi_n}, \tag{1.17}$$

where a_n and ϕ_n are amplitude and phase of n_{th} phasor and N is the number of independent input positions. Assuming N is large, and a_n and ϕ_n are independent of each other and also independent of a_m and ϕ_m for $m \neq n$, the joint probability function for real and imaginary parts of the output field (E) can be approximated as a complex random Gaussian function by the Central Limit Theorem

$$p_{R,I}(R, I) = \frac{1}{2\pi\sigma^2} \exp\left(-\frac{R^2 + I^2}{2\sigma^2}\right), \tag{1.18}$$

where σ is the standard deviation. The probability density function for intensity (I) and phase (θ) is then given by

$$\begin{aligned} p_I(I) &= \frac{1}{2\sigma^2} \exp\left(-\frac{I}{2\sigma^2}\right), \\ p_\theta(\theta) &= \frac{1}{2\pi} \text{ where } -\pi \leq \theta < \pi. \end{aligned} \tag{1.19}$$

Therefore, the intensity follows the Rayleigh distribution and the phase is uniformly distributed over $-\pi$ to π. Intensity and phase are statistically independent.

Speckle size depends on the maximum transverse wave vector (Fourier) component. When the scattering medium is thick enough to completely disturb the direction of photon propagation, speckle size is around a half of the light wavelength.

1.3.2 Transmission Matrix

As the field propagation through a scattering medium is a linear process, the relation between input and output field can be described by matrix multiplication. When a input field ($E_{L,i}$) is incident on the left side of a scattering medium, the output field on the right side can be written as [11–13]

$$E_{R,o} = T_{L\rightarrow R} E_{L,i}. \tag{1.20}$$

Thus, the m_{th} entry of the output field is given by summation of contributions from each input mode:

$$(E_o)_m = \sum_{n=1}^{N} (T)_{mn} (E_i)_n,$$ (1.21)

where N is the number of input modes. Here, for simplicity, the subscripts L and R are dropped. Then, the transmission matrix T can be written as

$$T = U \Sigma V^*$$ (1.22)

by singular value decomposition. U ($M \times M$ matrix where M is the number of output modes) and V (N×N matrix) are composed of columns filled with left- and right-singular vectors. U is a set of orthonormal eigenvectors of TT^* and V is a set of orthonormal eigenvectors of T^*T. Thus, both are complex unitary matrices. Σ is a $M \times N$ diagonal matrix with singular values (square root of the eigenvalues of TT^*) on the diagonal. The operation Eq. (1.20) can be understood as follows. The right-singular vector decomposes the input field defined on the reference coordinate (where the input field is defined) into the eigenmodes propagating through the scattering media. Then, the amplitude transmission coefficients (Σ) are multiplied by each transmitting eigenmode. At last, the left-singular vectors map the transmitted and outgoing eigenmodes into the reference coordinate (where the output field is defined).
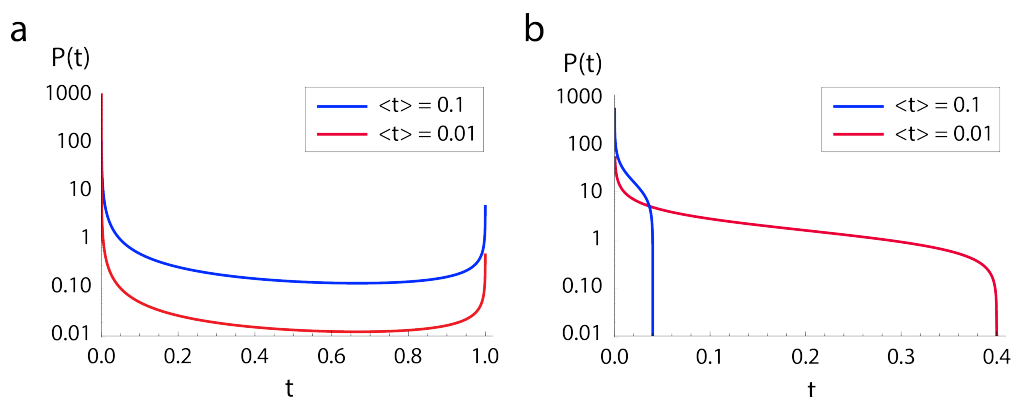
Figure 1.5: Transmission distribution of eigenchannels of disordered media. (a) Through a waveguide geometry. (b) Through a lossy configuration.

The distribution of intensity transmission coefficients (square of the diagonal elements of Σ) depends on the absorption properties of the scattering media and the vector space T is defined on. When the tranmission matrix T is for the scattering medium in the waveguide geometry or the vector space associated with T is large enough to fully describe the field propagation through a scattering media in open space, the total energy conservation condition (with an additional assumption of no absorption) imposes a certain form of correlation between the matrix elements of T. In this case, the transmission coefficient follows the biomodal distribution in the following equational form [14–17]:

$$P(t) = \frac{\langle t \rangle}{2t\sqrt{1-t}} \text{ where } \cosh^{-2}(L/l) \leq t \leq 1, \tag{1.23}$$

where $\langle t \rangle$ is an average transmittance. That is, each eigenchannel is either open ($t = 1$) or closed ($t = 0$) and the probability of the unity and nearly zero transmittance is given as follows:

$$\text{Probability}(t \sim 1) = \frac{\langle t \rangle}{N},$$
$$\text{Probability}(t \sim 0) = 1 - \frac{\langle t \rangle}{N}, \tag{1.24}$$

where N is the number of optical modes in the scattering media. Therefore, the probability of the channel being open becomes lower when the scattering media becomes more turbid (i.e. when $\langle t \rangle$ is reduced). The distribution of transmission coefficients for the case of $\langle t \rangle = 0.1$ and $\langle t \rangle = 0.01$ are shown in Fig. 1.5(a).

The presence of the open channel is hardly observable in reality as the biomodal distribution is derived under the ideal total energy conservation condition [13]. In practical cases where the transmission matrix is characterized in a lossy condition, the transmission matrix components become uncorrelated and follow a complex random Gaussian distribution. Then, the transmittance distribution of eigenchannels takes the quarter circle distribution [13, 18]:

$$P(t) = \frac{4}{R^2\pi}\sqrt{R^2 - t^2} \text{ where } 0 \leq t \leq R, \tag{1.25}$$

where R is $\frac{3\pi}{4}\langle t \rangle$. The channel with the highest transmission would have a transmission value that is only ~ 2.36 times higher than the average. The quarter-circle distribution of transmission coefficients for the case of $\langle t \rangle = 0.1$ and $\langle t \rangle = 0.01$ are shown in 1.5(b).

1.4   Optical Wavefront Shaping Methods

As clearly seen in Eq. (1.20) and (1.21), the scattered light field inside or through a scattering medium can be manipulated by controlling the incident light field. In the past decade, the concept of wavefront shaping and field manipulation has been demonstrated by focusing light inside or through scattering media [12, 19–21]. The methods have been attracting increasing attention as they potentially allow optical imaging inside scattering media (e.g. biological tissue), which has long been considered an impossible task. In this section, we provide a review of devices used for wavefront shaping (including the liquid crystal cell array, deformable mirror, and digital micromirror device) and introduce the concept of time-reversed light propagation.

1.4.1   Spatial Light Modulator

A spatial light modulator is a device used to impose a spatially varying modulation on the beam of incident light [22, 23]. The modulation can be in various forms: amplitude, phase, and polarization. In this subsection, we will review three devices - the liquid crystal cell array, digital micromirror device, and deformable mirror - that are widely used in the field of wavefront shaping.

Liquid crystal phase is characterized by a state between conventional liquid and solid crystal. The molecules in liquid crystal may be aligned and/or oriented like a solid crystal, but have a much greater freedom to move like a liquid. Liquid crystal can be divided into three classes: thermotropic, lyotropic, and metallotropic liquid crystals. These are classified by the condition required for the phase transition. Thermotropic and lyotropic liquid crystals, which are composed of organic molecules, occur in a certain temperature range. While the thermotropic phase is induced merely by

temperature, the lyotropic phase requires a amphiphilic solvent (both hydrophilic and liphphilic) and exhibits a phase-transition controlled by the concentration of the liquid crystal molecule and solvent. In contrast, a metallotropic liquid crystal is composed of both organic and inorganic components and the phase transition depends on the organic-inorganic composition ratio, in addition to temperature and concentration.

In most practical applications, rod-shaped liquid crystal molecules (a sub-category of the thermotropic phase) are used. In the liquid crystal phase, the long axis of the molecules are oriented in a certain direction (director's direction). Typically, several subphases and alignments of liquid crystals are observable by modifying the temperature. For example, in the smectic phase (which can be typically found at relatively lower temperatures), the molecules are arranged in planes such as in a conventional crystal. In contrast, in the nematic phase, the molecules are randomly positioned like a liquid. The nematic phase is most widely used in electrooptical applications as the director's direction can be easily controlled with an electric field.

The operation mode of a liquid crystal-based spatial light modulator depends on the director's direction in the response of the external electric field. Depending on the direction of the permanent or induced dipole moments, the long axis of the liquid crystal molecule can either be aligned along or perpendicular to the direction of the applied electric field. Here, we introduce two types of liquid crystal alignment that can be used to control the phase and amplitude of the light, respectively.

1. Parallel aligned nematic liquid crystal. In the PAN phase, the LC molecules are initially aligned parallel to the two alignment layers where the electrodes are aligned as well. When the electric field is applied, the LC molecules are aligned to the direction of electric field (rotation angle depends on the strength of the electric field). Based on the birefringence of the LC molecule, the phase of the light beam that passes through the LC cell can be modulated.

2. Twisted nematic liquid crystal. This type of LC molecules is aligned in a helical twist. Thus, the first molecule and the last molecule between the alignment layers are perpendicular to each other at the beginning. Therefore, the polarization of the beam is gradually rotated. When the electric field is applied, the polarization angle of

the light beam is no longer rotated by the LC cell as the LC molecules are aligned to the direction of the electric field. By placing the polarizers on the input and output sides of the LC cell, the amplitude modulation can be achieved. This is the working principle of the conventional LCD screen. In the wavefront shaping experiment, it should be taken into account that the phase of the light is also modulated by the bifringence.

A deformable mirror is a reflective surface that can be deformed into a desired shape. Historically, deformable mirrors have been widely used in astronomical telescopes to adaptively compensate the wavefront distortion from the atmosphere, resulting in an improvement on the resolution and brightness of the image [24, 25]. The first successful design was implemented with a thin aluminized glass facesheet bonded to a slab of piezoelectric material. Voltages applied to the electrodes (which are placed underneath the piezoelectric material) imprint the desired local deformation. Alternatively, the continuous facesheet can be supported and deformed by discrete actuators (up to a few thousand). Either piezoelectricity or electrostatic force can be used as an actuator module. The concept of the deformable mirror can also be implemented with segmented mirrors which consist of an array of discrete mirrors. Typically, each mirror is controlled by three actuators for three degrees of freedom in movement: piston and tip/tilt. In contrast to the continuous facesheet design, each of the mirror elements are free of crosstalk. However, the drawback lies in the fact that the gaps between mirror segments generate undesired scattered light.

A digital micromirror device (DMD) is an optical semiconductor composed of 10^5 to 10^6 microscopic mirrors arranged on a CMOS integrated circuit. Each micromirror is attached to the torsional hinge aligned along the diagonal of the mirror. Two electrodes, which are controlled by the CMOS circuit, are used to apply electrostatic force to the mirror elements and hold the micromirrors in the two operational positions (typically, $-10\,^\circ$ and $+10\,^\circ$). A DMD is used to modulate the amplitude of the incident light beam by guiding the light component reflected in either of the angles (referred to as the ON state) into an optical system of interest. In display applications, grayscales are produced by controlling the ratio of ON and OFF time within one frame time of

the human eye.

When choosing a spatial light modulator for a wavefront shaping experiment, a number of parameters, such as the number of degrees of freedom and the response time, should be taken into an account. The number of degrees of freedom determines the complexity of wavefront that the SLM can reproduce and the response time determines the range of applications depending on the dynamic characteristics of the specimen. A typical liquid crystal-based spatial modulator has 10^6–10^7 elements, refreshing at $\sim 60\,\mathrm{Hz}$. A digital micromirror device has a similar number of elements, but can operate at a frequency of up to $\sim 30\,000\,\mathrm{Hz}$. Thus, it is the most suitable for fast applications. A deformable mirror typically has a 10–1000 elements, operating at $\sim 1000\,\mathrm{Hz}$.

1.4.2 Time-reversed Light Propagation

The problem of scattering can be overcome by wavefront shaping techniques. More specifically, an SLM can be used to generate a phase-conjugated beam which propagates the scattering media in a time-reversed fashion. In this section, we introduce the concept of optical phase conjugation and time-reversed light propagation.

Optical phase conjugation is a process in which the incident optical wavefront is reproduced with a conjugated phase and back-propagated into the direction of incidence. From the Eq. (1.9), where inhomogeneity $\epsilon(\mathbf{r})$ is assumed, the complex amplitude $A(\mathbf{r})$ of the paraxial forward-propagating $(+z)$ wave $(E(\mathbf{r}, t) = A(\mathbf{r}) \exp(wt - kz))$ obeys the following equation [26]:

$$\nabla^2 A(\mathbf{r}) + \left[w^2 \mu \epsilon(\mathbf{r}) - k^2 \right] A(\mathbf{r}) - 2ik \frac{\partial A(\mathbf{r})}{\partial z} = 0. \tag{1.26}$$

Taking the complex conjugate of Eq. (1.26), we get

$$\nabla^2 A^*(\mathbf{r}) + \left[w^2 \mu \epsilon(\mathbf{r}) - k^2 \right] A^*(\mathbf{r}) + 2ik \frac{\partial A^*(\mathbf{r})}{\partial z} = 0, \tag{1.27}$$

assuming lossless medium ($\epsilon(\mathbf{r})$ is real). Equation (1.27) is the same as the wave

equation (Eq. (1.9)) with the phase conjugated copy of $E(\mathbf{r}, t)$ propagating in the reverse direction:

$$E_{\mathrm{pc}}(\mathbf{r}, t) = aA^*(\mathbf{r}) \exp(wt + kz), \tag{1.28}$$

where a is an arbitrary constant. Therefore, if we generate and propagate back the phase conjugate field, its amplitude will remain the complex conjugate of $A(\mathbf{r})$ (which is of the original wave) at each $\mathbf{r}$. That is, the wavefront distortion caused by the inhomogeneity can be rewound in reverse order (referred to as a "time-reversed" manner) so that the original field amplitude distribution can be perfectly restored (as shown in Fig. 1.6).
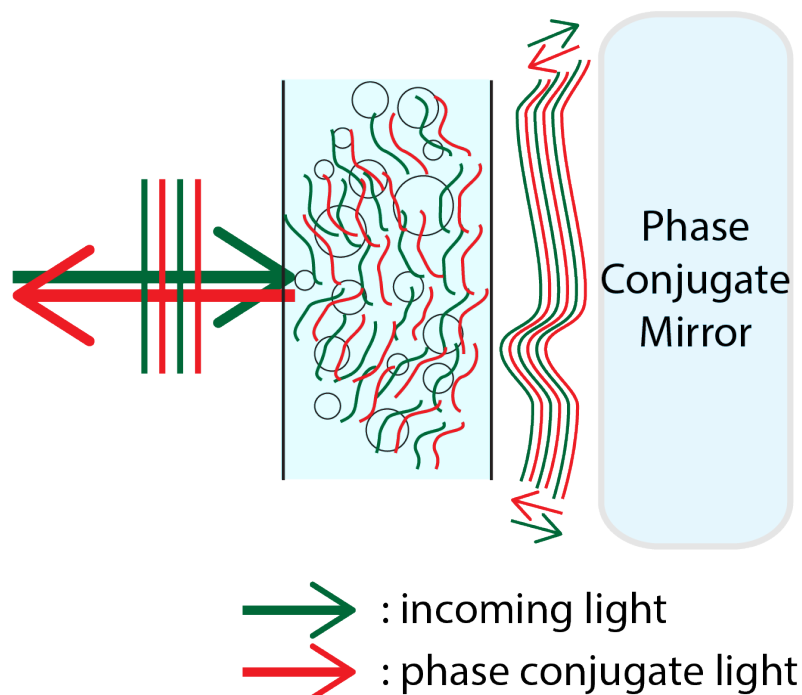
Figure 1.6: A phase conjugate mirror enables time reversal of light, even through multiple-scattering media. The spatial distortion introduced into the incoming beam can be precisely reversed by the phase conjugate beam.

In practice, $\epsilon(\mathbf{r})$ is not purely real (lossy) and the limited technical capability of current SLM technology (e.g. the limited number of degrees of freedom) does not allow us to produce a perfect phase conjugate wave. However, the time-reversal effect can be produced even with optical phase conjugation over a limited area or a limited

transverse (Fourier) wave vector range. This can be understood in the transmission matrix formalism provided in section 1.3.2.

Here, we assume the light originates from a point source (assumed to be 1st mode on input side) and propagates through a scattering medium. Then, from Eq. (1.21), the m_{th} element of the discretized output field on the right side of the scattering media can be expressed as [11, 12]

$$(E_o)_m = (T)_{m1} (E_i)_1 . \tag{1.29}$$

Here, the transmission matrix element $(T)_{m1}$ (relating the input field at the 1st input mode to the mth output mode) follows the random Gaussian distribution. With the phase conjugate field generated on the output side, the reconstructed field at the 1st mode on the input side can be expressed as follows:

$$(E_{\text{opc}})_1 = a \sum_{m=1}^{M} (T)_{m1} (E_o^*)_m. \tag{1.30}$$

Here, we use the fact that the transmission matrix element relating the field at the 1st input mode to the mth output mode is identical to the element associated with the propagation from the nth output mode to the 1st input mode due to the time-reversal symmetry of light propagation. a is a gain factor of the phase conjugation process. Substituting the $(E_o)_m$ term on the right-hand side of Eq. (1.30) with the expression in Eq. (1.29), we get

$$(E_{\text{opc}})_1 = a (E_i^*)_1 \sum_{m=1}^{M} | (T)_{1m} |^2. \tag{1.31}$$

When the conventional plane wave is incident on the output side (without phase conjugation), the field at the 1st mode on the input side is given by

$$(E_{\text{background}})_1 = \gamma \sum_{m=1}^{M} (T)_{1m}, \tag{1.32}$$

where $\gamma = \left| a (E_i^*)_1 \sum_{m=1}^{M} | (T)_{1m} |^2 \right|$ is the normalization factor to match incidence

input power associated with the case of phase conjugation in Eq. (1.30). The background intensity $\left|(E_{\text{background}})_1\right|^2$ can also be thought of as the intensity in the vicinity of the 1st mode on the input side. The resulting intensity enhancement (peak-to-background ratio) is then given by

$$\eta = \frac{\left|(E_{\text{opc}})_1\right|^2}{\left|(E_{\text{background}})_1\right|^2} = M. \tag{1.33}$$
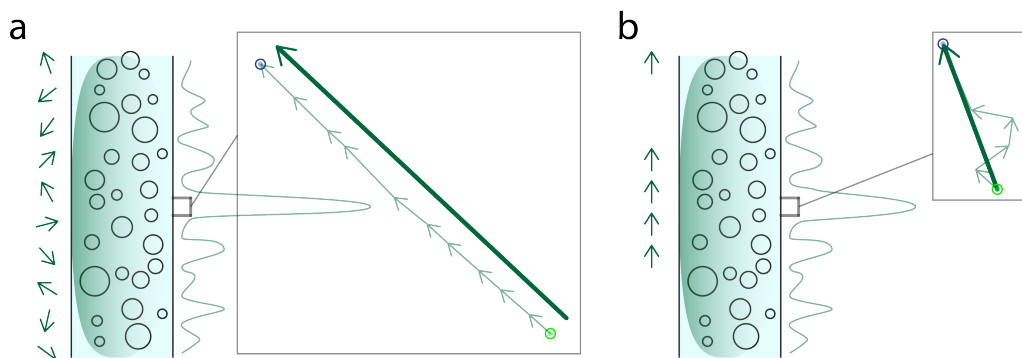
Figure 1.7: Focusing light through scattering media. Light intensity at a chosen point behind the scattering medium can be optimized through either (a) phase-only or (b) amplitude-only modulation of the incident beam

While the background random intensity is inevitable due to the imperfect phase conjugation, the intensity at the original input mode can be enhanced by a factor of M (the number of controlled optical modes from the output side) with the phase conjugation process. We note that the field enhancement can also be achieved through either phase-only or amplitude-only modulation. In these cases, the corresponding enhancement factors are given by [12, 27]

$$\begin{aligned} \eta &= \frac{\pi}{4}M \qquad \text{(phase only)} \\ &= \frac{1}{2\pi}M \quad \text{(amplitude only)}. \end{aligned} \tag{1.34}$$

Figure 1.7 graphically describes how the intensity enhancement (at a chosen point behind the scattering medium) can be achieved through wavefront modulation of the

incident beam.

The concept of employing a wavefront shaping technique to multiply scattering media (10.1 μm thick rutile where light scatters on average by 18 times) was first demonstrated by Vellekoop *et al.* in 2007 [12]. In this earlier work, the incident wavefront is controlled by LC-based SLM to progressively achieve the constructive interference of the scattered field at a chosen point. The feedback optimization algorithm was designed to find the proper phase modulation $\exp(-i\Delta\psi)$, which compensates the phase delay $\exp(i\Delta\psi)$ associated with field propagation through multiply scattering media. Thus, the optimization process is mathematically identical to the optical phase conjugation process. In 2008, Yaqoob *et al.* implemented an optical phase conjugation based on photorefractive crystal (Fe-doped $LiNbO_3$) and directly demonstrated the time-reversal of light through 0.69-mm-thick biological tissue (which on average scatters light 26 times) [19]. These early works have been followed by numerous applications, improvements, and theoretical studies regarding wave propagation through random media.

1.5   Scope of This Thesis

This thesis discusses a number of interrelated topics on optical phase conjugation and its applications in biology. The chapters are organized as follows. Chapter 2 introduces a new electro-optic method, called digital optical phase conjugation, with a comparison to traditional analog means of implementing optical phase conjugation. We then present a computational method for automatic alignment of digital OPC, which requires a precise pixel-to-pixel alignment between digital sensor and spatial light modulator. In chapter 3, we present two OPC-assisted optical focusing methods. Two methods, respectively, exemplify how OPC can be exploited for isotropic light focusing and dynamic focusing. Chapters 4 and 5 discuss a recently developed class of techniques that uses a physical or virtual guidestar for deep tissue (> 1 mm) light focusing and imaging. In Chapter 4, we take the time-reversed ultrasonically encoded optical focusing technique as an example and model each step of the tech-

nique to investigate the allocation of a photon budget throughout the process and the influence of shot noise on optical phase conjugation, and finally to estimate the penetration depth limit. In Chapter 5, we report two deep tissue light focusing methods - iterative TRUE optical focusing and time-reversed ultrasound microbubble encoded optical focusing - that aim to render the time-reversed spot with improved contrast and resolution. Finally, in Chapter 6, we reveal the theoretical relation between time-reversal fidelity and speckle intensity autocorrelation (a conventional measure of scatterer movement) through dynamic scattering media, and validate the relation through experiments on living tissue.

Chapter 2

Method for Auto-alignment of Digital Optical Phase Conjugation

Optical phase conjugation (OPC) has enabled many optical applications such as aberration correction and image transmission through fiber. In recent years, implementation of digital optical phase conjugation (DOPC) has opened up the possibility of reducing the effect of scattering and manipulating light deep inside random media. DOPC is particularly useful in biomedical studies due to its ability to provide greater-than-unity OPC reflectivity (the power ratio of the phase conjugated beam and input beam to the OPC system) and accommodate additional wavefront manipulations. However, the requirement for precise (pixel-to-pixel matching) alignment limits the practical usability of DOPC systems. Here, we propose a method for auto-alignment of a DOPC system where the misalignment between the sensor and the SLM is automatically corrected through digital light propagation.[1]

---

[1]This chapter is reproduced with some adaptations from the manuscript Jang, M.*, Ruan, H.*, Zhou, H., Judkewitz, B. & Yang, C. Method for auto-alignment of digital optical phase conjugation systems based on digital propagation. Opt. Express 22, 14054 (2014). *: equal contributions. MJ contributed to developing the idea, implementing the auto-alignment algorithm, designing and conducting the experiments, analyzing the experimental results, and preparing the manuscript.

2.1 Analog and Digital Optical Phase Conjugation System

Optical phase conjugation has been extensively studied since the 1960s. Based on its time-reversal property, optical phase conjugation has been of interest in many optical applications including aberration correction [26, 28–30], optical resonators [31, 32], pulse compression [33, 34], image transmission through fibers [26, 35], and high-resolution imaging [36, 37]. The first experimental demonstration of optical phase conjugation was performed with stimulated Brillouin scattering [38]. Various wave mixing processes (such as four-wave mixing and three-wave mixing) and photorefective effect [28, 31, 32, 36, 37] have been subsequently used to produce the optical phase-conjugate waves.

Because nonlinear media typically have the capacity for high spatial frequency components, OPC based on nonlinear phenomena supports OPC playback over a large collection angle and in a large number of optical modes [26, 37]. However, such techniques have practically limited flexibility in terms of working optical wavelength and intensity. More importantly, the OPC reflectivity achievable with such techniques is severely limited and is generally orders of magnitude below unity [39, 40]. Moreover, additional manipulation of the phase-conjugated field prior to playback, which is highly preferable in many biomedical applications [41], is not possible with such bulk medium approaches.

To address these limitations in the context of biophotonics applications, an opto-electronic digital OPC system (DOPC) was developed [42, 43]. The DOPC system consists of two parts: a CCD or CMOS camera for wavefront recording and a spatial-light modulator (SLM) for wavefront playback. These two components are precisely aligned around a beamsplitter to optically situate the two digital components in the same optical position. The DOPC procedure follows two steps (shown in Fig. 2.3): (1) the wavefront of the input beam is measured on an sCMOS sensor array using either phase-shifting holography or off-axis holography; and (2) the conjugated copy of the measured wavefront is displayed on an SLM, such as a liquid crystal on silicon

(LCoS) or digital micromirror (DMD)-based devices. As the reference beam intensity can be arbitrarily changed, there is no theoretical limit to the maximum OPC reflectivity. Furthermore, such a system allows for further manipulation of the optical wavefront prior to playback. This flexibility is potentially useful and can enable applications such as OPC focal spot scanning [41].
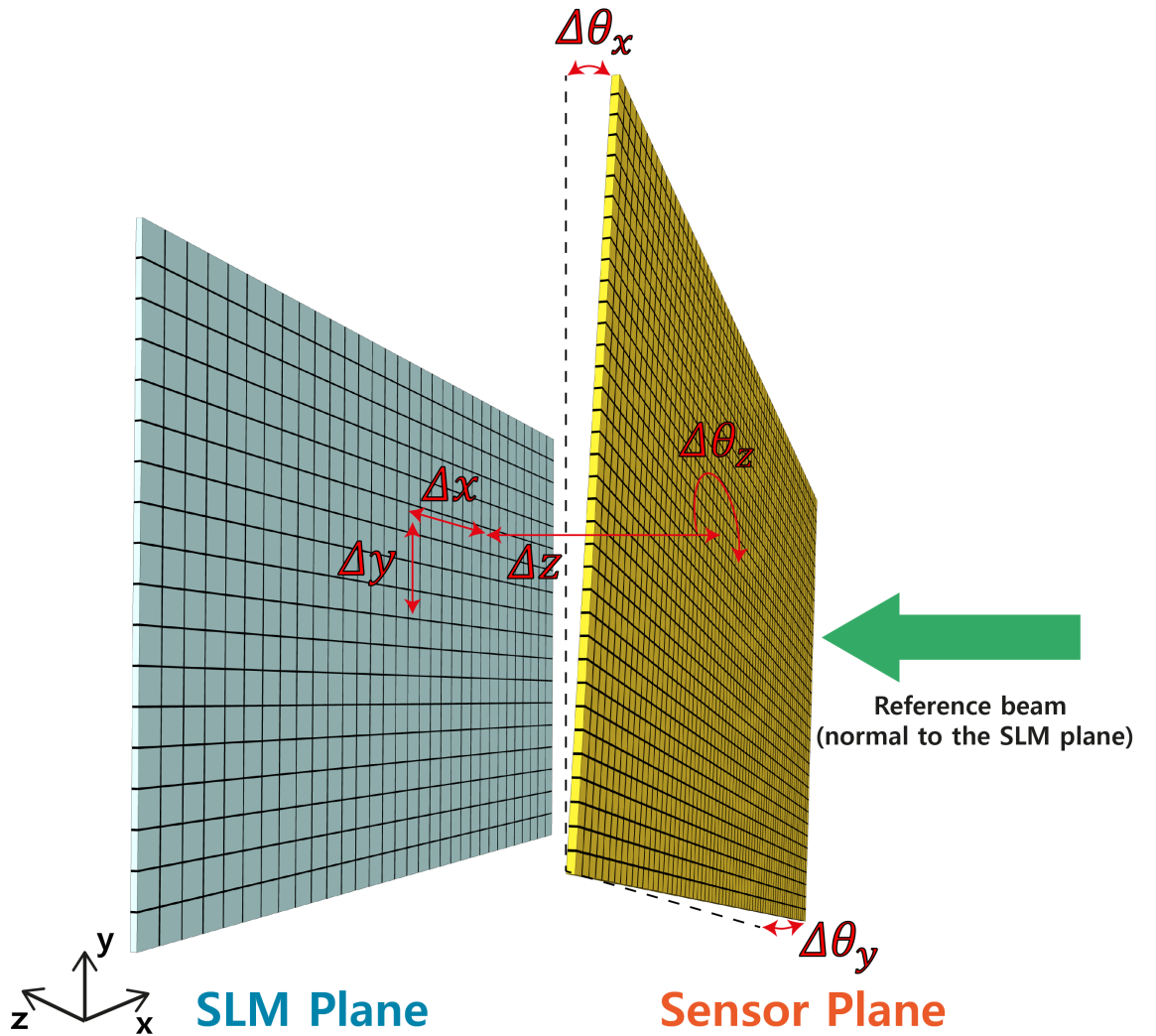
Figure 2.1: Six misalignment parameters in the alignment of the sensor plane and SLM plane in three-dimensional space. In-plane translation (Δx and Δy), in-plane rotation ($Delta\theta_z$), axial translation (Δz), and tip/tilt ($\Delta\theta_x$ and $\Delta\theta_y$) are present. The reference beam is normal to the SLM plane and, thus, it is obliquely incident on the sensor plane.

Despite its significant potential, the practical utility of a DOPC system has been

limited by implementation difficulties [42]. In brief, these difficulties stem from the need to achieve pixel-to-pixel matching of the sCMOS sensor array and the SLM in the system. To accomplish pixel-to-pixel matching, the sCMOS sensor array and the SLM need to be finely aligned in six misalignment dimensions: translational (Δx, Δy, and Δz), tip/tilt ($\Delta\theta_x$ and $\Delta\theta_y$), and rotation ($\Delta\theta_z$) (Fig. 2.1). Previous implementations further require a high quality macro lens to match the pixel size of the sensor and the SLM, if they are originally mismatched. The experimental procedure for bringing the system into precise alignment is highly exact and time-consuming to carry out. To make things worse, the alignment procedure does not allow for a quick shortcut realignment of the system if the system drifts out of alignment by even a very small amount (e.g., a few tens of microns). These difficulties are likely to be the major contributive factors that limit the broader application and implementation of DOPC systems beyond a few research groups.

2.2   Auto-alignment Method
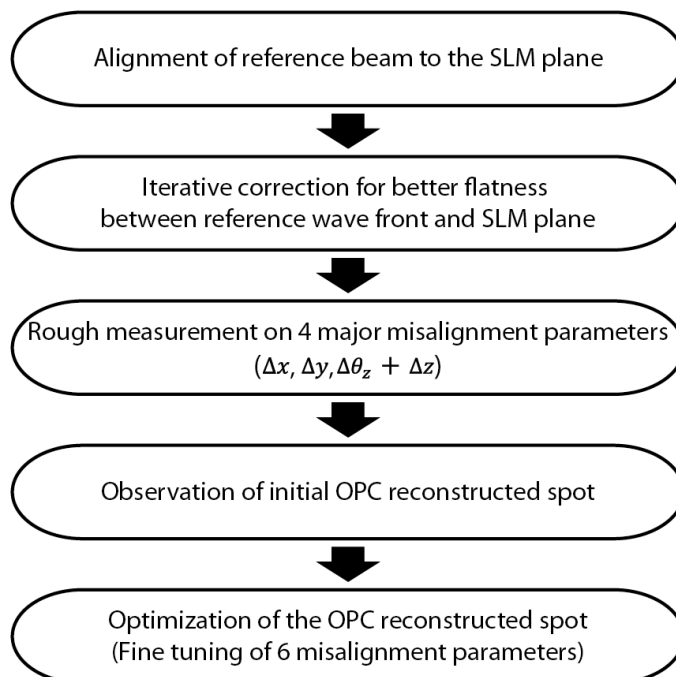
Figure 2.2: A scheme of the auto-alignment of a DOPC system. Flatness between the reference beam wave front and the SLM plane is optimized by the first two steps. Then, the misalignment parameters (three in-plane parameters Δx , Δy , and $\Delta\theta_z$, and axial translation Δz) are roughly measured. Next, the measured incoming wavefront is digitally propagated to the SLM plane with the roughly measured parameters to virtually achieve the rough alignment. At this step, an initial reconstructed DOPC signal (in our case a low contrast focal spot) can be observed. In the last step, all misalignment parameters are finely tuned around the roughly measured parameters while the intensity of the phase-conjugated focal spot (DOPC performance) is optimized.

We propose a computational-based alignment strategy for implementing automatic alignment of a DOPC that does not require physically bringing the sCMOS sensor array and the SLM into precise alignment. Instead, this method digitally propagates the optical wavefront, as measured at the sCMOS sensor array, to the virtual SLM plane. Through this means, optical phase-conjugation playback can be implemented on the SLM even if the measurement plane and SLM plane are not physically aligned. This auto-alignment process is performed through the following steps (Fig. 2). In

step 1, a collimated reference beam is directed at the SLM at a normal incidence. A measurement and correction procedure is then performed to correct for reference beam imperfections and SLM curvature (flatness optimization). In step 2, a rough measurement of four major misalignment parameters (Δx , Δy , and Δz and $\Delta\theta_z$) is made. This measurement allows an approximate digital propagation to θ_z to be performed and allows for the sCMOS sensor array to the SLM to be aligned. This roughly aligned system is then able to render an unoptimized DOPC reconstruction. In step 3, six misalignment parameters are iteratively fine-tuned by monitoring the DOPC reconstruction signal. Through this means, the DOPC system can be brought into optimized virtual alignment. Step 3 can be repeated with ease when mechanical drifts or shocks misalign the DOPC system in minor ways.

2.2.1 Experimental setup
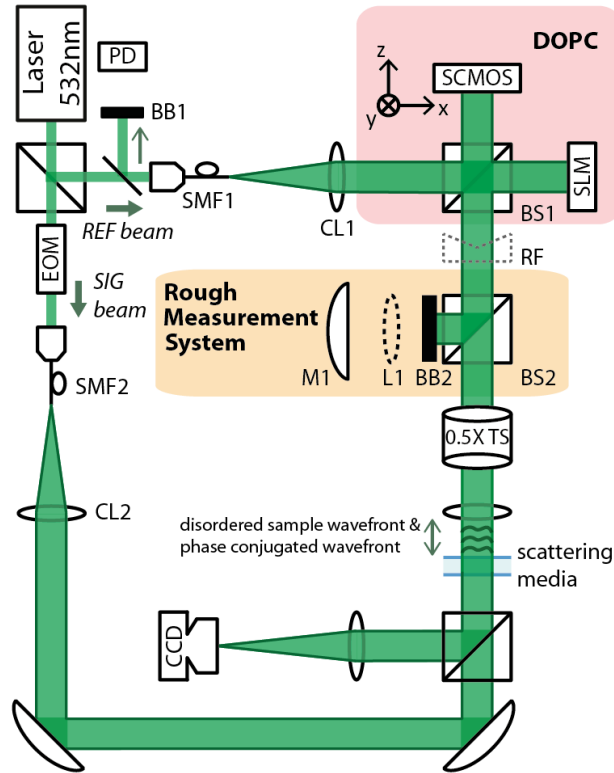
Figure 2.3: Experimental scheme of digital OPC. The laser beam is split into two arms: a reference arm and a sample arm. As the first step of DOPC procedure, the sCMOS camera captures the interferograms created by the reference beam and signal beam being transmitted through the scattering media (five layers of scattering film). A four-step phase-shifting method is used for the wavefront measurement of the signal beam. The EOM, placed on the sample arm, shifts the relative phase between two beams. Then, for the time-reversal playback, SLM is used to display the phase-conjugated wavefront, which is measured by the sCMOS camera and digitally propagated. The phase-conjugated light beam (SLM-reflected reference beam) is collimated through the turbid media and creates a focal spot on the CCD camera. The use of photo diode and rough measurement system is detailed in Fig. 2.4 and Fig. 2.5, respectively. SMF, single mode optical fiber; 0.5× TS, 0.5× telescope (from top to bottom); CL, collimation lens; BS, beam splitter; RF, retro reflector; L, lens; M, mirror; BB, beam block; PD, photo diode; EOM, electro-optic phase modulator; SLM, spatial light modulator; sCMOS, scientific CMOS camera; CCD, CCD camera.

Figure 3 shows the experimental setup for our study. The laser beam (532 nm and 150 mW diode-pumped solid state CW) is split into a reference beam and a signal beam. These two beams are spatially filtered by single mode optical fibers (460 HP, Thorlabs) and then collimated. The sample beam, which is scattered by a light-scattering sample (five layers of scattering film stacked on top of each other, Scotch 810 Magic tape, 3M) interferes with the reference beam on the sensor plane of the sCMOS camera (pco.edge 5.5, PCO). Phase measurement of the scattering field is then realized by phase-shifting holography [44]. An electro-optic phase modulator (EO-PM-NR-C4, Thorlabs) is used to step the relative phase between the reference beam and the sample beam. Then, we digitally propagated the measured wavefront and displayed the phase-conjugated copy of it on the SLM (PLUTO phase only, Holoeye). The phase-conjugated light beam, which is expected to be collimated after propagating back through the scattering media, is focused on the CCD camera (DMK 31BU03, The Imaging Source). In our system, the pixel dimensions of the sCMOS sensor array and the SLM were 6.5 and 8 microns, respectively, and 2560×2160 and 1920× 1080 pixels were present on each device. Thus, the sCMOS sensor array covered a larger area than the SLM. During the experiment, we set the region of interest of the sCMOS sensor array to be 2364×1330 pixels in order to match the physical size of the SLM. Subsystems for optimizing the flatness of the reference beam wavefront to the SLM surface and the rough measurement of misalignment parameters are explained in Sections 2.1 and 2.2.

Throughout this study, the contrast of the phase-conjugated focal spot (peak to background ratio, PBR) on the CCD was used to quantify the DOPC performance. Here, the peak was the maximum intensity of the DOPC focal spot, and the background was the mean intensity of the speckle pattern on the CCD when a random phase map was displayed on the SLM rather than phase-conjugated copy. By mathematically modeling the scattering medium transmission function as a complex random Gaussian matrix, the PBR can be calculated as $\pi N/4$ where N is the number of optical modes captured/controlled by the DOPC system. Then, N is simply given by P/S where P is the total number of controllable DOPC pixels and S is the speckle

coherence area in pixel numbers [12]. If the DOPC system is perfectly aligned, P is approximately given by the smaller value of the number of pixels in the sCMOS sensor array and the SLM (in our case, 1920×1080 since the SLM has a smaller number of pixels). In our experiment, speckle granularity was around 3×3 SLM pixels. Thus, the theoretical maximum PBR was 180000 .

2.2.2   Flatness Optimization of Reference Beam

The optimal performance of the DOPC system requires that the reference beam's wavefront be fully characterized on both the sCMOS sensor array and the SLM surface. This is because the reference beam serves both as the interfering reference beam for wavefront measurement of the incoming signal light field on the sCMOS sensor array and as the blank input wavefront that the SLM subsequently modifies to create the OPC field. In the conventional DOPC system, we would exactingly align a collimated reference beam normal to the SLM and precisely align the sCMOS sensor array to the SLM at the individual pixel level [42]. The collimation and normal incidence condition simplified the DOPC processing as we were able to accomplish DOPC playback by simply projecting a sign-reversed copy of the measured phase variations from the sCMOS sensor array onto the SLM [42]. In practice, however, available SLMs have considerably curved surfaces and reference beams cannot be assumed to be perfectly flat.

To address these limitations, we compensated for marginal imperfections in the reference wavefront and SLM surface curvature (deviation from perfect flatness) by finding the SLM phase pattern that transforms the reference beam to be flat in phase spatially during reflection [45]. This typically boosted the OPC performance by 2–5 times (depending on the initial alignment between the reference beam and the SLM plane).

This procedure was accomplished by going through the following steps. First, as is done in the conventional DOPC system, a retroreflector (RF) was temporarily inserted into the setup (gray dotted line, see Fig. 3) to create a Michelson interferometer. This

allowed us to make the reference beam (directed onto the sCMOS sensor array by the beamsplitter) interfere with the SLM-reflected reference beam (directed onto the sCMOS sensor array by the beamsplitter, BS1 in Fig. 3), and retroreflector, RF (gray dotted line, in Fig. 3). We then tip/tilt the SLM or adjust incidence angle of reference beam to SLM until the dominant lowest spatial frequency component of the observed interference pattern was at its lowest possible value. If the reference wavefront and SLM plane were flat, the interference pattern would be completely uniform when the normal incidence is achieved. However, as there were practical imperfections, we ensured that the reference beam was almost normal to the SLM by observing for the pattern with the lowest possible frequency. This step minimizes the marginal imperfections we need to correct in the next step.

We next proceeded to determine an appropriate compensation phase pattern to display on the SLM that would ensure that the reflected reference beam was spatially flat in phase. This was done by observing the collected power at the photo diode (PD) (2001-FS, New Focus) in Fig. 2.3. A simplified vignette of the experimental scheme that is relevant for this process is shown in Fig. 4. In brief, the reference light reflecting off the SLM propagates back through the SLM and is in turn detected by the PD. This signal is maximized if the reflected reference beam is spatially flat in phase. As shown in Fig. 2.3, the reference beam is spatially filtered by SMF 1 and collimated by collimation lens CL 1. Then, the reference beam is reflected off the SLM and focused back on the SMF 1 through CL1. Therefore, if the optical flatness between the reference wavefront and SLM surface is retained by displaying a compensation phase pattern, SLM-reflected light couples back to the SMF 1 with high efficiency.
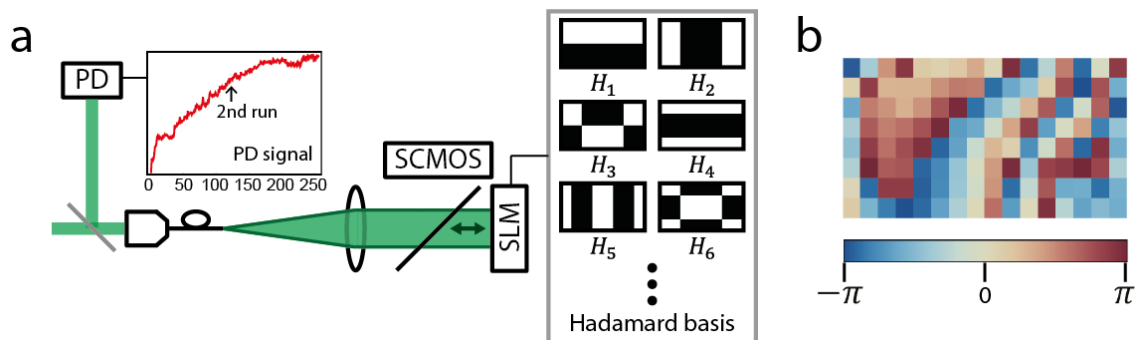
Figure 2.4: Iterative searching for an SLM pattern assuring flatness of the reference wavefront to the SLM surface. (a) SLM iteratively displays the phase map that consists of the optimized phase map from the previous step and the "+1" part of a Hadamard pattern (H_n). For each iteration, four measurements from the PD were obtained by stepping in phase on a Hadamard basis by $\pi/2$. An optimized phase map based the Hadamard basis was calculated using these four measurements. The PD signal inset shows the photo diode signal optimized during the iterative procedure. The Hardamad basis inset shows the 2D discrete Hardamad basis used for each iteration step (with the "+1" part in white and "-1" part in black). (b) Acquired phase map after two runs of the iterative procedure. This map optimizes the flatness between the reference wavefront and the SLM surface.

In our experiment, we iteratively searched the phase map to maximize the PD signal (optimizing flatness). Here, we used the 16×8 Hadamard basis (1920×1080 SLM pixels divided into 128 sections of 120 pixels×135 pixels) as the input basis [13]. That is, starting from the pattern with low spatial frequency, the optimum phase (ϕ_n) for the "+1" part of each Hadamard pattern (H_n, Fig. 2.4 Hadamard basis inset) was obtained. This choice of basis was very suitable for this purpose because the optical aberration and the SLM curvature were mainly in the low spatial frequency regime. Also, as half of the SLM pixels were modulated, the signal-to-noise ratio (SNR) at the PD was largely improved compared to the SNR of pixelwise optimization [13].

The iteration procedure was as follows. The nth phase pattern displayed on the SLM (ψ_n) consisted of two components, the optimized phase pattern from the previous iteration (ψ_{n-1}) and the "+1" part of the Hadamard basis (H_n, shown in Fig. 2.3 inset, "-1" part with zero phase). While displaying the addition of two phase

maps, we stepped the phase of the "+1" part (white portion in the inset) in four phases ($\exp\left(iH_n\right)$, $\exp\left[i(\pi/2)H_n\right]$, $\exp\left(i\pi H_n\right)$, and $\exp\left[i(3\pi/2)H_n\right]$). Consequently, the four interference intensities ($I_{n,1}$, $I_{n,2}$, $I_{n,3}$, and $I_{n,4}$) were measured from the PD. Mathematically, the interference intensity $I_{n,k} = |E_{mod}\exp\left(ik\pi/2\right) + E_{unmod}|^2$, where E_{mod} and E_{unmod} were resultant fields at the PD from modulated pixels and unmodulated pixels of the SLM, respectively. Then, the optimized phase for the nth Hadamard basis was simply calculated as $\phi_n = \tan^{-1}\left[\left(I_{n,2} - I_{n,4}\right)/\left(I_{n,1} - I_{n,3}\right)\right]$. The optimized phase pattern (ψ_n) was then updated by adding the Hadamard basis with the optimized phase ($\psi_{n-1} + H_n\phi_n$). As shown in the Fig. 2.4(a) PD signal inset, the PD signal increases as the flatness is compensated at each iteration step. After 128 iteration steps for each Hadamard basis, the phase map optimizing the flatness between the reference wavefront and the SLM was obtained (ϕ_{128}). The flatness can be further improved by repeating this iterative loop based on the optimized phase map from the previous run. In our experiment, we ran the iterative loop twice. At the end, when we played back the OPC beam, and the optimized pattern from the second run (shown in Fig. 2.4(b)) was added to the phase-conjugated wavefront.

2.2.3 Rough Measurement of the Major Misalignment Parameters

DOPC alignment can be thought as an optimization procedure with a global maximum (corresponding to the alignment with the highest DOPC PBR). The simplest strategy for finding the maximum would be an exhaustive parameter search. However, due to the number of parameters, this strategy would be slow and inefficient, particularly when starting far from the maximum. We, therefore, adopted a strategy in which we first obtained rough estimates of the misalignment parameters, in order to get closer to the maximum. Only then were parameters fine-tuned by a search strategy.

Rough measurements were done in two steps; measurement of in-plane misalignment parameters (Δx, Δy, and $\Delta\theta_z$) and measurement of axial displacement (Δz). A

subsystem for the rough measurement simply consisted of a plane mirror and a bulk lens (focal length $7.5\,\mathrm{cm}$). As for the SLM, the mirror surface was also aligned perpendicular to the incoming reference beam. The detailed procedure for the measurement is described in the following subsections.

Before proceeding, we would like to note that the tip/tilt misalignment of the sample and reference beams relative to the sCMOS sensor array does not actually have a significant impact on the DOPC performance. This robustness at the detection side is in remarkable contrast to the exacting alignment by which we ensure that the reference beam is normal to the SLM. This can be explained by noting that tip/tilt misalignment of the reference beam to SLM plane would result in a subsequent DOPC playback that is angled away from its intended path. In contrast, the sCMOS would still be able to obtain a reasonably accurate measurement of the interference light field if the tip/tilt of the sCMOS is small. To clearly illustrate this point, consider the interference of a sample beam with a reference beam that subtends an angle of θ_{sam}. Further suppose that the reference beam is at an angle of $\Delta\theta_x$ or $\Delta\theta_y$ with respect to the sCMOS sensor array ($\Delta\theta_x = \Delta\theta_y = 0$ would mean that the reference beam is at normal incidence). The resulting interference fringe pattern we would see would have a periodicity given by:

$$k\sin\left(\theta_{sam} - \theta_{xory}\right) - k\sin\left(-\theta_{xory}\right) = k\sin\left(\theta_{sam}\right), \tag{2.1}$$

when θ_{sam}, $\Delta\theta_x$, and $\Delta\theta_y$ are both small. k is the wave number. Notice that the $\Delta\theta_x$ and $\Delta\theta_y$ has no contributive component in the simplification of the equation. In other words, as long as θ_{sam} and $\Delta\theta_x$ and $\Delta\theta_y$ are small, the sCMOS sensor would see the same interference pattern independent of the tip/tilt misalignment. In most DOPC systems, the range of θ_{sam} we work with is actually quite small (a span of $\sim 6\,°$ is typical). As such, we can ignore tip/tilt misalignment as long as the misalignment is small (within the range of $10\,°$ or less) as well.

Rough Measurement of In-plane Misalignment Parameters

For in-plane misalignment parameters (Δx, Δy, and $\Delta\theta z$), four Fresnel zone patterns were displayed on the SLM, which is equivalent to four convex lenses (Fig. 2.5(b)). The focal length of these Fresnel zone patterns was chosen so that four focal spots were projected onto the sensor plane (Fig. 2.5(c)). The reference beam is reflected off the SLM plane and relayed by BS1, BS2, M1, BS2, and BS1 in the order as shown in Fig. 2.5(a). Δx and Δy were then simply estimated by measuring the distances between the positions of measured four points (magenta points in Fig. 2.5(c)) and the ideal positions of the points (center of the zone plates, white points in Fig. 2.5(c)). For the rotation ($\Delta\theta_z$), the angle between the horizontal line and the line connecting the two bottom points or two top points was evaluated. When the tip/tilt misalignment ($\Delta\theta_x$ and $\Delta\theta_y$) was large, we also roughly measured these parameters from the four spots by observing the extended distance between the spots.

Rough Measurement of Axial Displacement Misalignment

In order to measure the axial displacement (Δz), a plano-convex lens (7.5 cm focal length) was placed between the SLM and the mirror (Fig. 2.2). In this case, only a single Fresnel zone pattern was displayed on the SLM (Fig. 2.5(e)). The focal length of this zone pattern was chosen such that the SLM-reflected light beam focused on the focal plane of the lens (L1) which collimated the beam. This beam was then reflected off the mirror (M1) and focused back on the plane on which the original focal spot was made (Fig. 2.5(d)). The interference between the original reference beam (reflected off the BS1) and the beam that travels through the rough measurement system created an interference pattern (Fresnel zone pattern) on the sensor plane. Then, the focal length of the measured Fresnel zone pattern was obtained by fitting it to a lens transmission function ($= \exp ik\left(x^2 + y^2\right)/2f$, here f is the focal length). Finally, we roughly determined the axial displacement between two planes by comparing the fitted focal length of the measured zone pattern on the sensor (Fig. 2.5(f)) and the focal length of the original zone pattern displayed on the SLM (Fig. 2.5(e)). We could

roughly achieve the virtual alignment by plugging the roughly measured parameters (Δx, Δy, $\Delta \theta z$, and Δz) into the digital light propagator. This allowed us to render an unoptimized OPC focal spot that served as the feedback source for the parameter fine-tune procedure.
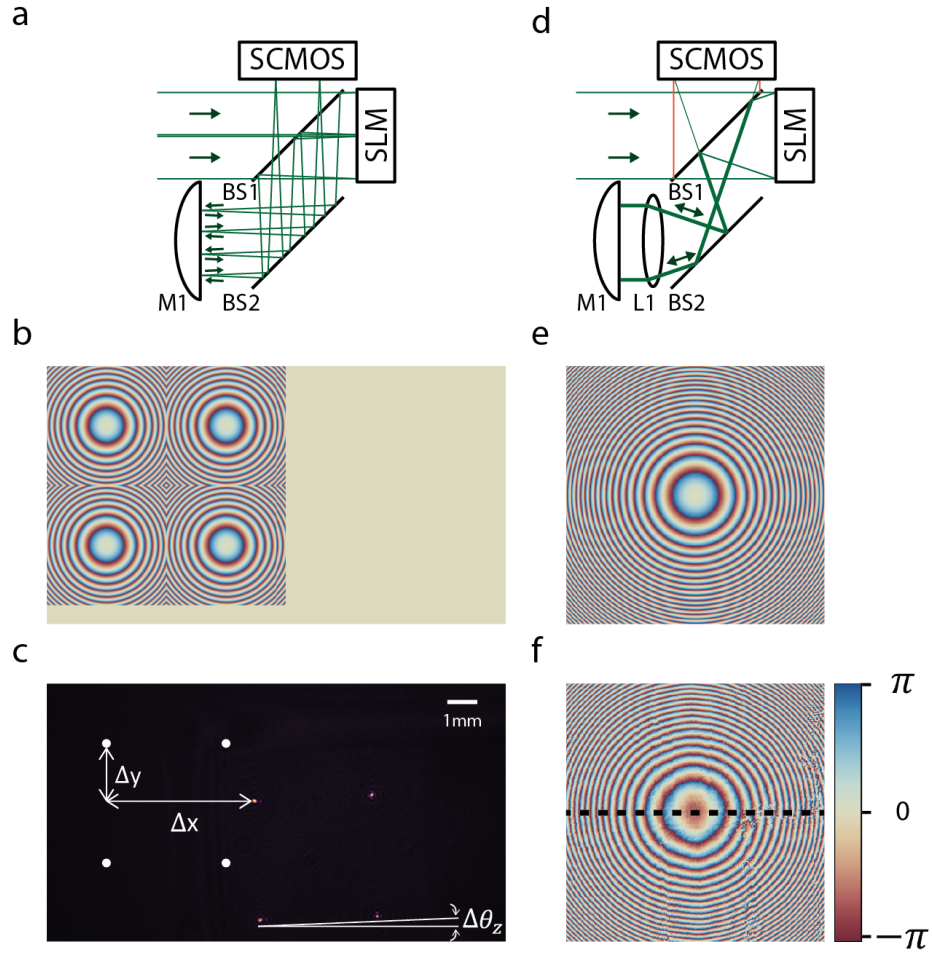
Figure 2.5: Rough measurement of the four major misalignment parameters. (a, b and c) Measurement of in-plane misalignment parameters. (a) Four Fresnel zone patterns are displayed on the SLM so that the mirror-reflected light creates four foci on the sCMOS sensor plane. (b) Four Fresnel zone patterns displayed on the SLM for the measurement of in-plane misalignment parameters. (c) Four foci created on the sCMOS sensor plane (magenta points). The overlaid white points are the ideal positions of the four foci. Δx, Δy, and $\Delta \theta z$ are roughly measured by comparing the distances and angles between the ideal spots and measured spots. (d, e, and f) Measurement of the axial displacement. (d) The single zone pattern is displayed. The wavefront of the back-propagated light into the sCMOS (by the interference between the red and green light rays) is measured. (e) The zone pattern displayed on the SLM for the measurement of the axial displacement. (f) The zone pattern measured from the sCMOS camera. Δz is determined by comparing the corresponding focal length of the displayed and the measured zone patterns.

2.2.4 Digital Light Propagation

The digital propagator is implemented with a scalar diffraction theory based on the angular spectrum method [46–48](as shown in Fig. 2.6). In contrast to the other scalar diffraction theories such as the Fresnel diffraction formula and the Kirchhoff diffraction formula, the angular spectrum method provides the diffraction field without approximation. Here, it was performed in three steps: (1) decomposition of the measured field (Fourier transform) into Fourier components (the measured field is shown in Fig. 2.6 upper left); (2) propagation (adding phase corresponding to the axial misalignment) of each Fourier component (Fig. 2.6 bottom); and (3) addition of the Fourier components (inverse Fourier transform) at the reference plane (inverse Fourier transformed field is shown in Fig. 2.6 upper right), here the SLM plane. Assuming f_x and f_y are spatial frequencies defined on the SLM plane, the angular spectrum method is mathematically expressed as

$$U_{SLM} = \int_{f_x, f_y} \hat{U}_{SA} \left(f_x, f_y \right) \exp \left(-2\pi i f_x x \right) \exp \left(-2\pi i f_y y \right) df_x df_y, \qquad (2.2)$$

where $\hat{U}_{SA}$ and H_{AS} are are Fourier components of the measured field and the angular spectrum transfer function. U_{SLM} s the propagated field on the SLM plane. H_{AS} is given:

$$H_{AS} = \exp \left[-ik\Delta z \sqrt{1 - \left(\lambda f_x \right)^2 - \left(\lambda f_y \right)^2} \right], \qquad (2.3)$$

where λ is the wavelength so that the exponential term is simply the additional phase of the Fourier component at (f_x, f_y) as it propagates for Δz.

The formula above is based on the regular angular spectrum diffraction theory describing diffraction of the light field between two parallel planes. To take account of the fact that the sensor plane is tip/tilted with respect to the SLM plane by $\Delta\theta_x$ and $\Delta\theta_y$, we first added the phase gradient of the oblique reference wave on the measured wavefront. Because the reference beam is normally incident on the SLM plane, it arrived on the sCMOS sensor array with an oblique angle of $\Delta\theta_x$ and $\Delta\theta_y$ as shown in Fig. 1. Then, we considered the transformation to relate the Fourier basis of the mea-

sured plane $(f'_x, f'_y, \hat{U}_{SA}$ is initially calculated) into the Fourier basis of the SLM plane (f_x, f_y) using the following rotation [48]: $(f_x, f_y, f_z(f_x, f_y)) = T\left(f'_x, f'_y, f'_z(f'_x, f'_y)\right)$ where T is a transformation matrix given by $T = R_x^{-1} R_y^{-1} (T^{-1} = R_y R_x)$. R_x and R_y are rotation matrices along the x and y axes, respectively. They are given by

$$R_x = \begin{bmatrix} 1 & 0 & 0 \\ 0 & \cos(\Delta\theta_x) & -\sin(\Delta\theta_x) \\ 0 & \sin(\Delta\theta_x) & \cos(\Delta\theta_x) \end{bmatrix} \text{ and } R_y = \begin{bmatrix} \cos(\Delta\theta_y) & 0 & \sin(\Delta\theta_y) \\ 0 & 1 & 0 \\ -\sin(\Delta\theta_y) & 0 & \cos(\Delta\theta_y) \end{bmatrix}. \quad (2.4)$$

This transformation allowed us to express the Fourier components of the measured wavefront on the sCMOS sensor array on the Fourier basis of the SLM plane.

We corrected the in-plane displacement misalignment by using the following functional relationship for shifting:

$$U_{SLM}(x - \Delta x, y - \Delta y) \leftrightarrow \exp(-2\pi i \Delta x f_x) \exp(-2\pi i \Delta y f_y) \hat{U}_{SLM}(f_x, f_y). \quad (2.5)$$
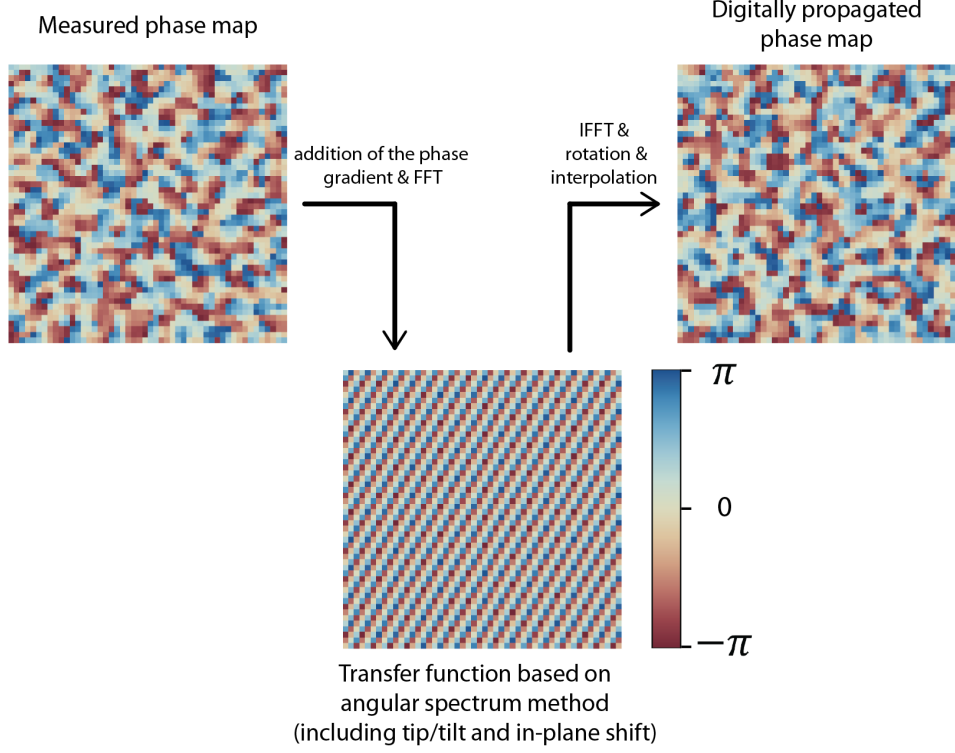
Figure 2.6: Auto-alignment based on digital propagation with an angular spectrum method. First, the measured phase map from the sCMOS sensor array is multiplied with the phase gradient of the oblique reference beam (corresponding to $\Delta\theta_x$ and $\Delta\theta_y$) and Fourier transformed. Then, the Fourier components are multiplied with the transfer function based on the angular spectrum method (including tip/tilt and in-plane shifts). Thus, the five misalignment parameters (Δx, Δy, Δz, $\Delta\theta_x$, and $\Delta\theta_y$) are taken account in this step. Then, the map in the Fourier domain is the inverse Fourier transformed to get the phase map on the SLM plane. At the final step, the phase map is rotated ($\Delta\theta_z$) and interpolated at each SLM pixel position.

Finally, the digital propagation of the measured field, correcting all of the misalignment except the in-plane rotation ($\Delta\theta_z$), was given by

$$
U_{SLM}\left(x, y\right) = \hat{U}_{SA}^{tip/tilt}\left(T^{-1}\left(f_x, f_y, f_z\left(f_x, f_y\right)\right)\right) \hat{H}_{SA}\left(f_x, f_y\right) \left|J\left(f_x, f_y, f_z\left(f_x, f_y\right)\right)\right|
$$
$$
\times \exp\left(-2\pi i f_x\left(x + \Delta x\right)\right) \exp\left(-2\pi i f_y\left(y + \Delta y\right)\right) df_x df_y,
$$

$$(2.6)$$

where $\hat{U}_{SA}^{tip/tilt}$ is the Fourier component (expressed with the basis on the SLM plane with T^{-1}) of the measured field multiplied by the phase gradient due to the tip/tilt

of the sensor plane. That is, in the spatial domain,

$$U_{SA}^{tip/tilt}(x', y') = U_{SA}(x', y') \exp\left(i\left(kT_{1,3}^{-1}x' + kT_{2,3}^{-1}y'\right)\right), \tag{2.7}$$

where x' and y' are the axes defined on the sensor plane. $J(f_x, f_y, f_z(f_x, f_y))$ is the Jacobian determinant to correct the energy factor ($\propto \left|\hat{U}_{SA}\right|^2$)) along (df_x, df_y) as the transformation T is nonlinear. It is given by

$$\begin{aligned} J(f_x, f_y, f_z(f_x, f_y)) =\ & \left(T_{1,2}^{-1}T_{2,3}^{-1} - T_{1,3}^{-1}T_{2,2}^{-1}\right)\frac{f_x}{f_z(f_x, f_y)} \\ & + \left(T_{1,3}^{-1}T_{2,1}^{-1} - T_{1,1}^{-1}T_{2,3}^{-1}\right)\frac{f_y}{f_z(f_x, f_y)} + \left(T_{1,1}^{-1}T_{2,2}^{-1} - T_{1,2}^{-1}T_{2,1}^{-1}\right). \end{aligned} \tag{2.8}$$

At the end, U_{SLM} is rotated by the angle $\Delta\theta_z$ and interpolated at the positions of each sensor pixel.

Fine Tuning of the Parameters

As mentioned above, the initial OPC peak was observed by displaying the phase-conjugated copy of the propagated field with roughly measured parameters. However, in most cases, the OPC peak-to-background ratio is much lower than the theoretical value due to the limited accuracy with which the misalignment parameter can be measured. Thus, we fine-tuned the parameters to further improve the system performance. This was done by scanning over the parameter spaces around the roughly measured parameter set while optimizing for the intensity of the phase-conjugated focal spot. We scanned parameters in the order of Δx, Δy, Δz (displacement), $\Delta\theta_z$ (in-plane rotation), $\Delta\theta_x$, and $\Delta\theta_y$ (tip/tilt) and repeated this sequence with a smaller step size until the maximized OPC peak intensity was converged. Step sizes are empirically chosen based on the speckle size of the measured wavefront. Typically, it takes around 10 minutes to find optimal parameters. This time is expected to be shortened with a fast detector (e.g. photodiode) for measuring OPC peak intensity and a better algorithm to search the optimized parameters.

2.3   Results

In this section, we present the results we acquired while recovering the DOPC performance from a highly misaligned system (in all six parameters) as a case study: (1) images we captured for the rough measurement of the misalignment parameters, (2) measured misalignment parameters, (3) OPC reconstructed spot with the roughly measured parameters, (4) fine-tuned misalignment parameters, (5) optimized misalignment parameters, and (6) OPC reconstructed spot with the optimized parameters. In the subsequent section, we present the table of misalignment parameters (measured and optimized) and the corresponding PBR for five different misaligned scenarios.

2.3.1   Auto-alignment of a DOPC System

For demonstration purposes, we misaligned the sCMOS sensor array and the SLM in six degrees of freedom associated with all six misalignment parameters using translational, rotation, and tip/tilt stages. The in-plane translation misalignment was in the order of a millimeter, and the axial translation misalignment was in the order of a centimeter. For the rotation and tip/tilt, several degrees of misalignment were applied.

Figure 2.5(c) shows the four spots on the sCMOS sensor array (created by zone plates on the SLM as described in section 2.2.3). From this image, we estimated Δx, Δy, and $\Delta \theta_z$ by $-5006 \, \mu m$, $-1845 \, \mu m$, and $2.39\,°$. For the axial misalignment, we compared two focal lengths, fitting one from the measured zone plate on the sCMOS sensor array (Fig. 2.5(f)) and displaying one on the SLMs (Fig. 2.5(e)). We determined the axial misalignment to be $17\,514 \, \mu m$.

Then, we plugged those roughly measured parameters into the digital propagator and observed an OPC reconstructed spot, albeit with comparably low PBR of 60 (Fig. 2.8(b)). The roughly measured parameters were subsequently used as a basis for iterative fine tuning.
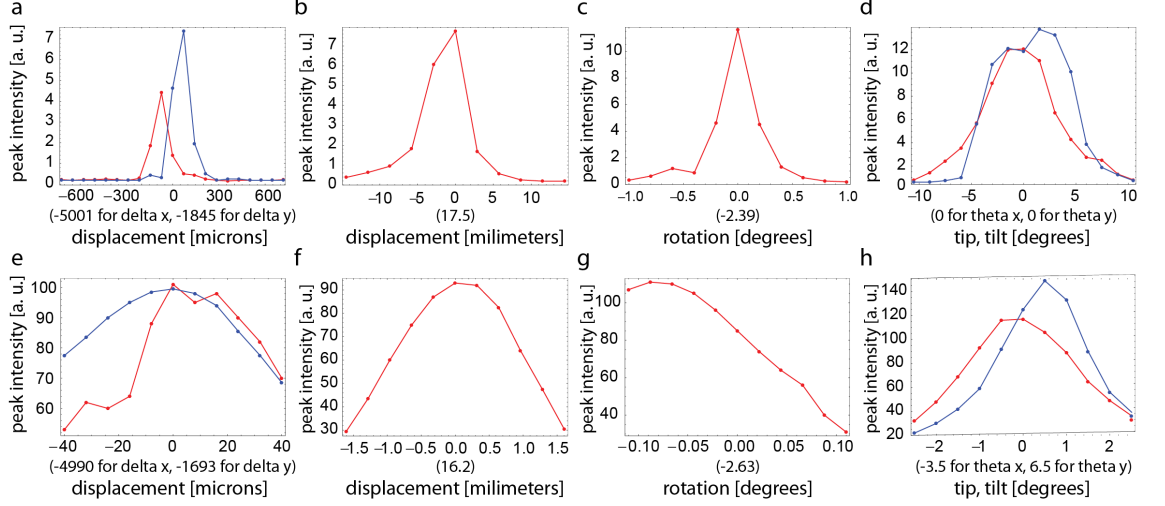
Figure 2.7: Optimization of the OPC reconstructed spot during the fine-tuning of the misalignment parameters. The peak intensities were measured from the CCD camera while scanning one parameter at a time. (a) and (e) for Δx (red) and Δy (blue). (b) and (f) for Δz . (c) and (g) for $\Delta \theta_z$. (d) and (h) for $\Delta \theta_x$ (red) and $\Delta \theta_y$ (blue). The upper row shows the signals measured during the rough scanning at the beginning of the fine-tune procedure. The bottom row shows the signals measured during the fine scanning at the end of the fine-tune procedure.

As described above, the fine optimization of the parameters was started from the most significant parameters, Δx and Δy, then Δz, $\Delta \theta_z$, $\Delta \theta_x$, and $\Delta \theta_y$ in order of decreasing significance. At each scanning step, the misalignment parameters were plugged into the digital propagator for correction. Then, the corresponding OPC peak intensity of the focal spot was measured. As an example, Fig. 2.7 shows the measured peak intensity while we were scanning through each misalignment parameter. For an effective search of optimized parameters, we first scanned the parameters with a large step size and then repeated the scan with a smaller step size. In Fig. 2.7, upper row and lower row present the DOPC focal spot intensity during scanning with a large step size and a small step size, respectively. The optimized parameters were found to be $-4490 \, \mu\text{m}$, $-1693 \, \mu\text{m}$, $16\,231 \, \mu\text{m}$, $-3.5\,°$, $7.0\,°$, and 2.72 (for Δx, Δy, Δz, $\Delta \theta_z$, $\Delta \theta_x$, and $\Delta \theta_y$). So, the error of the rough measurement was $16 \, \mu\text{m}$, $152 \, \mu\text{m}$, and $-0.33\,°$ (for Δx, Δy, and $\Delta \theta_z$) and $-1283 \, \mu\text{m}$ (for Δz).

At last, the virtually aligned DOPC performance was demonstrated by comparing

the PBR without correction, with rough correction alone (digital propagation with roughly measured parameters), and with fine correction (digital propagation with fine-tuned parameters). As shown in Fig. 2.8(a), no focal spot was observed on the CCD camera without correction. After rough correction, the PBR of the OPC focal spot was $\sim$60 (Fig. 2.8(b)) and it increased to $\sim$52000 after fine tuning for PBR maximization. The measured field at the sCMOS sensor array ($U_{SA}(x', y')$), transfer function including tip/tilting and displacement ($H_{SA}(f_x, f_y)|J(f_x, f_y, f_z(f_x, f_y))| \times \exp(-2\pi i f_x \Delta x) \exp(-2\pi i f_y \Delta y)$), and correspondingly digitally propagated and rotated (by $\Delta\theta_z$) field ($U_{SLM}(x, y)$) are presented in Fig. 2.6.

Here, the DOPC PBR was enhanced $\sim$870 times compared to the DOPC system corrected only with roughly measured parameters. The achieved PBR was about 30% of the theoretical PBR limit. This PBR performance is rarely achieved in manually aligned DOPC systems.
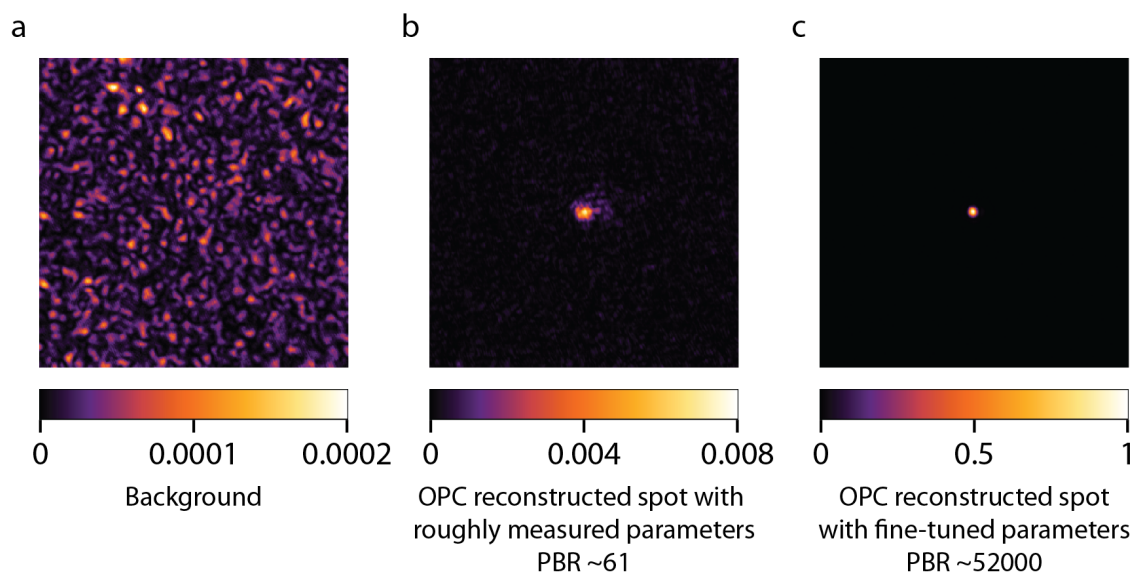
Figure 2.8: (a) Background and (b) DOPC reconstructed spot with roughly measured parameters and (c) optimized parameters (normalized by the optimized peak intensity with the fine-tuned parameter). (a) Without optimization, we observed only background as the misalignment significantly deteriorated the DOPC system. (b) With roughly measured parameters, the OPC peak was observed with low quality (PBR $\sim$61). (c) With fine-tuned parameters, the peak intensity was increased 870 times. A PBR of $\sim$52000 was observed, which corresponds to $\sim$0.31 of the ideal PBR.

2.3.2   Case Studies

Set	Roughly measured parameters $(\Delta x, \Delta y, \Delta z, \Delta\theta_x, \Delta\theta_y, \Delta\theta_z)$	Initial PBR	Fine-tuned parameters $(\Delta x, \Delta y, \Delta z, \Delta\theta_x, \Delta\theta_y, \Delta\theta_z)$	Optimized PBR
1	-5006, -1845, 17514, 0, 0, -2.39	60	-4990, -1693, 16231, -3.5, 7, -2.72 (16, 152,-1283, -3.5, 7, -0.33)	52000 (29%)
2	-2606, -2233, 8416, 0, 0, -2.87	1500	-2590, -2041, 9057, 0.5, 0.5, -2.82 (16, 192, 642, 0.5, 0.5, 0.05)	82000 (45%)
3	-2541, -2197, 3186, 0, 0, -2.85	1300	-2517, -2029, 3828, 1, -1,-2.83 (24, 168, 642, 1, -1, 0.02)	85000 (47%)
4	-177, -1315, 10801, 0, 0, -1.96	23000	-217, -1315, 11122, 1, 0, -1.8 (-40, 0, 321, 1, 0, 0.16)	97000 (53%)
5	284, -1306, 2528, 0, 0, -2.10	3600	260, -1314, 1887, 1, 2, -1.76 (-24, -8, -642, 1, 2, 0.33)	100000 (55%)
Control (PBR ~5400 w/o any correction)	22, -34, 2773, 0, 0, -0.69	170	24, -40, 3850, -0.5, -2.5, -0.09 (2, -6, 1077, -0.5, -2.5, 0.60)	120000 (66%)

Figure 2.9: Five case studies. An auto-alignment scheme was applied to five different misaligned configurations of the sCMOS sensor array and SLM. The values in between parentheses in the "Fine-tuned parameters" column are the differences between the roughly measured parameters and fine-tuned parameters. Thus, they present the accuracy of measurement on the four measured parameters. The values in parentheses in the "optimized PBR" column are the ratio of optimized PBR to the theoretical maximum, 180000. Misalignment parameters are in units of μm and degrees. As the control set, the result from a roughly aligned system is presented.

In this section, we examine the performance of our auto-alignment strategy for several scenarios (including the one already presented as Set 1 in Fig. 2.9). Figure 2.9 presents the roughly measured parameters, corresponding PBR, optimized parameters, and optimized PBR for each misaligned scenario. We have repeatedly and successfully achieved an optical phase conjugation procedure. For all configurations, PBR was recovered to more than 50000 (~30% of the theoretical maximum).

The Control set in the table shows the results we obtained while correcting a roughly aligned system (physically roughly aligned based on the roughly measured parameters). We applied our technique to the physically roughly aligned DOPC system to experimentally investigate the optimal DOPC performance which would be practically beneficial for the optimal performance of various applications, as such for the contrast of high-resolution imaging. The absolute PBR of ~120000 was achieved,

corresponding to ∼66% of the theoretical maximum.

Empirically, precision of the rough measurement was in the order of $\sim 100\,\mu$m for Δx and Δy, $\sim 0.5\,^\circ$ for $\Delta\theta_z$, and $\sim 1000\,\mu$m for Δz . In the case studies, even though the speckle coherence area was around $24\,\mu$m $\times$ $24\,\mu$m (3×3 SLM pixels), the rough measurement was sufficiently accurate to allow the initial reconstructed peak to be observed because of the memory effect of the thin scattering sample [49]. For the thick turbid media, this precision might not be good enough to render the initial reconstructed peak. However, this challenge can be simply circumvented by digitally filtering out the high spatial frequency components of the measured field. This enables the observation of the initial reconstructed peak with the correction based on the roughly measured parameters. Thus, the fine-tuning of the misalignment parameters can be applied. This process can then be repeated with the higher spatial frequency part of the measured wavefront until PBR is maximized.

2.4   Summary and Outlook

DOPC is a novel and promising technique for turbidity suppression in biomedical imaging, but the requirement for precise system alignment poses significant challenges to its practical implementation. As our data show, even small misalignments, particularly lateral shifts and in-plane rotations between the camera and the SLM, can lead to drastic reductions in DOPC performance. Here, we introduced a versatile easy-to-use method that significantly reduces the effort and time required for precise alignment. Even with untypically large misalignments of several millimeters for displacement and several degrees for rotation and tip/tilt, our method converges to optimal performance within 10 minutes. For small scale misalignments (less than a hundred μm and one degree), our fine tuning method can be completed within three minutes, which is well-suited for drift correction on a daily basis. Our system has robustly achieved optical phase conjugation with a high fidelity (PBR of 52000–120000, corresponding to 29%–66% of the theoretically achievable PBR of ~ 180000), which is comparable to that of conventional precision alignment.

It should be noted that the PBR is typically below 100% of the ideal PBR ($= \frac{\pi}{4}$,180000) even with the exact pixel-to-pixel physical/virtual matching alignment because of the following reasons: (1) There is a crosstalk between SLM pixels so that the phase of the phase-conjugated field cannot be precisely addressed. This effect becomes more significant when the phase pattern contains high spatial frequency components such as the fine speckle in our experiments (speckle granularity was around 3×3 SLM pixels). (2) Digital components such as sCMOS sensor array and SLM are pixelated. Thus, we cannot capture/display all nuances of the incoming/phase-conjugated field.

We note that some loss in PBR is always to be expected for physically misaligned systems, even with optimal correction by our auto-alignment technique. Because our method is based on the digital light propagation of optical wavefronts from the sensor plane to the SLM plane, a portion of the digitally propagated wavefront may fall outside of the virtual SLM plane (loss in information) such that the entire measured field at the sensor plane is not reproducible by the SLM. This explains the gradual drops in PBR (equivalent to the gradual drops in the effective number of DOPC pixels, P) in our experimental results as the misalignment become severe.

While such hardware limitations reduce the number of effectively controlled modes, our routinely achieved PBR of over 50000 would still provide a sufficient contrast for high resolution imaging. Furthermore, ongoing improvement of SLM hardware by the industry is likely to reduce cross-talk and increase the number of SLM pixels in the near future, which will lead to a further increase in DOPC performance.

With such hardware advances and the considerable reduction in alignment complexity and time presented in this paper, we expect that our new alignment strategy will aid the dissemination of DOPC in the field of biomedical optics.

Chapter 3

Exploiting Optical Phase Conjugation for Light Focusing

The ability to create a diffraction-limited spot (or image) can be severely limited by aberrations from optical system and specimen. Inspired by the concept of adaptive optics, we propose a method of exploiting optical phase conjugation for light focusing. This section presents two implementations of the concept where the optical phase conjugation is employed to (1) address challenges in isotropic light focusing and (2) achieve variable focusing and 3D light patterning.[1]

3.1   OPC-assisted Isotropic Focusing

Isotropic optical focusing, the focusing of light with axial confinement that matches its lateral confinement, is important for a broad range of applications. Conventionally, such focusing is achieved by overlapping the focused beams from a pair of opposite-facing microscope objective lenses. However the exacting requirements for the alignment of the objective lenses and the method's relative intolerance to sample turbidity have significantly limited its utility. In this section, we present an

---

[1]The first section of this chapter is reproduced with some adaptations from the manuscript Jang, M., Sentenac, A. & Yang, C. Optical phase conjugation (OPC)-assisted isotropic focusing. Opt. Express 21, 8781 (2013). *: equal contributions. MJ contributed to designing and conducting the experiments, analyzing the experimental results, and preparing the manuscript. The second section of this chapter is reproduced with some adaptations from the manuscript Ryu, J.*, Jang, M.*, Eom, T. J., Yang, C. & Chung, E. Optical phase conjugation assisted scattering lens: variable focusing and 3D patterning. Sci. Rep. 6, 23494 (2016). *: equal contributions. MJ contributed to developing the idea, designing the experiments, analyzing the experimental results, and preparing the manuscript.

optical phase conjugation (OPC)-assisted isotropic focusing method that can address both challenges. We exploit the time-reversal nature of OPC playback to naturally guarantee the overlap of the two focused beams even when the objective lenses are significantly misaligned. The scattering correction capability of OPC also enables us to accomplish isotropic focusing through thick scattering samples. This method can potentially improve 4Pi microscopy and 3D microstructure patterning.

3.1.1 Conventional Isotropic Light Focusing

Optical focusing is important for a broad range of applications, such as biological imaging [50–52], particle trapping [53], and optical data storage [54]. A focused light beam can typically achieve diffraction-limited transverse spot size through the use of broadly available microscope objective lenses. Interestingly, the axial focused spot size tends to be 3-5 times worse. This is attributable to the fact that single-sided optical focusing can only bring at most a hemisphere's worth of optical k-vector (spatial frequency) components to the focused spot, sufficient to create a tight transverse focus but insufficient to achieve the same along the optical axis (Fig. 3.1(a)). In the context of focused-beam scanning microscopy, such as confocal microscopy, this translates to a superior transverse resolution but a poor axial resolution.

Isotropic focusing can address this limitation by bringing in a full angular range of optical k-vector components which results in diffraction-limited spot size along all axes. Conventionally, isotropic focusing is achieved by employing two high numerical aperture (NA) objective lenses facing each other (Fig. 3.1(b)). This approach was originally proposed and demonstrated in conjunction with a confocal imaging system [55–58]. The imaging technique, so called 4Pi microscopy, improves an axial resolution 3-5 times compared to the conventional focusing technique with a single objective lens [2, 52, 55, 58]. However, the broader applications of 4Pi microscopy are limited by the following challenges. 1) The two objective lenses need to be precisely aligned so that their focused spots overlap exactly, 2) optical aberrations (including sample scattering) in the intervening medium between the two objective lenses can disrupt

the focus overlap or, worse, deteriorate either one or both of the focused beams so that the light beam(s) no longer come to the focus. This second challenge is especially problematic and restricts 4Pi imaging application to thin sample sections (∼50 microns).
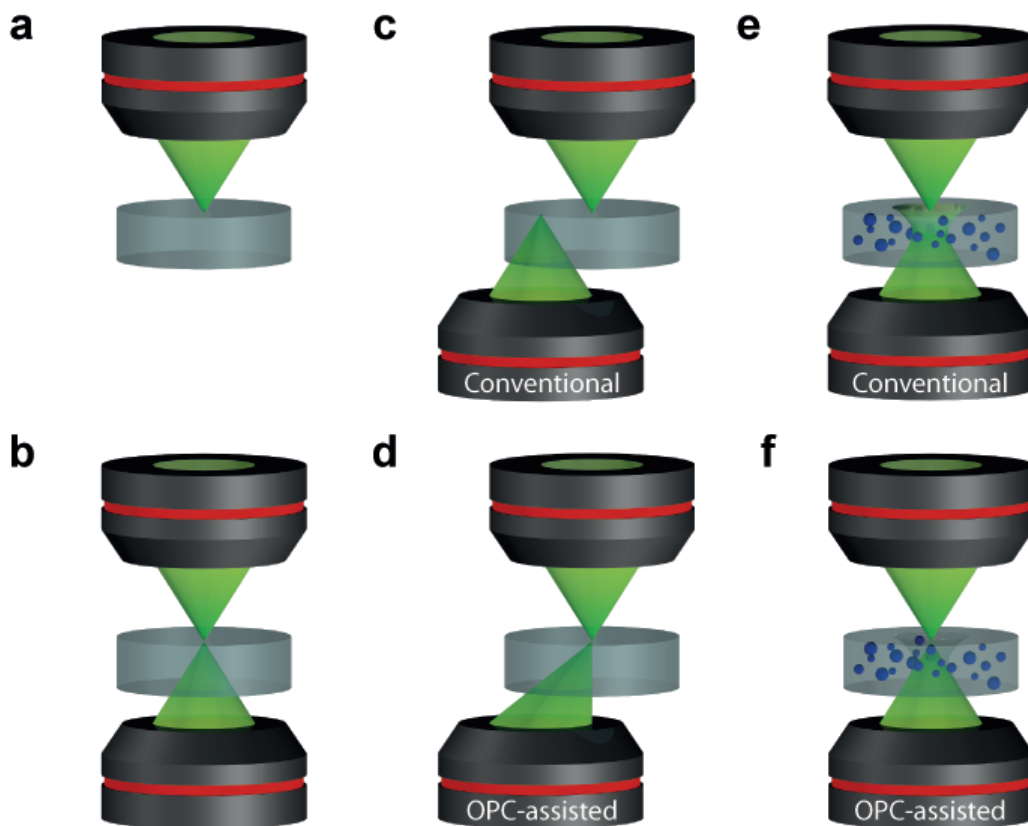
Figure 3.1: (a) Conventional unidirectional focusing scheme with single lens. (b) Conventional isotropic focusing scheme with two aligned lenses. The aperture angle (contributing k-vector components) for the focused light beam is doubled in the isotropic focusing scheme. (c-f) Conventional and OPC-assisted isotropic focusing in two circumstances (c and d) with lateral misalignment (e and f) and through inhomogeneous media. The conventional system fails to maintain isotropic focusing for both cases, while the OPC-assisted system adaptively corrects the aberrations.

3.1.2   OPC-assisted Isotropic Light Focusing

In this work, we report the application of optical phase conjugation (OPC) in an isotropic focusing scheme. Optical phase conjugation (OPC) is the process by which

an incoming light field is recorded and a phase sign-reversed copy of the light field is generated and played back. In effect, it can be interpreted as a time-reversed reflection process as the phase-conjugated field will propagate back along the original trajectory [19, 26, 42, 59, 60]. One research group recently showed that the time-reversal theory can be employed in non-adaptive way to achieve isotropic focusing simply with a single objective lens and a plane mirror [61]. However, this modification does not mollify the optical aberration challenge. In addition, while this approach eliminates the need for precise alignment of the objective lens pair, it still requires precision in mirror placement unless some form of feedback is employed. The new OPC-based approach described in this paper can dynamically overcome the abovementioned challenges.

In OPC-assisted isotropic focusing, we use the first objective lens to focus light at the desired location in the target medium. The transmitted wavefront is then collected by the second objective lens and recorded by an OPC system. The OPC system then generates a phase conjugated beam (OPC beam) back through the second objective lens. The OPC beam will retrace the original trajectory in a time reversed fashion, and thereby guarantees that it will exactly overlap with the focused beam from the first objective lens. The automatic alignment inherent in this technique resolves the first challenge. This makes isotropic focusing more robust. Additionally, the OPC beam automatically corrects for sample aberrations and therefore resolves the second challenge. To date, these have not been accomplished by other technologies.

In this paper, we report experimental demonstration of OPC-assisted isotropic focusing and showed that this scheme can indeed tackle these two abovementioned challenges - with misalignment between two objective lenses and through scattering sample. Conventional isotropic focusing methods will fail to create an isotropic focused spot in both cases (Fig. 3.1(c) and (e)). With an aid of OPC, we experimentally showed that isotropic focusing can be achieved even with misalignments of up to 140 microns and 80 microns along the transverse and axial directions, respectively (Fig. 3.1(d)). We also demonstrated that isotropic focusing can be achieved in a scattering media with $\mu_s l \sim 7$, where μ_s is the scattering coefficient and l is medium thickness (Fig. 3.1(f)). Therefore, this isotropic focusing approach can potentially

allow 4Pi microscopy to image thicker and inhomogeneous tissue sections. Amongst the other applications, this approach may also enable high-resolution laser-etching of 3D microstructure.

Experimental Setup and Principle

Our implementation of OPC-assisted isotropic focusing involved the incorporation of a digital optical phase conjugation (DOPC) into the conventional isotropic focusing scheme (see Fig. 3.2). The DOPC technique is an established optoelectronic approach for the measure of an input light field and the play back of an optical phase conjugated light field [42,60,62]. In brief, we first focused light into a target medium through the first objective lens (OBJ1) of the pair (UPLFLN 100XO2, Olympus, oil immersion type, NA 1.3). The transmitted light was then collected by the second objective lens (OBJ2) and its wavefront was measured and played back by a DOPC system. The employed DOPC system can complete a cycle of measurement and playback in less than a second and it has the capability to control many of optical modes (up to 10^6, a measure of the playback quality). The playback can be maintained for an arbitrarily long time.

The DOPC system consisted of a camera arranged to perform interferometry-based wavefront measurement (SCMOS camera, PCO), a spatial light modulator (phase-only modulating LCoS, Holoeye), and an optical phase modulator (ElectroOptic Modulator, Thorlabs) for phase-shifting interferometry [42,62]. We used a 1 telescope to optically conjugate the DOPC system to the back aperture of objective lens (OBJ2) to optimize OPC effectiveness.

We further built a conventional confocal fluorescence detection setup to examine the focused light distribution characteristics. A CCD camera (pixelfly qe, PCO) was also installed to allow observation of the transverse light distribution generated from OBJ2, though it was not a necessary component of the confocal setup. Finally, we used a nanopositioning stage (P- 611.3, Physik Instrumente) to actuate the sample as needed, such as when we perform raster-scanning of the fluorescent bead.
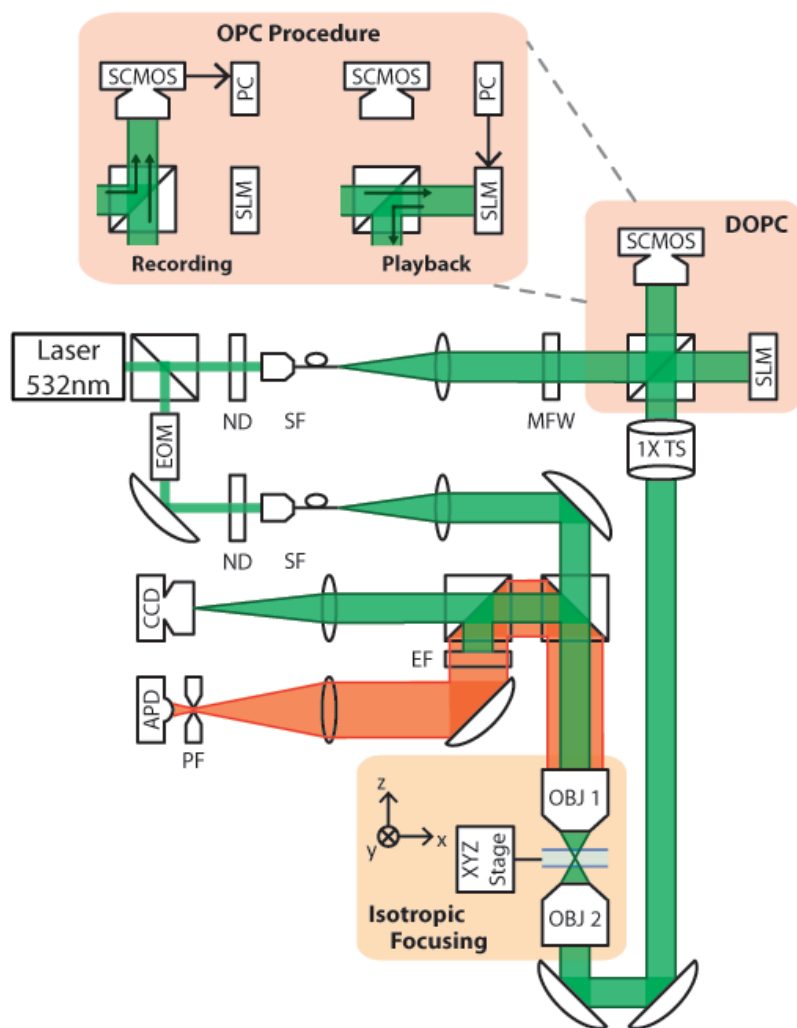
Figure 3.2: Schematic diagram of the OPC-assisted isotropic focusing system. 532 nm laser beam was split into two paths. Both beams were spatially filtered as coupled to single mode fiber and collimated by bulk lenses. One path passing the EOM formed an original focal spot through OBJ1 and entered the DOPC system, the other path was split into two beams; a reference beam for phase-shifting holography and an OPC beam retracing the original focal spot back. ND, continuous neutral density filter; SF, spatial filter; 1× TS, 1× telescope; PH, pinhole; MFW, motorized filter wheel; OBJ, objective lens; EOM, Electro-optical phase modulator; SLM, spatial light modulator; SCMOS, scientific CMOS camera; CCD, CCD camera; APD, avalanche photo diode.

We characterized the focused spot size by raster-scanning an isolated fluorescent bead (diameter 100 nm) across the focal region. The bead was embedded in anti-fade reagent (∼80 microns thick, refractive index = 1.46, Invitrogen) which was sand-

wiched between two coverslips (170 μm thick, refractive index = 1.515). A solid-state laser 532 nm laser served as the light source. We picked off the fluorescence emission collected by OBJ1 via a 50/50 beam splitter and confocally detected the signal with a spectral filter (LP02-561RS-25, Semrock) to eliminate the excitation light, a 10 μm pinhole (set at the 0.8 Airy disk diameter) to reject the out-of-focus emission light, and an avalanche photodiode (APD) detector (SPCM-AQRH-14, Perkin Elmer) to detect the emission photons from the focal spot.
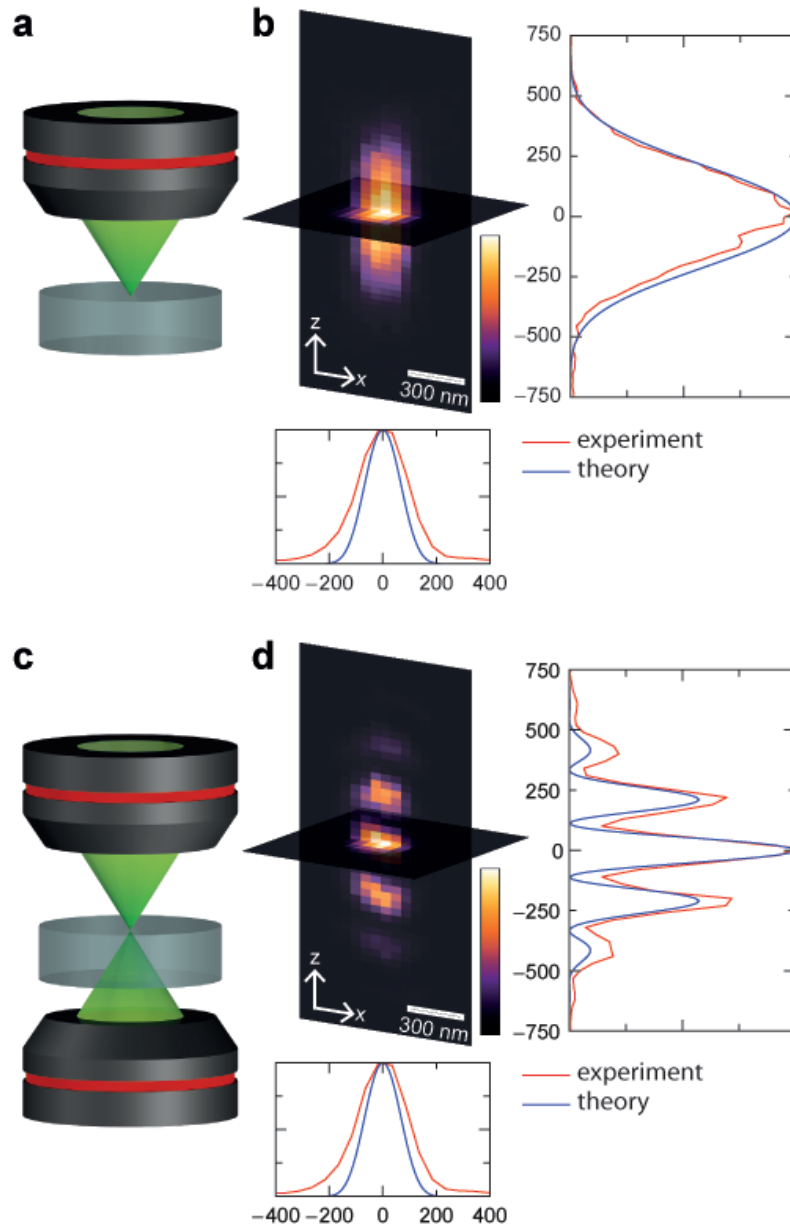
Figure 3.3: PSF of unidirectional and isotropic focusing systems. (a and c) Unidirectional and isotropic focusing schemes with single lens and two aligned lenses. (b and d) Transverse and longitudinal section of the measured PSF in conjunction with confocal detection system. 1D profiles present the axial and transverse PSF. (red line: measured profile, blue line: theoretical profile). All graphs plotted on a micron scale.

The 3D scanning of single bead was performed through the following procedures: 1) We placed a fluorescent bead at the focal spot of OBJ1. 2) We measured the phase

map of the wave front exiting OBJ2 by the means of phase shifting interferometry. 3) We then displayed the conjugated phase map on the SLM. 4) We alternately turned on only one of the beams to excite the fluorescent bead. We adjusted the power of the time-reversed beam so that the bead fluoresced with the same brightness for each of the beams. (A motorized filter wheel was used for this purpose.) 5) Next, we turned on both beams and adjusted the relative phase between two beams via the EOM to achieve constructive interference of the two focused light beams, which maximized the fluorescence signal from the bead. 6) Finally, we translated the specimen across the focal region to perform scanning. For this experiment, the excitation power of each beam was set at about $1\,\mu$W.

Through the raster-scan measurements, we were able to characterize the system point spread function (PSF), which is given by the product of the focused light distribution and confocal detection PSF. For comparison, we also measured the PSF associated with unidirectional focusing (light was focused through the first objective lens (OBJ1) and the second objective lens (OBJ2) was blocked). In addition, we also computed the theoretical light distributions near the focal region for both geometries with the use of the vectorial ray tracing model.

We experimentally found that PSF for unidirectional focusing gave a spot size (full width at half maximum, FWHM) of 200 nm and 500 nm along the transverse and axial directions, respectively (Fig. 3.3(a) and (b)). The axial spot size improved to 120 nm when we activated OPC-assisted isotropic focusing (Fig. 3.3(c) and (d)). Unsurprisingly, we observed a characteristic interference of the two counter-propagating beams that resulted in a sharpened central peak surrounded by side lobes. The 1D intensity profiles showed relatively good agreements between the experimental PSF and the theoretical PSF. The discrepancy can be attributed to the finite-sized pinhole and some aberration caused by refractive index mismatch between the embedding medium and cover slip.

3.1.3 Results

Isotropic Focusing through Two Misaligned Lenses

To demonstrate that this scheme can robustly correct for misalignment of the objective lenses, we intentionally disrupted the foci overlap by misaligning the OBJ2 in the next set of experiments. In this situation, we expected the DOPC to robustly measure the transmitted wavefront (collected through OBJ2) and playback an appropriate phase conjugated copy of the wavefront and, thereby, preserve the beam overlap.

Figure 3.4 shows the transmitted wavefront recorded by the DOPC system when the objective lenses were misaligned. As the transverse and axial displacements were increased, we observed fringe patterns and bull's eye patterns, respectively, with higher spatial frequency components. We note that the light field experiences analogous wavefront distortion when the medium consists of multiple layers with different refractive indices or has a continuous gradient of refractive index.
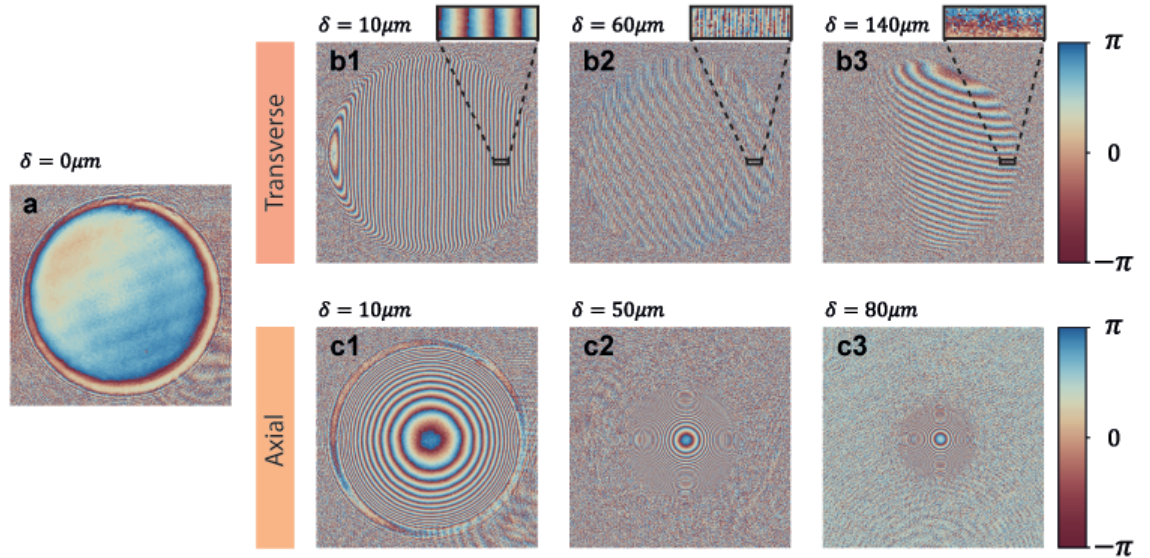
Figure 3.4: Measured wave front (phase map) exiting transversely/axially misaligned objective lens (OBJ2 in Fig. 3.2). (a) Phase map of the wave front exiting well-aligned objective lens. Flat pattern (plane light beam) was observed. (b1–b3) Phase map of the wave front exiting transversely misaligned objective lens with an incremental displacement. Fringe patterns (angularly deviated light beam) with different frequency were detected. (c1–c3) Phase map of the wave front exiting axially misaligned objective lens with an incremental displacement. Bulls eye patterns (converging light beam) were emerged. With severe misalignment, some higher spatial frequency information was missed.
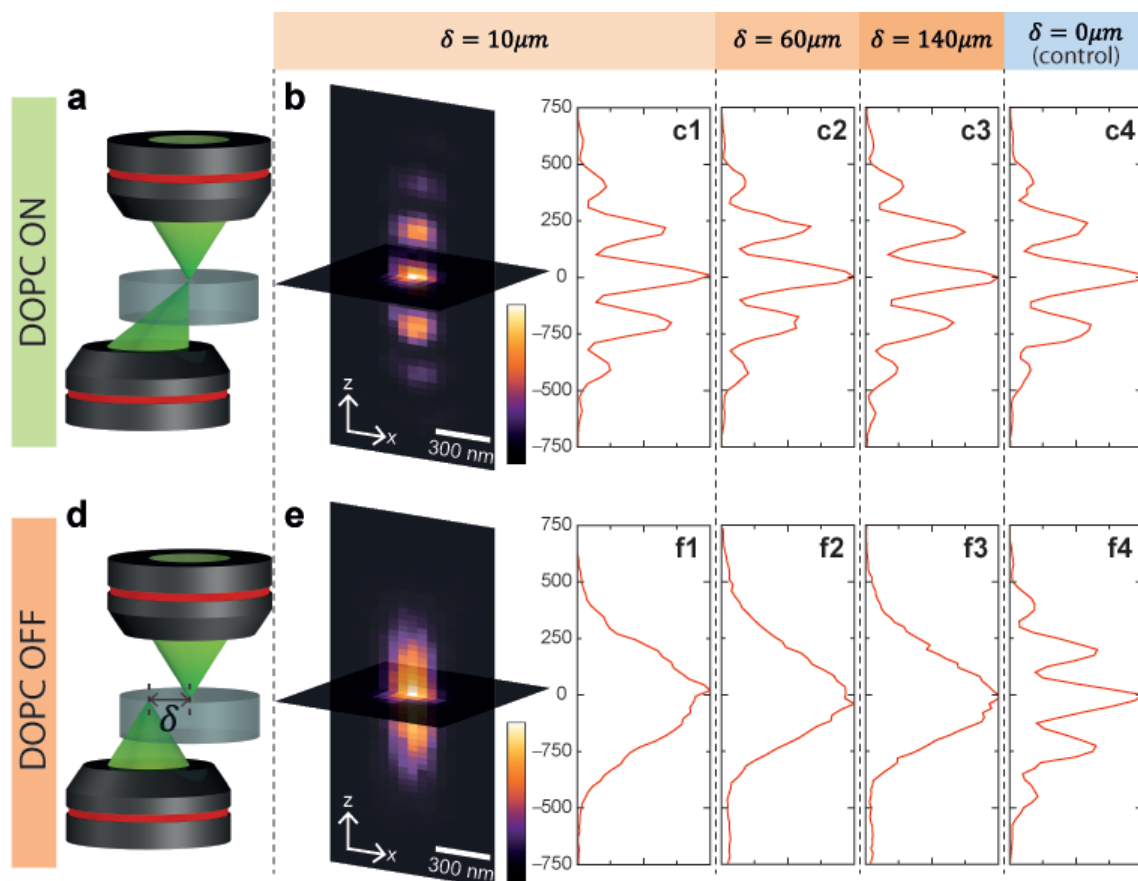
Figure 3.5: PSF of OPC-assisted and conventional isotropic focusing system with a 10 microns transverse misalignment. (a and d) OPC-assisted and conventional isotropic focusing schemes. (b and e) Transverse and longitudinal section of the measured PSFs in conjunction with confocal detection system. (c1-c3) 1D axial PSFs of OPC-assisted isotropic focusing system with incremental transverse misalignment. The OPC-assisted system robustly provided the identical PSFs with marginal errors (FWHM of 120 nm). (f1-f3) 1D axial PSFs of conventional isotropic focusing system. As two objective lenses formed two far-distant foci, the system presented the elongated profile (FWHM of 500 nm). (c4 and f4) 1D axial PSFs of two systems with well-aligned objective lenses. As a control set of experiments, axially sharpened profiles were measured for both systems. All graphs plotted on a micron scale.

Figures 3.5(b) and (c) shows the measured PSFs associated with a 10 micron transverse misalignment of OBJ2. For the sake of comparison, we also plotted the PSFs without the aid of DOPC (Figs. 3.5(e) and (f)). With the use of OPC-assisted isotropic focusing, the PSF spot size was measured as 200 nm and 120 nm along

transverse and optical axes, respectively. Without the correction, the system basically worked like a unidirectional focusing system because the two lenses formed focused spots that were too distant to overlap (10 μmu apart). We repeated the experiment with 10 microns axial misalignment. The results are shown in Fig. 3.6.
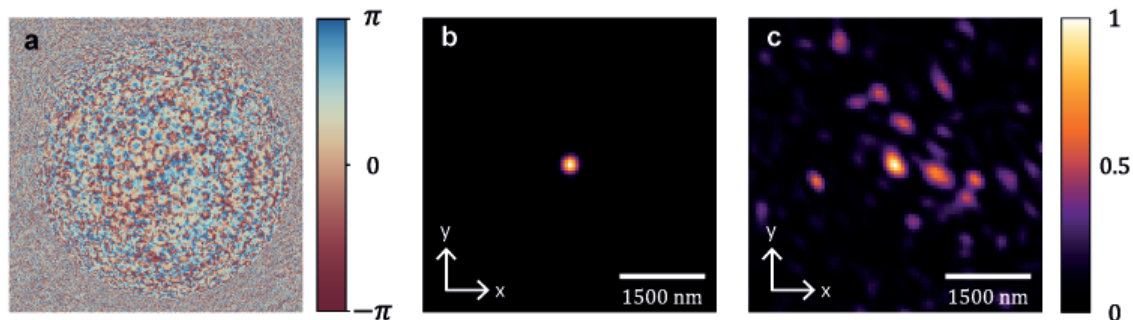
Figure 3.6: PSF of OPC-assisted and conventional isotropic focusing system with a 10 microns axial misalignment. (a and d) OPC-assisted and conventional isotropic focusing schemes. (b and e) Transverse and longitudinal section of the measured PSFs in conjunction with confocal detection system. (c1–c3 and f1–f3) 1D axial PSFs of OPC-assisted isotropic focusing system and conventional isotropic focusing system with incremental axial misalignment. (c4 and f4) 1D axial PSFs of two systems with well-aligned objective lenses. All graphs plotted on a micron scale.

Practically, we expected that the compensable misalignment range would be largely set by the wavefront pixilation during DOPC play back. Intuitively speaking, the finite pixel size on the spatial light modulator (SLM) implied that its primary diffracted beam could only cover a finite angular range. At the objective lens aperture stop, this maximum deflection angle equaled ∼1.9 degrees, which corresponded to ∼60 microns transverse focal spot displacement. However, we experimentally found that it was actually possible to maintain isotropic focusing beyond this range by employing higher diffraction orders. We do note that the power transmission to the phase-conjugated focal spot will drop as the misalignment increases. This implied that we need to increase the play back power to compensate. We confirmed that our system was able to maintain isotropic focusing up to a misalignment of 140 microns transverse misalignment (Fig. 3.5(c)). This range can be further extended by increasing the playback power beyond our system's capability. Likewise, we were able to correct up

to 80 microns axial misalignment (Fig. 3.6(c)) with our current setup. We expect that larger misalignments can be compensated if higher playback power is available.

OPC-assisted Isotropic Focusing through an Optically Inhomogeneous Medium

To demonstrate that the OPC-assisted isotropic focusing method can robustly accomplish isotropic focusing through an optically inhomogeneous medium, we conducted the following experiment.

We prepared a ∼80 microns thick slab of scattering medium consisting of polystyrene beads (refractive index = 1.60, Polysciences) of various sizes (diameter 100 nm, 200 nm, 350 nm, 500 nm, and 1000 nm) corresponding to anisotropy factors of 0.13, 0.53, 0.80, 0.89, and 0.96, respectively (calculated based on Mie theory). The mean number of scattering events was determined to be $\mu_s l \sim 7$ by the ballistic transmission measurement [63]. Fluorescent beads were embedded as well to provide PSF measurement targets.

We note that the distortion correction will only work for the play back beam. In other words, the fine focal spot needs to be created from the first objective lens (OBJ1) so that the OPC beam can retrace it from the opposite direction. This implies that the intervening medium between the first objective lens and the focal point would have to be of sufficiently low turbidity.

In this experiment, our focus was placed 10 microns into the medium (on OBJ1 side). Figure 3.7(a) shows the transmitted wavefront recorded by the DOPC system (on OBJ2 side). It presented a disordered pattern due to the multiple scattering. Unsurprisingly, the play back light was able to retrace its way through the scatterers and generate a good focal spot at the original focal region. Without the correction (plane light field from DOPC system), the light distribution was significantly disturbed (Fig. 3.7(b) and (c)). The measured PSF for both situations is presented in Fig. 3.1.3(b) and (d). Axial spot size of the PSF was enhanced to 120 nm from 500 nm with the aid of DOPC.
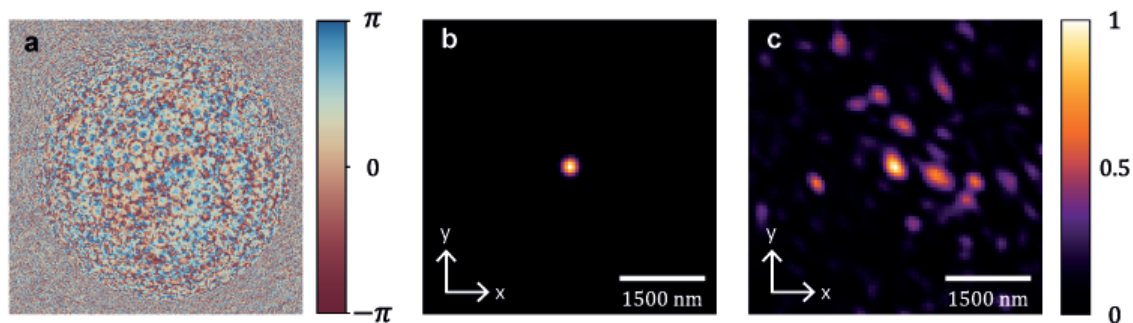
Figure 3.7: (a) Measured wave front (phase map) propagated through an inhomogeneous media with $\mu_s l \sim 7$. As the light experienced multiple scatterings, a disordered wave front was measured. (b-c) Light intensity distribution emerged from an objective lens on the side of the DOPC (OBJ2 in Fig. 3.2). Those were captured by an additional CCD sensor through OBJ1 (Fig. 3.2). (b) With an aid of the DOPC, a sharp focal spot was reconstructed. (c) Without an aid of the DOPC (plane light beam from DOPC), focal spot was significantly degraded.

If we translate the inhomogeneous medium to scan the spot through the region of interest, the phase-conjugated focal spot is gradually blurred [19,60]. This is expected as the displacement of the sample implies a change in the scatterers' configuration as seen by the DOPC system. Consequentially, DOPC needs to be performed for each different configuration of the scatterers. However, in the forward-scattering regime, which prevails in a biological sample a few hundreds microns thick, the phase-conjugated focal spot presents robustness to the sample displacement even up to a few micrometers. In our experiment, OPC was only performed four times while collecting the 0.8 micron $\times$ 1.5 micron section image shown in Fig. 3.6(b).
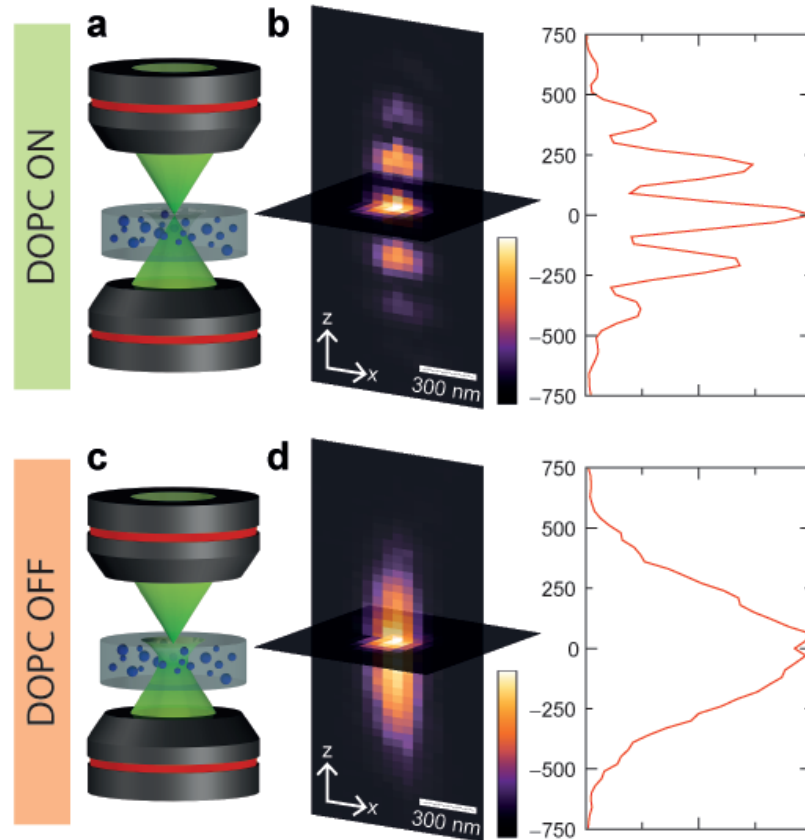
Figure 3.8: PSF of OPC-assisted and conventional isotropic focusing system through the optically inhomogeneous media ($\mu_s l \sim 7$). (a and c) OPC-assisted and conventional isotropic focusing schemes. (b and d) Transverse and longitudinal section of the measured PSFs in conjunction with confocal detection system. 1D axial PSFs clearly showed the recovery of isotropic focusing with aid of the DOPC. All graphs plotted on a micron scale.

3.1.4 Summary and Outlook

In this study, we have developed a new adaptive focusing technique, termed OPC-assisted isotropic focusing. Our prototype system demonstrated that this approach is robust against objective lens misalignment (up to 140 microns transverse and 80 microns axial misalignment demonstrated) and is capable of creating an isotropic focus even in the presence of turbidity ($\mu_s l \sim 7$ demonstrated) on one side of the focal point. We believe that the method is directly relevant in two application areas

- 4Pi microscopy and fabrication of 3D microstructure [55–58, 64].

In 4-Pi microscopy, this adaptive approach should allow more robust operations where exacting alignment of the objective lens pair can be significantly relaxed. The ability to work robustly with samples that are too turbid to image with conventional 4-Pi microscopy is another significant advantage. We note that this approach still requires the light beam from the first objective lens to be well focused, which implies that the intervening medium between the focus and the first objective lens needs to be relatively clear (the same requirement as for conventional 4-Pi). However, the method will be able to accommodate turbidity associated with the other side of the focus. This implies that this new adaptive approach will likely be suitable for performing 4-Pi imaging of superficial cells or layers on thick sample sections (such as fluorescently tagged proteins near the top or bottom of a developing embryo).

This adaptive focusing method can also address direct laser etching of 3D microstructures, such as photonic crystals. One feasible way to fabricate 3D microstructures would be to perform a focused laser beam scanning to etch planar patterns into a suitable slab of material [64]. By progressively etching and vertically compiling a vertical stack of planar patterns, we can arrive at a 3D microstructure. The use of isotropic focusing in this type of application can ensure diffraction-limited spatial resolution in three dimensions. However, conventional isotropic focusing is not a practical solution. Specifically, we can expect that, as layers of planar pattern are progressively etched into the material, they will collectively behave like a scattering medium and will disrupt one of the focused beams. As we have reported above, OPC-assisted isotropic focusing will not suffer from this shortcoming. This advancement is likely to be highly relevant to 3D photonic crystal fabrication, as such structures do generally require features that are of the optical wavelength scale along all three axes [65].

Our current experimental setup is intended only as a demonstration of the adaptive focusing method's advantages. To translate the work for applications, it is highly desirable to suppress the side lobes surrounding the central peak. This can be achieved by switching to the two-photon excitation scheme or by employing a higher NA ob-

jective lens [66]. It would also be beneficial to improve the system's speed. We expect that the use of a high speed sensor and digital micromirror device in place of a scientific CMOS (SCMOS) camera and SLM will improve the DOPC process speed to 1000 Hz (currently 5 Hz). On a different front, it will also be favorable to develop a more dynamic phase control method that can automatically lock the relative phase of the two counter-propagating beams such that optimal constructive interference can occur at the center of the focal spot.

3.2 OPC-assisted Scattering Lens: Variable Focusing and 3D Patterning

Variable light focusing is the ability to flexibly select the focal distance of a lens. This feature presents technical challenges, but is significant for optical interrogation of three-dimensional objects. Numerous lens designs have been proposed to provide flexible light focusing, including zoom, fluid, and liquid-crystal lenses. Although these lenses are useful for macroscale applications, they have limited utility in micron-scale applications due to restricted modulation range and exacting requirements for fabrication and control. Here, we propose a holographic focusing method that enables variable light focusing without any physical modification to the lens element. In this method, a scattering layer couples low-angle (transverse wave vector) components into a full angular spectrum, and a digital optical phase conjugation (DOPC) system characterizes and plays back the wavefront that focuses through the scattering layer. We demonstrate micron-scale light focusing and patterning over a wide range of focal distances. The interferometric nature of the focusing scheme also enables an aberration-free scattering lens. The proposed method provides a unique variable focusing capability for imaging thick specimens or selective photoactivation of neuronal networks.

3.2.1 Variable-focus Lens

Light focusing is typically achieved through a lens or curved mirror with a fixed focal length. The focusing optic's numerical aperture (NA) defines the depth of focus (DOF) as [2]:

$$DOF = \frac{2\lambda}{NA^2}.$$ (3.1)

Eq. (3.1) assumes a circular aperture; λ is the wavelength of light. For micron-scale light focusing with visible light (focus size of 1-5 microns at $\lambda = 532\,\mathrm{nm}$), the NA has to be in the range of 0.05–0.27, which leads to a depth of focus of 14–360 microns. Thus, for most biomedical applications that require three-dimensional (3D) optical interrogation, the specimen target section needs to be precisely aligned to the focal plane.

This problem can be circumvented with a variable-focus lens. The most common design is the zoom lens, in which the focal length is adjusted with a moving element(s). However, this approach may not be suitable for lens configurations that require exact alignment, such as an objective lens. This limits zoom lens applications in biological microscopy. Another notable approach to variable focusing is to electrically modulate the morphology or refractive index of lens element. One prominent example is the fluid lens, in which the radius of curvature of a fluid drop is modulated by external voltage [67–70]. However, the aberration and limited numerical aperture of the fluid lens restricts its applications [67].

3.2.2 Wavefront Shaping for Light Focusing

A wavefront-shaping technique provides versatile light focusing without physical modification to the optical element [71–74]. Instead, the spatial light modulator (SLM) is employed to shape the incident wavefront on the lens aperture so that a spot or multiple spots can be created at the desired location(s) in three-dimensional space. A notable strength of this technique is the ability to create multiple foci simultaneously or sequentially. This enables, for example, optical stimulation of multiple locations on a neuron [71, 73, 74], or creation of optical traps in arbitrary three-dimensional

configurations [72]. However, the controllable degrees of freedom in a SLM are not sufficient to address every possible nuance of the optical wavefront over the large aperture ($> 1\,\text{cm}$). In fact, when the 1-megapixel SLM ($1{,}000{\times}1{,}000$ pixels) is placed onto a $1 \times 1\,\text{cm}^2$ aperture, the maximum possible deflection angle through the SLM is only $sim 1.5$ degrees [$\simeq \lambda/(2 \cdot \text{pixel size})$]. Thus, the achievable focusing range is correspondingly limited.
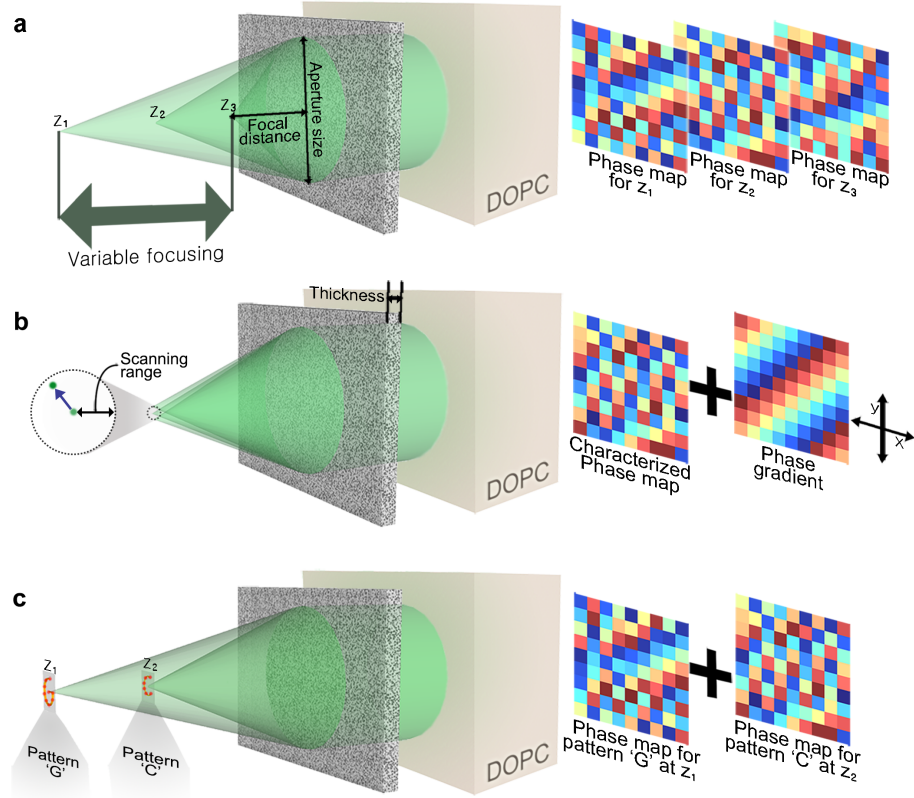
Figure 3.9: Schematic of the optical phase conjugation-assisted scattering lens. (a) Variable focusing with the OPC-assisted scattering lens. The scattering lens generates a focal spot at different focal distances by playing back the phase-conjugated version of the wavefront recorded at different focal distances, z_1, z_2, and z_3. (b) Lateral scanning of the focal spot. The focal spot can be laterally moved based on the short-range correlation (memory effect). In this case, a linear phase gradient is added to the recorded wavefront. The gradient amplitude determines the amount of displacement and the direction determines the direction of spot movement. (c) Arbitrary 3D patterning. Arbitrary 3D patterns, such as 'C and 'G at two different planes, can be created using a scattering lens by superposing multiple wavefronts that individually optimize the optical modes inside 'C and 'G.

An alternative technique was proposed by Vellekoop *et al.*, which exploits light scattering to achieve interferometric focusing [75]. In this approach, the feedback-based wavefront-shaping method is used to focus light through a scattering layer by progressively achieving constructive interference of the scattered light field at a chosen point [12, 75, 76]. This "scattering lens" enables diffraction-limited focusing (given

by aperture size and focal length) that is immune to aberration [75]. Furthermore, it is demonstrated that the focus reconstructed behind the scattering media can be laterally [77–79] or axially [80, 81] displaced by the optical memory effect [49, 82]. However, in previous works, the backing objective lens placed in between the scattering lens and the spatial light modulator significantly limits the effective aperture size of the scattering lens, which in turn limits the variable focusing capability of the scattering lens. For instance, Yang *et al.* has demonstrated that the spot reconstructed through a scattering layer can be axially displaced over the range of $\sim 300\,\mu$m for three dimensional fluorescence imaging [80].

Here, we propose an optical phase conjugation (OPC)-assisted scattering lens that generates a micron-sized focal spot over a wide range of focal distances (22–51 mm, Fig. 3.9a). The scattering lens also enables three-dimensional light patterning in micron resolution over a volume enclosed by a $\sim 20\,\mu$m $\times 20\,\mu$m circle at 22 mm focal distance and a $\sim 50\,\mu$m $\times 50\,\mu$m circle at 51 mm focal distance (Fig. 3.9c). The optical phase conjugation system is implemented with a pixel-to-pixel aligned sensor and SLM [19, 42]. The sensor in the digital OPC (DOPC) system is first used to characterize the randomized wavefront originated from the reference spot behind the scattering lens. Then, SLM plays back the phase-conjugated (time-reversed) wavefront, which is focused back to the reference spot through the scattering lens. In the characterization step, multiple wavefronts are captured at different axial positions of the reference spot and used for variable focusing. As demonstrated in the previous studies [77–81], a memory effect is used for lateral scanning (Fig. 3.9b). The OPC-assisted method enables coordination of much larger numbers of optical modes with shorter lens characterization time than the previous feedback algorithm scheme [75, 77]. This OPC-assisted scattering lens will find applications in the areas of optical imaging and selective photoactivation.

The subsequent sections are structured as follows. We first provide a detailed description of the experimental setup and procedure. We then present experimental data on the focal spot size and usable range of the scattering lens, and demonstrate sequential and simultaneous light patterning in three-dimensional space. Finally, we

discuss the limitations and practicality of the proposed scheme.

3.2.3 Experimental Setup and Principle
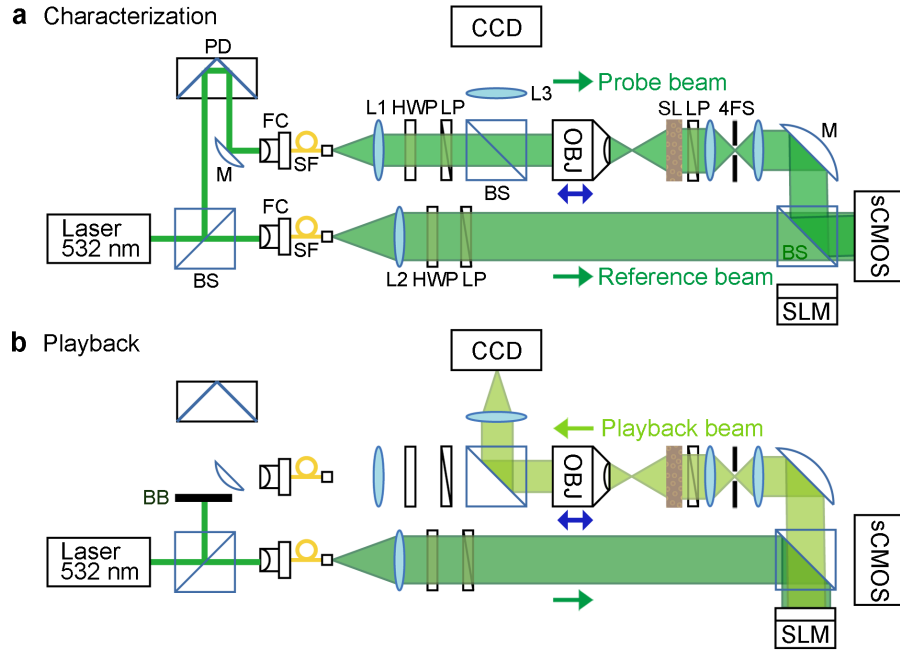
Figure 3.10: Experimental setup. The scattering lens is characterized and then used to generate a focal spot or focal pattern. (a) Characterization. A narrow beam from a 532-nm pulsed diode-pumped solid-state laser is split into a probe beam and a reference beam. The diffused wavefront of the scattered probe beam is captured by the DOPC system. The reference beam interferes with the diffused probe beam for the off-axis holography method. (b) Playback. The phase-conjugated copy of the recorded wavefront is calculated and displayed on SLM. Then, the playback beam (the reference bean reflected off the SLM) is focused through the scattering lens by the time-reversal symmetry. The focal plane of the scattering lens is imaged onto the CMOS camera. BS, beam splitter; PD, path delay part; M, mirror; FC, fiber coupler; SF, single mode fiber; L1, 300 mm lens; L2, 200 mm lens; L3, 500 mm lens; LP, linear polarizer; HWP, half-wave plate; OBJ, objective lens; SL, scattering lens; 4FS, 4-f system (from SL, 150 mm lens, iris, and 125 mm lens); sCMOS, scientific complementary metal oxide semiconductor; SLM, spatial light modulator; CCD, charge-coupled device; BB, beam blocker.

The experimental configuration for lens characterization is shown in Fig. 3.10. The probe beam is focused through an objective lens and scattered by a scattering lens, which is a $5.6\,\mu$m thick layer of ZnO particles (white paint) sprayed onto a standard glass microscope slide. Based on the scattering coefficient of the white pigment ($\sim 1.3\,\mu$m^{-1}) [77, 83], we estimate that the light is scattered an average of $\sim$7 times and creates a Lambertian scattering from the other side of the scattering lens. The digital OPC system, which is imaged onto the scattering lens surface through the 4-f system (with $1.2\times$ magnification), collects the scattered wavefront. Here, the collimated reference beam interferes with the scattered probe beam so that the complex wavefront can be measured with an off-axis holographic method [84]. The iris in the 4-f system selects the off-axis component to be recorded and played back. The linear polarizer and wave plate are used to match the polarization angle of the probe beam and reference beam. We repeatedly characterize the scattering lens at focal distances ranging from 2251 mm by translating the objective lens along the optical axis. We then conjugate the recorded wavefront and play it back from the SLM. The same reference beam used for the holographic measurement serves as a playback beam. The reconstructed focal spot or pattern is then imaged onto the CCD camera through an objective lens and tube lens (L3). The probe beam is blocked during this process.

The focusing fidelity is quantified by the enhancement factor, which is defined as the ratio between the intensity contained in the focal spot and the average background intensity. In contrast to conventional focusing schemes, background is inevitable in the interferometric approach. This is attributed to partial measurement of the wavefront emerging from the scattering lens. In other words, the deviation from the perfect phase conjugation randomly contributes to the background while the portion of playback field overlapped with the perfect phase-conjugated field forms a converging spherical wavefront (aberration free due to the time-symmetry of the Green function) [77]. If only the input field phase is controlled in the time-reversal process, the enhancement factor has the following relation to the number of controllable input modes (N) [12]:

$$\eta_1 = \frac{\pi}{4}N, \tag{3.2}$$

where the subscript 1 denotes that a single optical mode (i.e. focal spot) is reconstructed through the time-reversal process. In our experiment, N was $\sim$40,000 (see Methods for the determination of N). Thus, from Eq. (3.2), we estimate the theoretical η_1 of $\sim$31,000.

When we generate a light pattern composed of K optical modes, we add K input wavefronts that independently optimize each optical mode behind the scattering lens. Therefore, $1/K$ energy from the input side contributes to the light intensity at each optical mode in the desired light pattern. Mathematically, the enhancement factor of the light pattern (here, the ratio between the average intensity contained in each focal spot and the average background intensity) is given by

$$\eta_K = \frac{\eta_1}{K} = \frac{\pi}{4}\frac{N}{K}. \tag{3.3}$$

3.2.4   Results

Focal Spot Size at Different Focal Distances
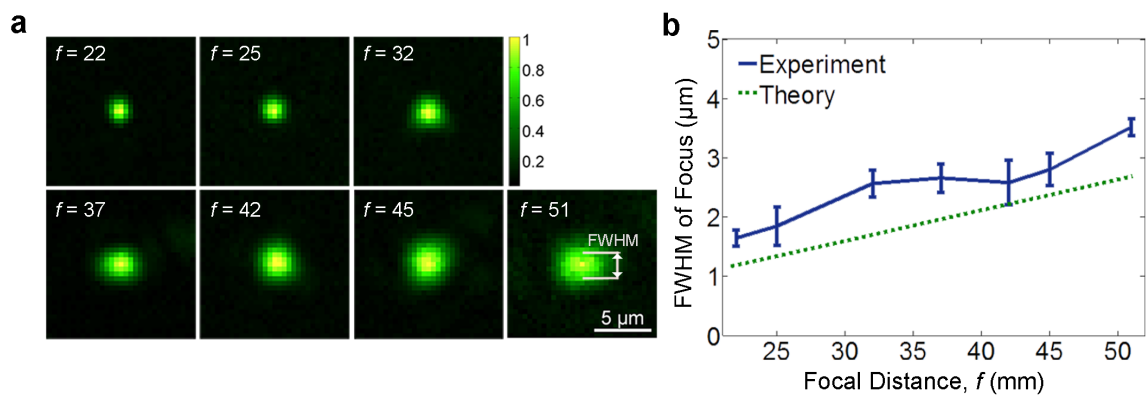
Figure 3.11: Variable focusing through OPC-assisted scattering lens. (a) Images of focal spot at different focal distances. Each image is normalized with respect to peak intensity. (b) Theoretical and experimental full width at half maximum (FWHM) of the focal spot at different focal distances.

We first demonstrate the variable-focusing capability of the OPC-assisted scattering lens (Fig. 3.9a). The scattering lens is characterized for focal distances ranging from 22–51 mm. Then, we play back each captured wavefront to create the focal

spot at each focal distance. The lateral intensity distribution and the full width at half maxim (FWHM) of the reconstructed focal spot at different focal distances is presented in Fig. 3.11. FWHM ranges from ~ 1.5–$3.5\,\mu$m, which corresponds with an NA of $\sim 0.08 - -0.18$. The focal spot size linearly increases with increasing focal distance. Because the aperture size of scattering lens is fixed, the effective NA is inversely proportional to focal distance. The theoretical relation is given by

$$\text{FWHM of the focal spot} = 0.51\lambda/NA = 0.51\lambda/\sin\left[\tan^{-1}\left(d/2f\right)\right], \qquad (3.4)$$

where d is the aperture size of scattering lens ($\sim 10\,$mm with $1.2\times$ magnification of the 4-f system). We expect the deviation from the theoretical prediction is mostly from the marginal distortion of the reference wavefront. The distortion can lead to inaccurate wavefront measurement and playback, which was performed based on the assumption that the reference wavefront is perfectly flat. With the presence of short-range correlation, the unwanted distortion in the wavefront may contribute to the light intensity in the vicinity of the original spot. We also note that the misalignment and aberration of the tube lens (L3) may cause an additional blurring in detection point spread function. The enhancement factor η_1 ranges from 2,500–8,000, depending on alignment quality. It corresponds to the 8$\sim$25 % of the theoretical η_1 from Eq. (3.2).

Lateral Scanning Range at Different Focal Distances
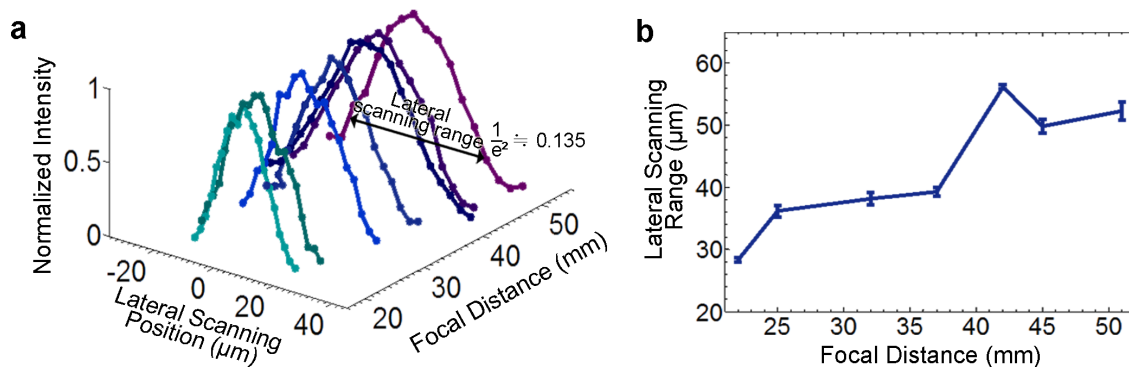
Figure 3.12: Lateral scanning range of the OPC-assisted scattering lens. (a) Normalized peak intensity of the focal spot at different lateral scanning positions and focal distances. (b) Theoretical and experimental full width at $1/e^2$ of the intensity profile at different focal distances.

Similar to the previous studies [77–81], the focus was laterally shifted by merging the captured wavefront with the linear phase gradient (Fig. 3.9b). Figure 3.12a plots the normalized peak intensity of the focal spot at different lateral scanning positions and focal distances. The lateral scanning range, which is obtained as full width at $1/e^2$, was measured to be 28~56 microns (Fig. 3.12b). As theoretically expected, the angular scanning range was not affected by focal distance. Consequently, the lateral scanning range linearly scaled with the focal distance.

Demonstration of Light Patterning
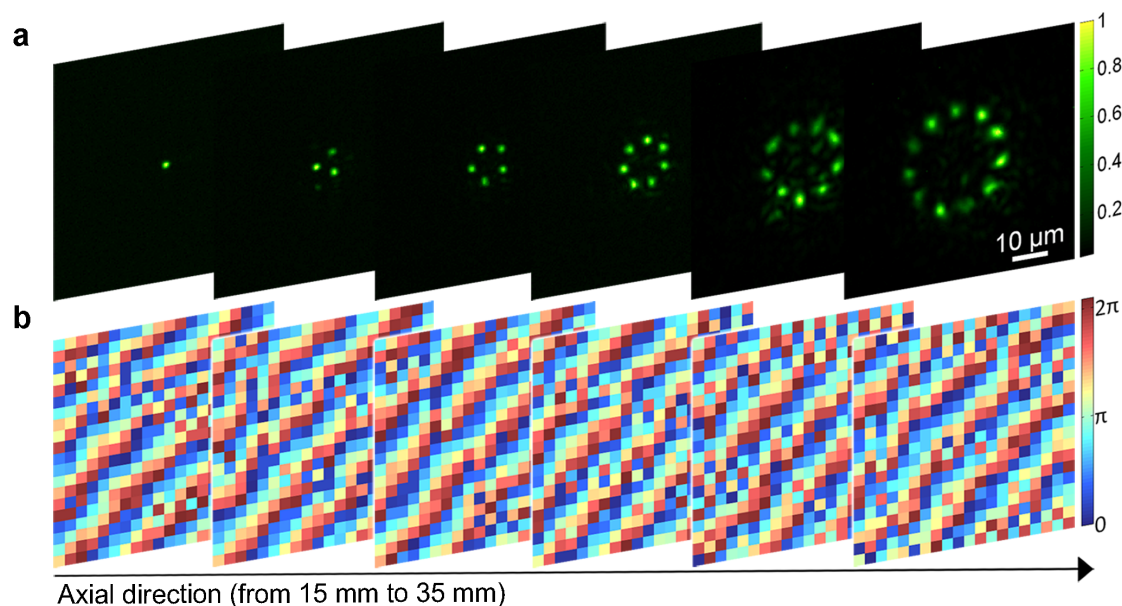
Figure 3.13: Sequential generation of multiple focal spots at different focal distances. The focal distance is changed from 15 to 35 mm with 5-mm intervals. The wavefronts at each focal distance were recorded. Then, the phase maps for multiple foci were synthesized and played back separately. (a) Images of multiple foci at different focal distances. Each image is normalized with respect to peak intensity. (b) Phase map shown for each focal distance. The phase map is cropped into 20×20 pixel images for display.

We demonstrate arbitrary light patterning based on the superposition principle. First, we sequentially create multiple focal points at different focal distances by adding multiple phase gradient maps into a single phase-conjugate wavefront (Fig. 3.13a). The synthesized wavefronts are shown in Fig. 3.13b. We observe a noticeable deformation in the focal spot and ghost spots in some patterns. These unwanted effects can be significantly suppressed by controlling the amplitude term in addition to the phase term. With the imperfect wavefront modulation and reduction in the short-range correlation, the enhancement factor η_K is reduced $\sim$20 times as the number of reconstructed focal spots increases from 1 to 11.

In practice, the maximum number of possible optical modes depends on the ap-

plication. For example, if the scattering lens is used for selective optogenetic stimulations, η_K (η_1/K) of 100 is required for 5-fold modulation of the maximum neural response [85]. In this case, the maximum number of possible optical modes that can be optimized through the scattering lens is > 20.
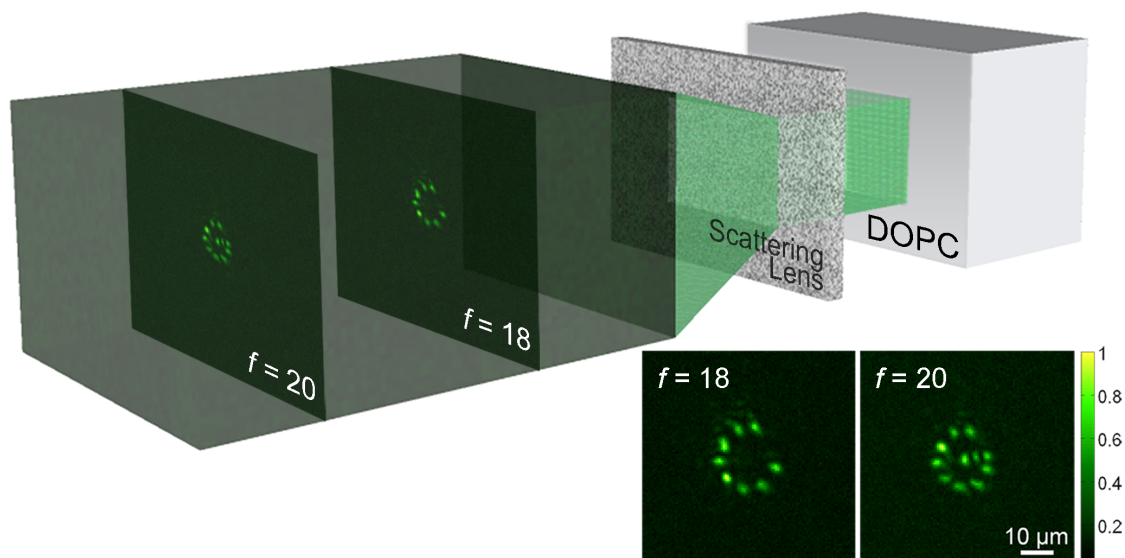
Figure 3.14: Simultaneous generation of arbitrary patterns at different focal distances. Volumetric 3D image shows the intensity distribution at different focal distances. The image is normalized with respect to the peak intensity. Insets present the patterns 'C and 'G generated at focal distances of 18 and 20 mm, respectively.

The simultaneous generation of 3D arbitrary patterning through the scattering lens is illustrated in Fig. 3.14. The phase maps for 'C and 'G are synthesized separately based on two wavefronts captured at two different focal distances (18 and 20 mm). Then, the two phase maps are superposed and displayed on the SLM. We confirmed that the patterns 'C and 'G are created 18 and 20 mm behind the scattering lens through the translating objective lens.

3.2.5 Summary and Outlook

In this study, we have demonstrated that the OPC-assisted scattering lens can serve as a variable focusing lens. Although the scattering layer does not essentially increase the

number of controllable degrees of freedom (which is determined solely by the SLM), it provides a great deal of flexibility in selecting a focal distance by redistributing the intrinsic controllable degrees of freedom in SLM into a full angular spectrum. The $10 \times 10\,\text{mm}^2$ wide aperture provides a micron-scale focal spot with variable focal length from 22–51 mm. Short-range correlation enables lateral shift of the spot with simple modification of the characterized wavefront. Using a digital wavefront shaper, we superposed multiple wavefronts to generate the arbitrary light pattern in three-dimensional space. Similar to other lenses equipped with wavefrant shaping methods [75,77,80,86,87], the OPC-assisted scattering lens corrects aberrations. The larger the lens aperture, the more flexibility the lens will provide. In principle, larger apertures are achievable with higher magnification of the relay system between the DOPC plane and the scattering lens.

We achieved variable focusing with the multiple wavefronts characterized with the point sources at different distances from the scattering lens. Alternatively, variable focusing can be achieved through the longitudinal memory effect with a single wavefront solution. As demonstrated in the previous studies [80, 81], the wavefront solution synthesized with a quadratic phase profile can be used for longitudinal scanning. However, we note that in our experimental configuration the longitudinal correlation range (in geometrical optics approximation, $\lambda f^2/\pi a L$, where f is focal distance, a is aperture size, and L is the thickness of scattering lens) is an order of magnitude shorter than the variable focusing range we demonstrated in our study.

In our system, the lateral focusing range is approximately 25–50 μm when it is defined as full width at $1/e^2$ of the peak intensity (without lateral scanning). However, the η_1 corresponding to the peak intensity is $\sim$2,500–8,000, and η_1 will be sufficiently high for most applications even with a 1/100 reduction. Thus, in practice, the usable field of view of our scattering lens can be extended to $\sim$40–100 μm. The lateral scanning range can be further improved by attaining full short-range correlation with better alignment between the SLM image plane and scattering layer or by increasing the number of characterization points on the transverse plane.

The scattering lens is ineffective in terms of power transmission. The power trans-

mission depends on the type and thickness of the scattering layer and the number of controllable optical modes. For instance, in our experiment, $\sim 10^{-7}$–10^{-8} of total power impinged on the input side was delivered to the focal spot. Although the power transmission is not effective through a scattering layer, considering the optical power distribution within the usable field of view, more than 50% of the power is focused to the target spot(s). The absolute power delivered to the focal spot(s) can be arbitrarily controlled by adjusting the power of the playback beam.

The OPC-assisted scattering lens provides great flexibility for variable-light focusing and light patterning, and can be used for a broad range of optical applications. First, it can serve as illumination optics for fluorescence microscopy. It has a unique capability for focusing light through thick specimens such as CLARITY-cleared tissue [88]. In the imaging applications, an array of focal spots along with fast scanning from a galvo mirror and digital micromirror device (in place of the SLM), will significantly improve the imaging speed. In addition, axial resolution can be further extended with an isotropic focusing scheme, which can be simply achieved in the current setup by allowing the reference spot (probe beam) to interfere with the reconstructed focal spot (playback beam) [55, 86]. In addition to its application in imaging, the scattering lens can be a powerful tool for manipulating particles and activating biomolecules or materials. For example, it can be combined with optogenetics technology for interrogating three-dimensional neuronal networks at cellular resolution [89].

In practice, a potential difficulty in using the scattering lens is that the characterization step requires a high-quality objective lens and is time-consuming when the number of characterization points is large. One direction worth pursing for future research is to develop a strategy for self-characterization of scattering lenses [90].

Appendix to Section 3.2

Setup

A pulsed laser beam (532 nm wavelength, 5 ns pulse width, 2 kHz repetition rate, 7 mm coherence length) generated from the Q-switched laser (FQS-200-1-Y-532, Elforlight) was split into a probe beam and a reference beam. The probe beam was focused through the objective lens (magnification ×10, NA 0.25, PLN 10×, Olympus) and transmitted through the scattering layer. The transmitted probe beam was relayed to the CMOS sensor or the DOPC system through the 4-f system and interfered with the reference beam. The diameter of the iris placed in between two lenses of 4-f system was around 3 mm. The phase map of the probe beam is calculated through the off-axis method and stored in a computer. The characterization step is repeatedly performed at multiple locations of the reference spot along the optical axis. The motorized stage was used to precisely position the objective lens. Then in the playback step, the SLM (Pluto, Holoeye) of the DOPC system displayed the conjugated wavefront to generate single or multiple spots through the scattering layer. Although we used a pulsed laser in our experiment, a continuous wave laser (with a single longitudinal mode) would be a preferable choice as it typically has a longer coherence length.

The DOPC system is optimized through the digital auto-alignment method [91]. Through the experiment, we achieved the experimental enhancement factor for single focus (η_1) and multiple foci (η_K) corresponding to 4–25% of the theoretical values. We speculate the discrepancy may be due to the cross talk between SLM pixels and the loss of sub-pixel nuance in a speckle field. The reduction in the short-range correlation further decreases the enhancement factor of multiple foci (η_K). The objective lens was also used to visualize the focal plane of the scattering lens. Imaging magnification from the focal plane of the scattering lens to the CCD sensor (GC655, prosilica) was characterized by a Ronchi ruler (200 lp mm^{-1}, Edmund Optics).

Determination of the Number of Controlled Optical Modes

The number of pixels we controlled in the experiment was 1654×1080. Once the separation between the off-axis component and the zero order component in Fourier space is optimized, we cropped the elliptical region (major axis of $\sim$150 pixels and minor axis of $\sim$85 pixels) in the Fourier space to extract the phase conjugation component. We estimated the number of controllable degrees of freedom as the number of pixels in the cropped Fourier component, which is around $\sim$40,000.

Diffuse Sample Preparation

The scattering lens was prepared by spray painting ZnO particles onto a standard microscope slide. The ZnO layer thickness was $5.6\,\mu$m. The thickness was measured by the surface profiler (Alpha-step IQ, KLA-Tencor).

Determination of Spot Size and Scanning Range

The one-dimensional intensity profile of the focal spot is extracted from the image of the focal spot captured from the CCD sensor. The intensity profile was fitted to the one-dimensional Gaussian profile. The spot size was then determined as the FWHM of the fitted Gaussian profile.

The one-dimensional scanning profile was acquired by sampling the peak intensity of the focal spot at different lateral scanning positions. The scanning profile was normalized and fitted to the functional form of $C(x) \simeq x^2/\sinh^2 x$ [49,82]. Then, the full width at $1/e^2$ of the fitted curve was determined as the lateral scanning range.

Impact of Thickness of Scattering Medium

Since the phase conjugation plane is optically located on the surface of scattering lens, we are able to laterally move the focused spot by simply adding a linear phase gradient on the conjugated wavefront. Theoretically, the short range correlation (memory

effect) has the following dependence on the tilting angle [49, 82]:

$$C\left(\theta\right) \simeq \left[\frac{(2\pi\theta L/\lambda)}{\sinh\left(2\pi\theta L/\lambda\right)}\right]^{2}, \tag{3.5}$$

when the tilting angle is small. θ is the tilting angle and L is the thickness of scattering lens. Thus, the intensity of the spot is dropped by $1/e^2$ when the tilt angle is

$$\theta_{1/e^2} \simeq 0.43\lambda/L. \tag{3.6}$$

Then, the corresponding scanning range (Δ) is given by

$$\Delta \simeq 2\theta_{1/e^2}f \simeq 0.86\lambda f/L, \tag{3.7}$$

where f is the focal distance. That is, the lateral scanning range linearly increases with the focal distance, f.

Chapter 4

Modeling Time-Reversed Ultrasonically Encoded Optical Focusing: Estimation on Penetration Depth

The time-reversed ultrasonically encoded (TRUE) optical focusing technique is a method that is capable of focusing light deep within a scattering medium. The theoretical study, provided in this chapter, aims to explore the depth limits of the TRUE technique for biological tissues in the context of two primary constraints: the safety limit of the incident light fluence and a limited TRUEs recording time (assumed to be 1 ms), as dynamic scatterer movements in a living sample can break the time-reversal scattering symmetry. This study sheds light on the allocation of photon budget in each step of the TRUE technique, the impact of low signal on the phase measurement error, and the eventual impact of the phase measurement error on the strength of the TRUE optical focus.[1]

---

[1]This chapter is reproduced with some adaptations from the manuscript Jang, M., Ruan, H., Judkewitz, B. & Yang, C. Model for estimating the penetration depth limit of the time-reversed ultrasonically encoded optical focusing technique. Opt. Express 22, 5787807 (2014). MJ contributed to developing the idea, implementing the computational model, analyzing the numerical results, and preparing the manuscript.

4.1 Time-Reversed Ultrasonically Encoded Optical Focusing

Because biological tissues are optically turbid, biomedical optical techniques have very limited penetration depth. The depth limit is essentially given by the characteristic length at which photons lose their directionality (one transport mean free path). Although it depends on the type of tissue and the light wavelength, this accessible depth is typically around one millimeter [92] or less. Thus, when used noninvasively, the utility of optical techniques in research and diagnosis has long been restricted to the superficial layers of tissue.
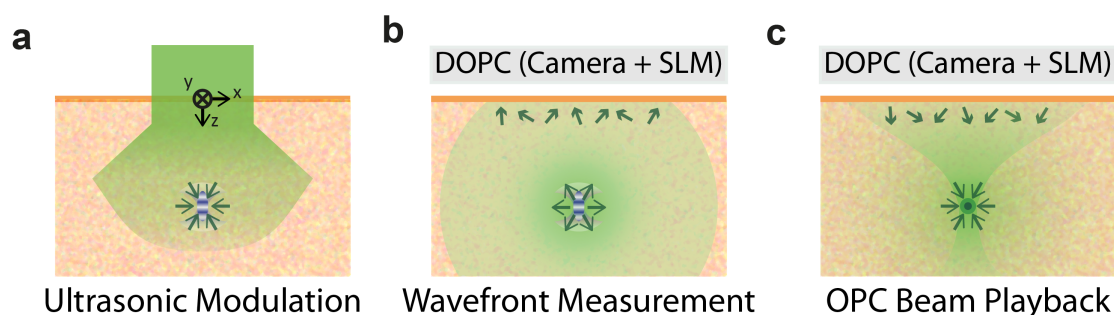
Figure 4.1: Schematic of the TRUE focusing principle with digital optical phase conjugation system (DOPC). (a) Collimated incident beam propagates through scattering medium. Light component passing through the ultrasound focus is encoded with ultrasound frequency. (b) Ultrasound-modulated light propagates back to the tissue surface. The distorted wave front is measured by a sensor in the DOPC system. (c) Spatial light modulator (SLM) reproduces a phase-conjugated copy of the measured wave front. The OPC beam with time-reversal characteristic is focused back into the US spot.

During the past few years, there has been considerable effort to break this limit using the technique of time reversal of ultrasonically encoded light, which combines ultrasonic light modulation with optical phase conjugation (OPC) [45, 93–95]. OPC is an optical process by which an incoming wavefront is reproduced and propagated back so that the phase-conjugated light wave can retrace the original light wave in the reverse direction (time-reversal property). In TRUE, the ultrasound is focused

deep inside a tissue sample, while the tissue is illuminated by a laser beam. Diffuse laser light reaching the US focus is then frequency-shifted by the acousto-optic effect [96], which serves as a tag. Tagged US frequency-shifted light leaving the sample is selectively detected and phase-conjugated. Due to the time-reversal symmetry of light propagation, phase-conjugated light in turn propagates back to the ultrasound focus, where it creates an optical focus.

Recently, TRUE has been experimentally achieved by both analog and digital OPC systems. Analog method utilizes nonlinear optical phenomena such as Brillouin scattering and nonlinear susceptibility of photorefractive media [19, 62, 93]; on the other hand, the digital method (DOPC) is implemented with digital devices - wavefront sensor and spatial light modulator (SLM) [41, 42, 45, 94, 95]. The principle of the DOPC-based TRUE focusing technique is described in Fig. 1. The demonstration of deep-tissue light focusing with DOPC has been made with a resolution of $\sim 40\,\mu$m at a depth of $2.5\,$mm inside biological tissue [45].

4.1.1 Restrictions on *In Vivo* Applications

In principle, with perfect wavefront measurements, the TRUE technique could create an optical focus even tens of centimeters deep in the human body. However, there are two important constraints that fundamentally limit the penetration depth of the TRUE focusing technique for living tissue applications. First, the incident light fluence per pulse at the tissue surface has to be smaller than the tissue damage threshold ($20\,$mJ$\,$cm^{-2} according to the ANSI medical safety standard [97]). We note that a pulsed light source is assumed as it yields more photons under the safety standard. Second, wavefront measurement and OPC playback (in Fig. 4.1) should be performed within a short time-window, before the movement of scatters significantly changes the tissue (as an optical object), thereby destroying the time-reversal symmetry. This sample-dependent time-window, which is also called the decorrelation time(t_{dec}), depends on the sample stability and depth. For most living tissues, it ranges from several milliseconds to seconds [62, 98, 99]. In our analysis, we will

consider a TRUE recording time of period $t_{rec} = 1\,\text{ms}$. We assume this time to be significantly shorter than t_{dec}. In the event that a shorter t_{dec} requires a shorter t_{rec}, the analysis in this study can be rescaled in a straightforward fashion, as the total signal photon budget is simply proportional to t_{rec}.

These two restrictions (one on incident light intensity and the other one on wavefront recording time) limit the incident photon number and, in turn, the number of frequency-shifted photons that can be collected at the surface for the wavefront measurement. As the signal level decreases with increasing tissue depth, shot-noise deteriorates the validity of the wavefront measurement and, in turn, the contrast and intensity of the TRUE focus.

In this study, we developed a numerical model to calculate the penetration depth limit of the TRUE technique given by the abovementioned constraints in living tissue applications. Our analysis is not meant to be exhaustive. One of its purposes is to establish a basic model system for understanding the interplay between various optical and ultrasonic parameters in determining the useful focusing depth of TRUE. A reader interested in a particular optical geometry, more sophisticated modeling assumptions, or a specific set of constraints can adapt our model for his/her respective purpose.

Additionally, this paper is aimed at elucidating the fundamental optical limitations of the TRUE focusing technique given by shot noise at low signal level, rather than focusing on limitations associated with current technical hurdles. For this purpose, we specifically modeled the TRUE system, implemented with digital version of the OPC system, with idealized fidelity. The idealized assumptions used here are listed in Section 4.2; we also compare the current technical limits to these assumptions in that section. We note that modification would need to be made on our model if the reader desires to investigate the effect of shot noise on an analog OPC system, as those systems exploit nonlinear optical phenomena to achieve their effects. There are likely more restrictive constraints that would have to be considered in that scenario.

The numerical simulation of TRUE developed here consists of the following steps, which are detailed in the Methods section: First, we simulate light propagation from the tissue surface (at the safety limit and within t_{rec}) to the deep-tissue US focus with

diffusion approximation. Second, the amount of US frequency-shifted light is determined using the Raman-Nath theory. Third, the intensity of frequency-shifted light propagating back to the surface is determined and used to calculate the detection shot-noise. Finally, we determine the relationship between shot-noise and focus contrast (peak-to-backgroud ratio, PBR) and determine that the practical depth limit of DOPC is in the range of 30–100 mm with the parameters under our consideration. We expect that our model will provide a framework to check the feasibility and performance of potential applications of the TRUE technique.

The subsequent sections are structured as follows. The next section describes the model geometry, assumptions, and full details of the methods with a flow chart. We will then present the numerical result regarding the dependence of the photon budget and PBR on the target depths. Finally, we will determine the fundamental depth limit from the result and discuss the utility of our model.

4.2   Simulation Model

4.2.1   Model Geometry and Assumptions

Model Geometry

Due to its relevance for biomedical imaging, a backscattering geometry is considered in this numerical study. The specific physical model geometry we are considering here is shown in Fig. 1. The target sample is a semi-infinite tissue phantom.

We assume that the DOPC system abuts the sample at its interface. For the sake of simplicity, we blackbox the DOPC and simply assume that the system is able to record the wavefront of the backscattered light exiting the interface with high fidelity and is also able to generate a corresponding phase-conjugate wavefront with high fidelity for playback. We assume that the DOPC is able to span $20 \, \text{cm} \times 20 \, \text{cm}$ of the interface surface to ensure that most of the ultrasound-modulated light is captured by the DOPC system. The wavefront measurement is assumed to be performed via interferometry where the reference beam's phase is stepped in quadrature [44] as done

in previous works [41, 45, 62, 94, 95]. Thus, the wavefront recording time is divided into four sensor exposure periods of $0.25\,\text{ms}(= t_{rec}/4)$ for each interference pattern. Idealized assumptions will be detailed in Section 4.2.1.

With regard to the incident light, we assume that the probe light field has a width of $5.1\,\text{cm} \times 5.1\,\text{cm}$ and fluence per pulse at the ANSI safety limit of $20\,\text{mJ}\,\text{cm}^2$. To perform quadrature interferometry within our specified time window of $1\,\text{ms}$, the pulse repetition rate would have to be $4\,\text{kHz}$. The pulse duration (p_{dur}) does not affect the result as long as it is sufficiently short compared to the ultrasound pulse. The cases at three wavelengths, 532, 633, and $800\,\text{nm}$, are studied. The corresponding sample absorptive attenuation coefficients are 0.038, 0.008, and $0.005\,\text{mm}^{-1}$, and reduced scattering coefficients are 0.33, 0.24, and $0.17\,\text{mm}^{-1}$, respectively [100]. In this study, we mainly present plots of the results for wavelength of $800\,\text{nm}$; of the three wavelengths, $800\,\text{nm}$ leads to the greatest penetration depth.

Coordinate system	Cartesian coordinate system is used. The origin is set on the center of the incident light field on the tissue surface. xy-plane is on the tissue surface. And, z-axis is normal to the surface pointing toward the inside of the tissue.	
Incident light	Fluence per pulse (uniform)	$= 20\,mJcm^{-2}$
	Beam width	$= 5.1\,cm \times 5.1\,cm$
	Total energy per pulse	$= 0.52\,J$ $= 2.1 \times 10^{18}$ photons
	Pulse duration	$= 10\,ns$
	Light wavelength (λ	$= 800\,nm$
Point sources sampling the incident light	Point source spacing	$= 0.2\,mm$
	Number of point source	$= 676$
	Energy per the point source (E_{point})	$= 8 \times 10^{-6}\,J$
Ultrasound	Ultrasound frequency	$= 50\,MHz$
	Ultrasound wavelength (λ_{US})	$= 30\,\mu m$
	Pressure at the ultrasound focus (P)	$= 2.35\,MPa$
	Surface area of US spot ($A_{US} = \pi \lambda_{US}^2 / 2$)	$\approx 1410\,\mu m^2$
Emerging speckle field	Speckle size ($(\lambda/2)^2$)	$\approx 0.16\,\mu m^2$
	Grid cell spacing (at which emerging photon number is evaluated)	$= 0.1\,mm$
	Number of modes (speckles) on a grid cell (M_{grid})	$= 6.25 \times 10^4$
Optical properties of tissue	Reduced scattering coefficient (μ_s')	$= 0.17\,mm^{-1}$
	Absorption coefficient (μ_a)	$= 0.005\,mm^{-1}$

Figure 4.2: Coordinate system and parameters used during the calculation.

With regard to the ultrasound, we assume that a transducer with a numerical aperture of 1 is placed at the same tissue surface. The generated ultrasound focal spot has transverse and longitudinal spot sizes of $15\,\mu$m and $30\,\mu$m, respectively, and we assume that the ultrasound is also pulsed with a frequency of $4\,$kHz . The ultrasound frequency is $50\,$MHz . Each ultrasound pulse ($20\,$ns long, corresponding to a single cycle) is assumed to modulate photons from each light pulse, as the light pulse is not broadened much at the dimension under consideration. Pressure at the target depth is set as $2.35\,$MPa corresponding to the safety standard (spatial-peak pulse-average intensity of $190\,$W cm^{-2}) [101,102]. The corresponding mechanical index value ($= 0.33$) and spatial-peak temporal-average intensity ($= 15\,$mW cm-2) is well below the safety standards (1.9 and $720\,$mW cm^{-2} for the respective standards). Figure 4.2 summarizes the parameters used in our analysis.

Assumptions

As previously mentioned, this study is primarily aimed at elucidating fundamental optical limitations in the TRUE focusing technique, rather than focusing on limitations associated with current technical hurdles. As such, we make idealized assumptions that exceed the currently available performances of sub-systems that make up the TRUE focusing system. This section details these assumptions and compares them with the current technical limit.

Assumption 1. The DOPC sensor and SLM have a sufficiently high number of pixels, and the pixels are sufficiently small to capture the nuances of all the backscattered light field. This assumption ensures that, in the absence of noise, our sensor and SLM are not limiting factors in characterizing the phase of all the optical modes (wave front) of the backscattered light field. In a fully developed speckle field, the total number of optical modes associated with light emerging from a $20\,$cm $\times$ $20\,$cm surface is given by $\sim 2.5 \times 10^{-11}$. This is $\sim$5 orders of magnitude greater than the number of pixels available on a high-end commercial sensor and SLM. We do note that there are no physical laws that prevent the scaling up of pixel counts in these digital components. In practical experiments, it may also be possible to manage the

way we select dominant optical modes [41] so that we can usefully devote the available system pixels to optimally collect signals.

Assumption 2. Each sensor pixel has an unlimited well depth and 100% quantum efficiency as well as zero dark noise and readout noise so that our wavefront measurement by interferometry is only subjected to shot noise. In practice, sensor sensitivity suffers from dark noise, readout noise, limited well depth, and quantum efficiency. However, as we are more interested in the fundamental penetration depth limit imposed from Poissonian shot noise at low signal level, this assumption allows us to explore TRUEs depth penetration capability without getting bogged down by the current capabilities of sensors.

Assumption 3. The scatterers are assumed to be static during $1\,\mathrm{ms}$ ($= t_{rec}$). In the absence of substantial blood flow, one early experiment indicates that photorefractive crystal-based OPC playback of the wavefront can adequately perform the time-reversal of multiply scattered light at a living tissue thickness of $\sim 7\,\mathrm{mm}$ with a decorrelation time-scale of one second (wavelength of $532\,\mathrm{nm}$, live rabbit ear [62]). Intrinsic cellular motions in a living sample can be expected to set the time-window for TRUE application in living targets. Blood pulsation and unintentional movement of living sample will induce additional bulk movement of scatterers that can deteriorate t_{dec} even further. Appropriate methods for holding the tissue robustly in place would likely be required as the proper physical fixing of tissue (the rabbit ear was gently held between two glass slides) is likely a major reason for why such a long decorrelation time was observed in [62]. The presence of moving blood within the blood vessels also constitutes a signal loss mechanism (light that passes through the blood vessel cannot be time-reversed) that results in a diminished PBR. Thus, we expect that, as long as blood pulsation is minimized and the surrounding tissues are not perturbed by blood flow, photon paths through those unperturbed tissues would still preserve their time-symmetry property.

Assumption 4. Incident probe light is only modulated at the US spot. Here, we assume both probe light and ultrasound are pulsed. Both theoretically and experimentally, we can only modulate a light component passing though the US spot by

triggering an ultrasound pulse with a proper delay (which corresponds to the light pulse travel time to the US spot) with respect to light pulse generation [45].

Assumption 5. The backscattered light field has a fully developed speckle pattern where the dimension of speckle granularity (autocorrelation area) is $(\lambda/2)^2$ [10]. This is a valid assumption for the large-depth TRUE focus we are presently considering. By this assumption, the transmission matrix components, which relate the field at US spot and the field at the tissue surface, can be represented mathematically by a complex random Gaussian matrix [13, 20].

Assumption 6. Calculation of phase map and its display takes negligible time compared to the wavefront recording time. Because we set our recording time at 1 ms, the exposure time is set to $0.25\,\text{ms}(= t_{rec}/4)$ for each interferogram. In a typical TRUE setup, the calculation of the phase map from four interferograms takes around 200 ms, which can be significantly shortened with a better computing unit. Moreover, the display device (liquid crystal-on-silicon) operates at 60 Hz ($\sim 15\,\text{ms}$). We note that there is no physical limitation that prevents TRUE systems from achieving much faster display times. In the event that liquid crystal technology imposes a reaction time that is difficult to tackle, it is possible to envision switching to a MEMS-based display device to circumvent the display reaction time problem.

4.2.2   Model Analysis Strategy
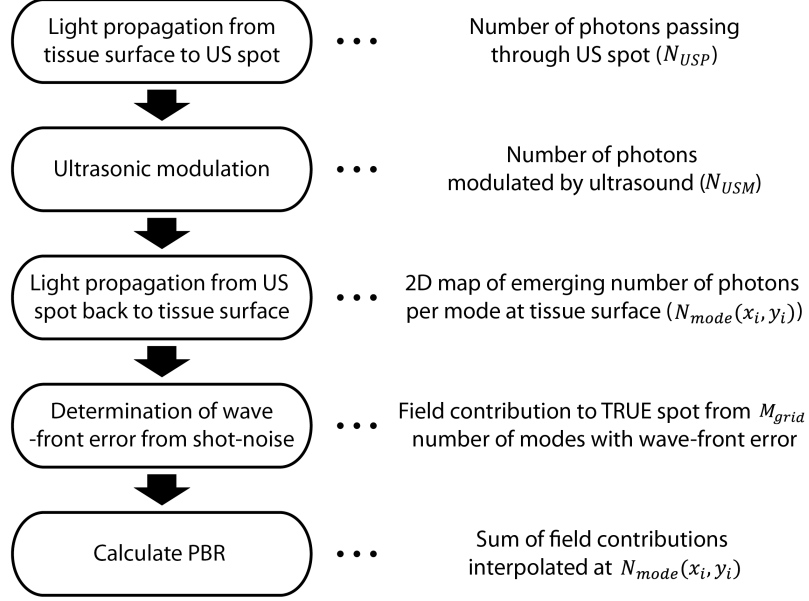
Figure 4.3: Flow chart of simulation procedure. 2D photon flux map emerging from the tissue surface is calculated from the first three steps regarding light propagation and ultrasonic light modulation. Then, wavefront measurement error resulting from shot-noise is determined to calculate the field contribution from M_{grid} number of modes to the TRUE focal spot ($A_{OPC\_LUT}e^{i\phi_{OPC\_LUT}}$). In the last step, PBR is calculated by summing up the field contributions from each simulation grid cell. Here, we use the lookup table approach that we will describe in detail at Section 4.2.2

The simulation consists of the following steps (Fig. 4.3): First, we simulate light propagation from the tissue surface (at the safety limit and within t_{rec}) to the deep-tissue US focus with diffusion approximation to calculate the number of photons passing through the ultrasound spot (N_{USP}). Second, the number of ultrasound-modulated photons (N_{USM}) is calculated by estimating the ultrasound-modulation efficiency with the Raman-Nath theory. Third, by propagating back the ultrasound-tagged photons emanating from the US focus, we mapped out the emerging tagged photon flux on the 2D tissue surface ($N_{mode}\left(x_{l,m}, y_{l,m}\right)$). Detection shot-noise is determined using the 2D photon flux. Finally, we determine the detailed relationship between shot-noise and focus contrast (peak-to-background ratio, PBR_{TRUE}) and determined the

practical depth limit of TRUE.

Simply put, PBR_{TRUE} is the ratio of fluence at the TRUE focal spot and the surrounding background. Despite the OPC beam's time-reversal property, background fluence is always expected to be present because the information of the tagged light emerging from US spot is partially lost due to light absorption during its propagation and partial measurement of the emerging wavefront (from one side of the tissue). Approximately speaking, it is proportional to the effective number of optical modes we can reliably measure for the backscattering light (reduced from the actual number of optical modes due to wave front measurement error) divided by the number of optical modes in the ultrasound spot (M_{US}).

Photon Budget Calculation

We used the diffusion approximation to calculate light propagation in scattering biological tissue. For simplicity, we used the light diffusion equation for a steady-state source, which is given by

$$\left(-D\nabla^2 + \mu_a\right) \Phi\left(\overrightarrow{r}\right) = q_0\left(\overrightarrow{r}\right), \tag{4.1}$$

where the diffusion constant D and source term $q_0\left(\overrightarrow{r}\right)$ are defined by

$$D = \frac{1}{3\left(\mu_a + \mu'_s\right)}, \text{ and } q_0\left(\overrightarrow{r}\right) = \int_{4\pi} \epsilon\left(\overrightarrow{r}, \hat{s}\right) d\Omega = 4\pi\epsilon\left(\overrightarrow{r}\right).$$

$\Phi\left(\overrightarrow{r}\right)$ is the fluence rate with units W/m^2, μ_a and μ'_s are the absorption and reduced scattering coefficients, respectively, and $\epsilon\left(\overrightarrow{r}, \hat{s}\right)$ is the amount of source power density generated along $\hat{s}$ at the small solid angle $d\Omega$ which is in units W/m^3. $\overrightarrow{r}$ is a position vector. The coordinate system used in this analysis is described in Fig. 4.1 and 4.2. Because the light pulse ($p_{dur} = 10\,\text{ns}$ long) is not significantly broadened, we simply use the source with the net power corresponding to the power of a single pulse ($= 20\,\text{mJ cm}^{-2} \times 5.1\,\text{cm}^2/10\,\text{ns}$) and integrate for a one pulse duration to get the photon fluence for each pulse. Equation (4.1) is derived from the radiative transfer

equation with the assumption that the light radiance can be expressed as an isotropic fluence plus a small directional flux [103]. The assumption is generally valid when the light propagation is scattering-dominated, and the position under consideration is far enough from the source ($> 1/\mu'_s$).

Then, the solution for steady-state Dirac-Delta source ($q_0(\overrightarrow{r}) = \delta^3(\overrightarrow{r})$) at the origin is simply

$$\Phi(\overrightarrow{r}) = \frac{1}{4\pi r D} e^{-\mu_{eff} r}, \tag{4.2}$$

where $\mu_{eff} = \sqrt{\mu_a/D}$ is the effective attenuation coefficient. To get the fluence for the collimated incident beam hitting the semi-infinite medium, we approximated the incident beam with $0.2\,\mathrm{mm}$-spaced point sources at the depth of transport mean free path ($1/\mu'_s$) where the photon loses its directionality (pencil beam approximation) [103]. We used a zero-boundary condition to take into account the effect of the boundary [104]. That is,

$$
\begin{aligned}
\Phi(\overrightarrow{r}) &= \Phi(x, y, z) \\
&= \sum_{i \in \text{point sources}} \frac{P_{point}}{4\pi \left|\overrightarrow{r} - (x_i, y_i, 1/\mu'_s)\right| D} e^{-\mu_{eff}\left|\overrightarrow{r} - (x_i, y_i, 1/\mu'_s)\right|} \\
&\quad - \frac{P_{point}}{4\pi \left|\overrightarrow{r} - (x_i, y_i, -1/\mu'_s)\right| D} e^{-\mu_{eff}\left|\overrightarrow{r} - (x_i, y_i, -1/\mu'_s)\right|},
\end{aligned}
\tag{4.3}
$$

where the P_{point} is the power of each point source, E_{point}/p_{dur}. E_{point} is the energy of each light pulse each point source is sampling ($20\,\mathrm{mJ\,cm^{-2}} \times (0.2\,\mathrm{mm})^2$). The fluence can be interpreted as the number rate of photons passing through a certain point, with units of photon number$/(mm^2 \cdot sec)$. Thus, we estimate the number of photons passing through the ultrasound spot (N_{USP}) per pulse by multiplying the fluence by the area of the ultrasound focal spot and pulse duration. That is,

$$N_{USP} = \Phi(\overrightarrow{r_{US}}) \times A_{US} \times p_{dur}/(hc/\lambda), \tag{4.4}$$

where $\overrightarrow{r_{US}} = (0, 0, d_{US})$ is a position vector of the US spot, d_{US} is the depth of the US spot, $A_{US} = \pi \lambda_{US}^2/2$ is the surface area of the US spot, and λ_{US} is the ultrasound

wave length. We assumed that the US spot is ellipsoidal with transverse and axial sizes of $\lambda_{US}/2$ and λ_{US}, respectively.

There are two main mechanisms of ultrasonic light modulation; the displacement of scatterers and the change in refractive index induced from the ultrasonic pressure [45]. The modulation contributed from the moving scatterers is negligible compared to that from ultrasound-driven index grating, because the number of scattering events is low due to the small US spot size. Thus, we modeled the ultrasound spot as the refractive index grating with the amplitude

$$\Delta n = \frac{\partial n}{\partial p} P, \tag{4.5}$$

where $\partial n/\partial p$ is a piezo-optic coefficient of the medium. We used the piezo-optic coefficient for water, $1.466 \times 10^{10}\,Pa^{-1}$ [105]. These parameters satisfy the following standard to use the Raman-Nath theory for nearly all incidence angles of light [106, 107]:

$$\frac{Q'(\theta)\,\gamma(\theta)}{2} \leq 1, \tag{4.6}$$

where the parameter $Q'(\theta)$ is $2\pi\lambda l/n_0\lambda_{US}\cos\theta$, $\gamma(\theta) = \pi\Delta n l/\lambda\cos\theta$ is the modulation parameter, and l is the light-sound interaction length. This condition is satisfied up to $88/,^\circ$ ($\equiv \theta_{max}$) with $\lambda_{US} = 30\,\mu m$. The effective light-ultrasound interaction length was estimated as $\lambda_{US}/2$ based on the NA ($=1$) of the ultrasound transducer. Then, from the Raman-Nath theory, the first-order diffraction efficiency is simply given by [106–108]

$$\eta(\theta) = J_1^2(\gamma(\theta)). \tag{4.7}$$

Then, the ultrasound-modulated photon number per pulse can be calculated as

$$N_{USM} = \left(N_{USP} \int_0^{\theta_{max}} \eta(\theta)\,d\theta \right) \Big/ \theta_{max} \tag{4.8}$$

because θ_{max} (incidence angle up to which the Raman-Nath theory is valid) is near 90° and irradiance is nearly isotropic in the diffusive regime.

As the last step of light propagation simulation, we calculate the propagation of the tagged photons to the tissue surface. We first assume the point source matches with the light power calculated from the previous step. As with the simulation of incident light propagation, diffusion approximation with a zero-boundary condition is used to calculate the flux (with units W/m^2) from the tissue surface, which is given by

$$
\begin{aligned}
\overrightarrow{J}\left(\overrightarrow{r}\right) &= -D\nabla\Phi\left(\overrightarrow{r}\right) \\
&= \frac{\Phi\left(\overrightarrow{r_{US}}\right)A_{US}\eta}{4\pi\left|\overrightarrow{r}-\overrightarrow{r_{US}}\right|^2}\left(\frac{1}{\overrightarrow{r}-\overrightarrow{r_{US}}}+\mu_{eff}\right)e^{-\mu_{eff}\left|\overrightarrow{r}-\overrightarrow{r_{US}}\right|}\left(\overrightarrow{r}-\overrightarrow{r_{US}}\right) \\
&\quad -\frac{\Phi\left(\overrightarrow{r_{US}}\right)A_{US}\eta}{4\pi\left|\overrightarrow{r}+\overrightarrow{r_{US}}\right|^2}\left(\frac{1}{\overrightarrow{r}+\overrightarrow{r_{US}}}+\mu_{eff}\right)e^{-\mu_{eff}\left|\overrightarrow{r}+\overrightarrow{r_{US}}\right|}\left(\overrightarrow{r}+\overrightarrow{r_{US}}\right),
\end{aligned}
\tag{4.9}
$$

where η is angle-averaged modulation efficiency ($= \int_0^{\theta_{max}}\eta\left(\theta\right)d\theta\Big/\theta_{max}$) [93,103]. The flux map was evaluated for every $0.1\,\mathrm{mm}$ over the $20\,\mathrm{cm}\times 20\,\mathrm{cm}$ area on which the OPC plane is assumed to be present. Because the speckle size is $\lambda/2$, the flux map is converted to the map of the average number of signal photons per mode (speckle) at each grid cell ($N_{mode}\left(x_{l,m},y_{l,m}\right)$) using the following relationship (l,m are indices for gird cells):

$$
N_{mode}\left(x_{l,m},y_{l,m}\right) = J_z\left(x_{l,m},y_{l,m}\right)\times\left(\lambda/2\right)^2\times p_{dur}\Big/\left(hc/\lambda\right),
\tag{4.10}
$$

where $J_z\left(x_{l,m},y_{l,m}\right)$ is flux along the z-axis. Then, by calculating wavefront measurement error induced from the shot noise at the signal level ($N_{mode}\left(x_{l,m},y_{l,m}\right)$), we estimated contrast (PBR) of the TRUE focal spot.

Phase measurement error calculation

Before estimating the theoretical PBR from the flux map, we first investigate the phase measurement error of the 4-step phase-shifting method while assuming only Poissonian shot noise. In the 4-step phase-shifting method [44], the intensity of each

interference is expressed by

$$
\begin{aligned}
I_i &= |E_{ref} + E_{sig} + E_{unmod}|^2 \\
&= A_{ref}^2 + A_{sig}^2 + A_{unmod}^2 + 2A_{ref}A_{sig}\cos\left(\phi_{ref_i} - \phi_{sig}\right) \\
&\quad + 2A_{ref}A_{unmod}\cos\left(\phi_{ref_i} - \phi_{unmod}\right) + 2A_{sig}A_{unmod}\cos\left(\phi_{sig} - \phi_{unmod}\right),
\end{aligned}
\tag{4.11}
$$

where $E_{ref} = A_{ref}e^{i\phi_{ref}}$ is a reference field (frequency-shifted), $E_{sig} = A_{sig}e^{i\phi_{sig}}$ is a signal field (frequency-shifted), $E_{unmod} = A_{unmod}e^{i\phi_{unmod}}$ is a unmodulated light field, and A and ϕ represent amplitude and phase, respectively. As only the fourth term on the right-hand side serves as signal term, the signal-to-noise (Poissonian shot noise) ratio (SNR) can be defined by

$$
SNR = \frac{2A_{ref}A_{sig}}{\sqrt{A_{ref}^2 + A_{sig}^2 + A_{unmod}^2 + 2A_{ref}A_{unmod} + 2A_{sig}A_{unmod}}} \frac{1}{hc/\lambda},
\tag{4.12}
$$

where h is Planck's constant. When the reference beam intensity is much larger than the others ($A_{ref}^2 \gg A_{sig}^2, A_{unmod}^2$), the SNR is maximized to $2A_{sig}/\sqrt{hc/\lambda}$ ($= 2\sqrt{\text{signal photon number}}$). We computed the phase from the four computationally generated interferograms with a large reference beam intensity and compared it with the actual phase. By repeating the procedure for many speckles, we could build the probability density function for the phase measurement error at different signal levels. For the creation of the interferogram, A_{sig} and ϕ_{sig} are randomly generated from Rayleigh distribution and uniform random distribution, respectively, based on the statistics of fully developed speckles. Then, the Poissonian shot noise with a standard deviation of $A_{ref}/\sqrt{hc/\lambda}$ ($= \sqrt{I_{ref}/(hc/\lambda)}$, generated with random number generator) is added to each interferogram. This exercise gives a better understanding of how the low signal intensity affects to the phase measurement error.

With this approach to determine wavefront measurement error, we calculated the field contribution from a single grid cell (M_{grid} number of modes) to the TRUE spot so that shotnoise-induced wavefront error was related with the reduction in OPC efficiency (reduction in effectively reliable number of optical modes). The PBR was

then evaluated by summing up the field contribution from each simulation grid cell. This calculation is based on the time-reversal symmetry of the scattering process, which is described in the following section.

PBR Calculation

Because scattering is a reciprocal process, we can expect scattering to possess time reversal symmetry. This property can be interpreted as follows:

A_0 (input mode) $\rightarrow A_k e^{i\phi_k}$ (k^{th} mode measured at OPC plane),

E_k (k^{th} mode played back at OPC plane) $\rightarrow \dfrac{A_k}{A_0} e^{i\phi_k} E_k$ (time-reversed input mode),

$$(4.13)$$

where A_0 is the incident signal light field on the input mode, $E_k = A_{ref} e^{-i\psi_k}$ is a phase-conjugated light field displayed at the OPC plane (SLM surface), A_k and ϕ_k are amplitude and phase of each speckle. ϕ_k and ψ_k can be thought as the actual and measured (played-back) phases of each speckle. Thus, if we perform OPC for the single input mode and there is no wavefront measurement error ($\psi_k = \phi_k$, when the signal intensity is high enough), the resultant field at the time-reversed input mode can be expressed by the following equation:

$$E_{OPC} = \sum_{k}^{M_{mode}} \frac{A_k e^{i\phi_k}}{A_0} E_k = \sum_{k}^{M_{mode}} \frac{A_k}{A_0} A_{ref}, \qquad (4.14)$$

where A_{ref} is the amplitude of the phase-conjugated light, and M_{mode} is the number of modes on OPC plane. Again, we assume that the OPC system only modulates phase. We also note that speckle amplitude (A_k) follows Rayleigh statistics by neglecting all the correlation between speckles (the transmission matrix component mentioned in the Assumptions section). By assuming plane wave illumination ($\psi_k = 0$), the field at the background is expressed by

$$E_{Back} = \sum_{k}^{M_{mode}} \frac{A_k e^{i\phi_k}}{A_0} A_{ref}. \qquad (4.15)$$

Then, by definition, PBR is [12, 42]

$$PBR_{single} = \frac{\sum\limits_{k}^{M_{mode}} E_{OPC}E_{OPC}^*}{\sum\limits_{k}^{M_{mode}} E_{Back}E_{Back}^*} \simeq \frac{\pi}{4}M_{mode}. \tag{4.16}$$

When wavefront error resulting from shot-noise is present, the intensity at the OPC spot is reduced to

$$E_{OPC}E_{OPC}^* = \left| \sum\limits_{k}^{M_{mode}} \frac{A_k e^{i\phi_k}}{A_0} A_{ref}e^{-i\psi_k} \right| \quad \text{with phase measurement error.} \tag{4.17}$$

Because of the huge number of optical modes (2.5×10^{11} speckles), we cannot use a simple Monte-Carlo approach (speckle by speckle). Instead, the contribution from M_{grid} number of modes on each simulation grid cell is pre-calculated for different average photon numbers, with the shot noise-induced wavefront error (grid cell by grid cell). This leads to a lookup table (LUT) relating the shot noise to the reduction in OPC efficiency. Then, we evaluate the field at the OPC spot by interpolating/extrapolating (from LUT) and summing up the field contribution ($A_{OPC\_LUT}(N_{mode}(x_{l,m}, y_{l,m})) \times e^{i\phi_{OPC\_LUT}(N_{mode}(x_{l,m},y_{l,m}))}$) from each simulation grid cell with the average signal photon number ($N_{mode}(x_{l,m}, y_{l,m})$). Mathematically, it is expressed as

$$\begin{aligned} E_{OPC} &= \sum\limits_{k}^{M_{mode}} \frac{A_k}{A_0}A_{ref}e^{(\phi_k - i\psi_k)} = \sum\limits_{l,m} \sum\limits_{k \in cell_{l,m}}^{M_{grid}} \frac{A_k}{A_0}A_{ref}e^{(\phi_k - i\psi_k)} \\ &= \sum\limits_{l,m} A_{OPC\_LUT}\left(N_{mode}\left(x_{l,m}, y_{l,m}\right)\right) e^{i\phi_{OPC\_LUT}\left(N_{mode}\left(x_{l,m},y_{l,m}\right)\right)}, \end{aligned} \tag{4.18}$$

where A_{OPC_LUT} and ϕ_{OPC_LUT} are the interpolation operators for amplitude and phase. The same approach has been used to calculate the background field assuming a plane phase map.

Equation (4.18) is for OPC procedure for single input mode. On the other hand,

in the case of TRUE focusing, the number of input modes can be estimated by

$$M_{US} = \frac{2A_{US}}{(\lambda/2)^2} \qquad (4.19)$$

where λ is the light wavelength. The factor of 2 is for considering modes propagating in either direction (with respect to the plane PBR is calculated on).

As the power of the OPC beam is distributed to the input modes, the PBR of the TRUE focal spot is given by

$$PBR_{TRUE} = \frac{\pi}{4} \frac{\sum_{k}^{M_{mode}} E_{OPC}E_{OPC}^* \Big/ \sum_{k}^{M_{mode}} E_{Back}E_{Back}^*}{M_{US}}. \qquad (4.20)$$

Both E_{OPC} and E_{Back} are calculated as the sum of contributions from grid cells (A_{OPC_LUT} and A_{Back_LUT}). The number of physical optical modes across the OPC plane ($20\,\text{cm} \times 20\,\text{cm}$) is 2.5×10^{11} and the number of input modes at the ultrasound plane is $\sim 1.8 \times 10^4$ for 800 nm. Thus, the ideal PBR_{TRUE} (without phase measurement error) is $\sim 1.4 \times 10^7$ for 800 nm, regardless of the depth. However, as derived above, PBR_{TRUE} decreases with depth due to the error in wavefront measurement.

We note that by this characterization, PBR_{TRUE} has a scaling relationship with the physical number of optical modes, and the signal level, which can be simply calculated with diffusion approximation. As such, while we have generally chosen optical and ultrasonic parameters to reflect a general TRUE scenario, the PBR_{TRUE} found here can be easily rescaled by a reader interested in a different set of parameters.

Definitions of TRUE Penetration Depth Limit

There are two ways we can define the penetration depth limits of TRUE from the simulation. Each is suitable for different applications. The primary way is to define TRUE depth limit ($depth_{local}$) as the depth at which PBR_{TRUE} decreases to the value of 2:

$$\text{1st standard: } PBR_{TRUE}(depth_{local}) = 2. \qquad (4.21)$$

This standard essentially can be used to test the effectiveness of the TRUE focusing technique because PBR_{TRUE} is itself the contrast of the TRUE focus.

The second way is to define TRUE depth limit (fluence depth) as the depth at which the photon fluence at the TRUE focus spot is at least higher than the incident light intensity at the sample's surface. The fluence at the TRUE focal spot can be simply calculated by

$$\Phi_{TRUE} = \Phi_{Back}\left(\overrightarrow{r_{US}}\right) \times PBR_{TRUE}, \qquad (4.22)$$

where $\Phi_{Back}\left(\overrightarrow{r_{US}}\right)$ is the background light fluence, which can be simply calculated by assuming plane wave illumination with the desired playback light intensity ($I_{playback}$). In short, $\Phi_{Back}\left(\overrightarrow{r_{US}}\right)$ can be thought of as background fluence. Therefore, the second standard:

$$\text{2nd standard: } \frac{\Phi_{TRUE}\left(depth_{local}\right)}{I_{playback}} = 1. \qquad (4.23)$$

The first definition is more generally useful and characterizable, as it simply tests for the presence or absence of TRUE-guided light at the aimed TRUE focus location. This is the definition we use predominantly. On the other hand, the second condition ensures that more light power is delivered to the point in the TRUE focal spot than the point on the tissue surface. So, for instance, it would be a useful standard for applications requiring an absolute optical power, such as "optical burning".

4.3 Results

The simulation results presented in this paper are aimed at predicting the key variables of TRUE focusing. Therefore the structure of the results section mirrors the physical TRUE focusing process.

For photon budget calculation, we note that all the plots are results from the 800nm light source, which leads to the largest penetration depth. First, Fig. 4.4(a) shows the photon fluence map of the incident probe light corresponding to a single pulse propagating through the tissue medium. Figure 4.4(b) shows the number of

photons passing through the US spot (N_{USP}). Because a very small portion of the diffused photons pass through the ultrasound spot, there is a significant loss in photon budget. For example, at a depth of ultrasound of 50 mm, only $\sim 1.1 \times 10^{11}$ photons pass through the ultrasound spot among the $\sim 2.1 \times 10^{18}$ number of incident photons for each pulse. Because, at 532 nm and 633 nm, the light source is more scattered and absorbed, a smaller portion of photons hit the ultrasound spot.

Then, the photons passing through the US spot are ultrasonically modulated by the efficiency depending on the incident angle of the light to the thin refractive index grating that is generated from the ultrasonic pressure (Fig. 4.5). We averaged the efficiency given by Raman-Nath theory up to θ_{max} ($= \int_{0}^{\theta_{max}} \eta\left(\theta\right) d\theta \Big/ \theta_{max}$). This results in a modulation efficiency of $\sim$0.0067. For 532 nm and 633 nm, the efficiencies are $\sim$0.013 and $\sim$0.010, respectively.
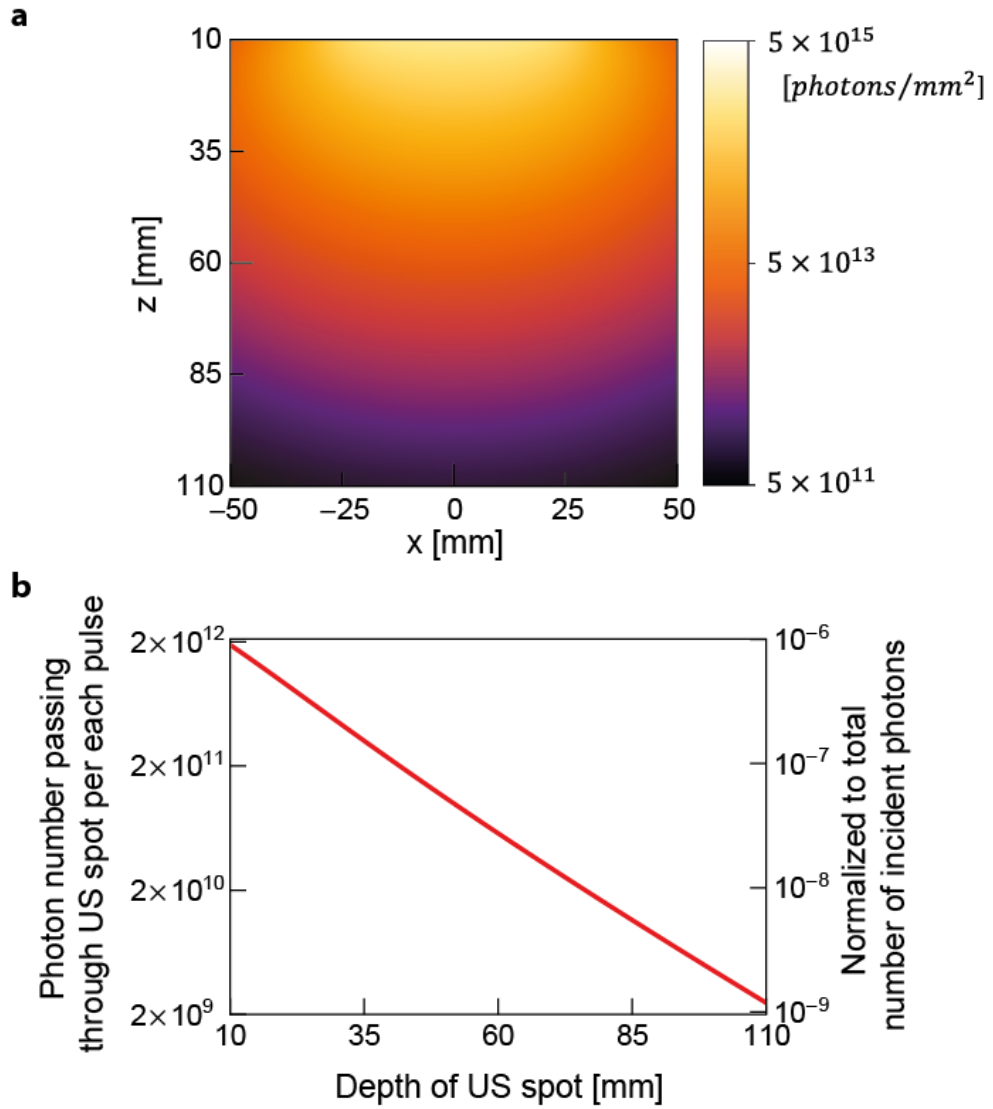
Figure 4.4: (a) Longitudinal sectional photon fluence map of the light beam propagating through the biological tissue corresponding to a single light pulse at the safety limit. The map is plotted in log scale. The wavelength is 800 nm. We calculated the number of photons passing through the US spot $(\Phi(\overrightarrow{r_{US}}) \times p_{dur}/(hc/\lambda))$ by multiplying the photon flux at target depth with the longitudinal cross-sectional area of the US spot. (b) Number of photons passing through the US spot is plotted along depth. The scale on the right axis represents the corresponding photon numbers normalized by the number of incident photons. The plot is in log scale.
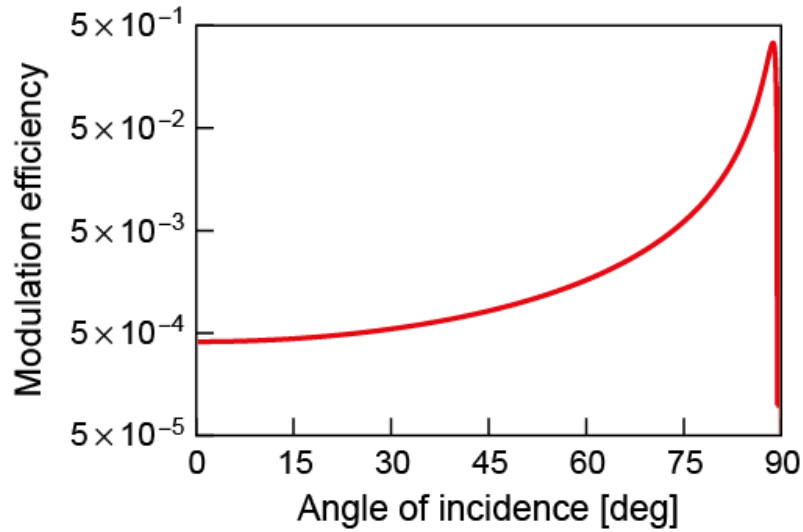
Figure 4.5: Dependence of ultrasonic modulation efficiency $(\eta(\theta))$ on the incident light angle as calculated by the Raman-Nath theory for an $800\,$nm light source and an ultrasonic pressure of $2.35\,$MPa. As $\theta_{max}(\sim 88\,°)$ is around $\sim 90\,°$ and the light irradiance is nearly isotropic in the diffusing regime, we averaged out the modulation efficiency for incidence angles of $[0, \theta_{max}]$. This results in a value of ~ 0.0067 (for $532\,$nm and $633\,$nm, ~ 0.013 and ~ 0.010, respectively). The number of modulated photon numbers (N_{USM}) is calculated by multiplying the averaged modulation efficiency with the number of photons passing through the US spot (N_{USP}). The plot is in log scale.

Following this, we propagate the modulated light back to the tissue surface. Figure 4.6(a) shows the average number of photons emerging from each speckle $(N_{mode}(x_{l,m}, y_{l,m}))$ for a single interferogram (corresponding to a single pulse) when the ultrasound spot is at a depth of $50\,$mm. We note that the photon number per speckle drops to much lower than 1, and will show that TRUE focusing can be achieved even with this photon budget. Figure 4.6(b) shows the total number of photons emerging from the surface. Because most back-scattered light falls into the region of the $20\,$cm $\times\,20\,$cm simulation grid, the photon budget loss is less significant than that in the first step. For example, for a depth of ultrasound of $50\,$mm, $\sim 5.7 \times 10^7$ photons emerge from the surface among $\sim 7.5 \times 10^8$ modulated photons at the US spot per pulse. Because of the same reason as in incident light propagation,

a smaller portion of photons can be detected with 532 nm and 633 nm.

a

b
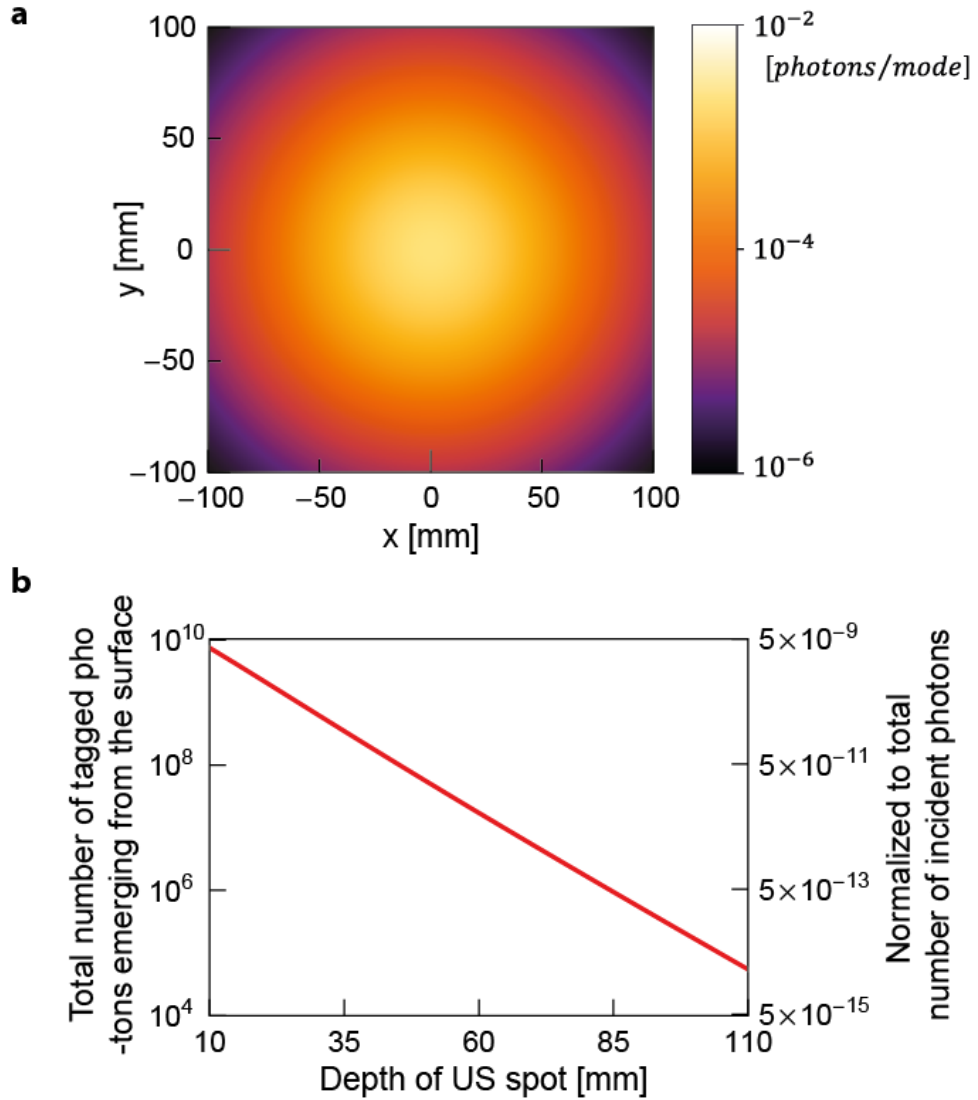
Figure 4.6: 2D photon flux map of ultrasonically modulated light emerging from the tissue surface from a single incident light pulse. The map is plotted in log scale. The target depth is 5 cm and the wavelength is 800 nm. We calculated the average number of photons per mode $(N_{mode}(x_{l,m}, y_{l,m}))$ by dividing the photon flux at each grid cell $(J(x_{l,m}, y_{l,m}))$ by the number of modes inside each grid cell (M_{grid}). (b) The total number of emerging photons at the surface is plotted for various depths. The scale on the right axis represents corresponding photon numbers normalized by the number of incident photons. The plot is in log scale.

Before evaluating the PBR from the photon flux map, we investigated the effect

of shot noise on the phase measurement error of individual optical modes at different average signal photon numbers ($I_{sig}/(hc/\lambda) = A_{sig}^2(hc/\lambda)$) (Fig. 4.7). We note that the SNR is $2A_{sig}/\sqrt{hc/\lambda}$ as derived in Section 4.2.2 with an assumption of large reference beam intensity ($A_{ref}^2 \gg A_{sig}^2, A_{unmod}^2$). The phase error distribution becomes uniform as the number of signal photons is decreased. However, the PDF shows the slight confinement around 0 even with a signal photon number of 0.01. This implies that the measured phase is more likely in the same direction as the correct phase in the complex plane. This tendency results in a partially constructive interference (of different optical modes at DOPC plane) at the OPC spot (TRUE focal spot) even in circumstances in which the emerging photon per speckle ($N_{mode}(x_{l,m}, y_{l,m})$) is much lower than 1.
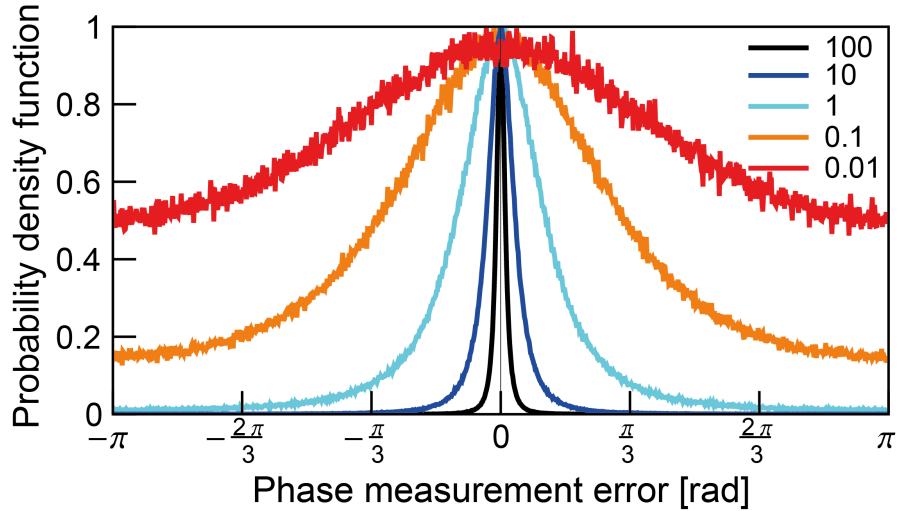
Figure 4.7: Normalized probability density function of the phase measurement error at different average signal levels ($I_{sig}/(hc/\lambda) = A_{sig}^2/(hc/\lambda)$) – 100, 10, 1, 0.1, 0.01 photon(s). The PDF is built with the Monte-Carlo simulation of a 4 step phase shifting method for 10^5 modes. The error is increased as the signal is decreased. Though it is wide, the peak around 0 is observed even at signal photon numbers smaller than 1.

Then, we build the relationship of PBR degradation with the wavefront measurement error. As mentioned above, we utilize the grid cell-wise field contribution (from the DOPC plane to the TRUE spot) which is prebuilt in LUT. More specifically,

the LUT relates the average signal photon number per mode ($N_{mode}(x_{l,m}, y_{l,m})$) to the field contributions A_{OPC_LUT} and ϕ_{OPC_LUT} (from a single simulation grid cell consisting of M_{grid} number of modes). Figure 4.8(a) shows the intensity contribution (square of amplitude, $A^2_{OPC\_LUT}$) from a single grid cell when phase conjugation is performed for the single input mode. The plot is normalized with the ideal intensity in the case without wavefront measurement error. The intensity contribution is not degraded significantly with more than 10 photons per mode (on average). However, shot noise at a low signal limit dramatically deteriorates the intensity contribution. For the sake of comparison with the background ($A^2_{Back\_LUT}$), Fig. 4.8(b) shows the PBR of the OPC spot optimizing a single input. PBR decreases to 1 at a low signal photon limit and saturates to the theoretically expected value, $\pi M_{grid}/4(= 4.8 \times 10^4)$, with sufficient photon budget to precisely characterize the wavefront. Insets present the resultant phase of the phase-conjugated field (ϕ_{OPC_LUT}) at different signal photon levels. As the PBR closes to 1 at the low photon budget limit, the resultant phase (ϕ_{OPC_LUT}) of the phase-conjugated field becomes uniform (Fig. 4.8(b) insets). In spite of the degradation, the PBR is still well above 1 even when the photon budget per speckle is, on average, only 10^4. From the LUTs, OPC and background field contributions (A_{OPC_LUT}, A_{Back_LUT}, and ϕ_{OPC_LUT}) from each grid cell is interpolated (at simulated signal photon number, $N_{mode}(x_{l,m}, y_{l,m})$). Then, by summing up and squaring the field contributions for OPC peak and background field, respectively, peak intensity (single mode) and background intensity is calculated. It gives the PBR_{single} (with phase measurement error). PBR_{TRUE} is simply PBR_{single}/M_{US}.
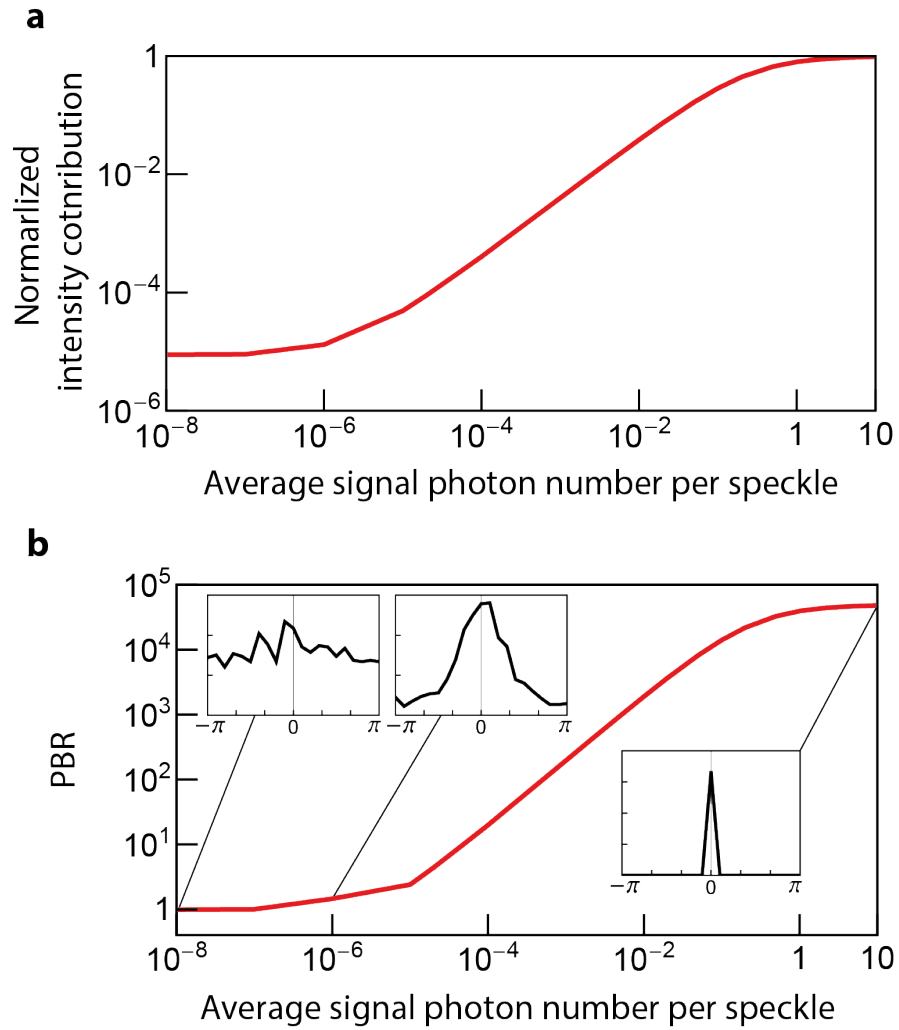
Figure 4.8: (a) Normalized intensity contribution from the single grid cell (0.1 mm × 0.1 mm) to a single input mode ($A^2_{OPC\_LUT}$) when OPC is performed for M_{grid} ($= 6.25 \times 10^4$) modes. The plot is normalized with the ideal intensity contribution in the case without wavefront measurement error. (b) Dependence of PBR on the average signal photon number when OPC is performed on a single grid cell for the single input mode. By assuming plane wave front, background intensity contribution is calculated. Then, PBR is calculated by dividing peak intensity contribution with the background intensity contribution. The insets show the resultant phase distribution (PDF) of the phase-conjugated field ($\phi_{OPC_{LUT}}$) at different signal photon levels.
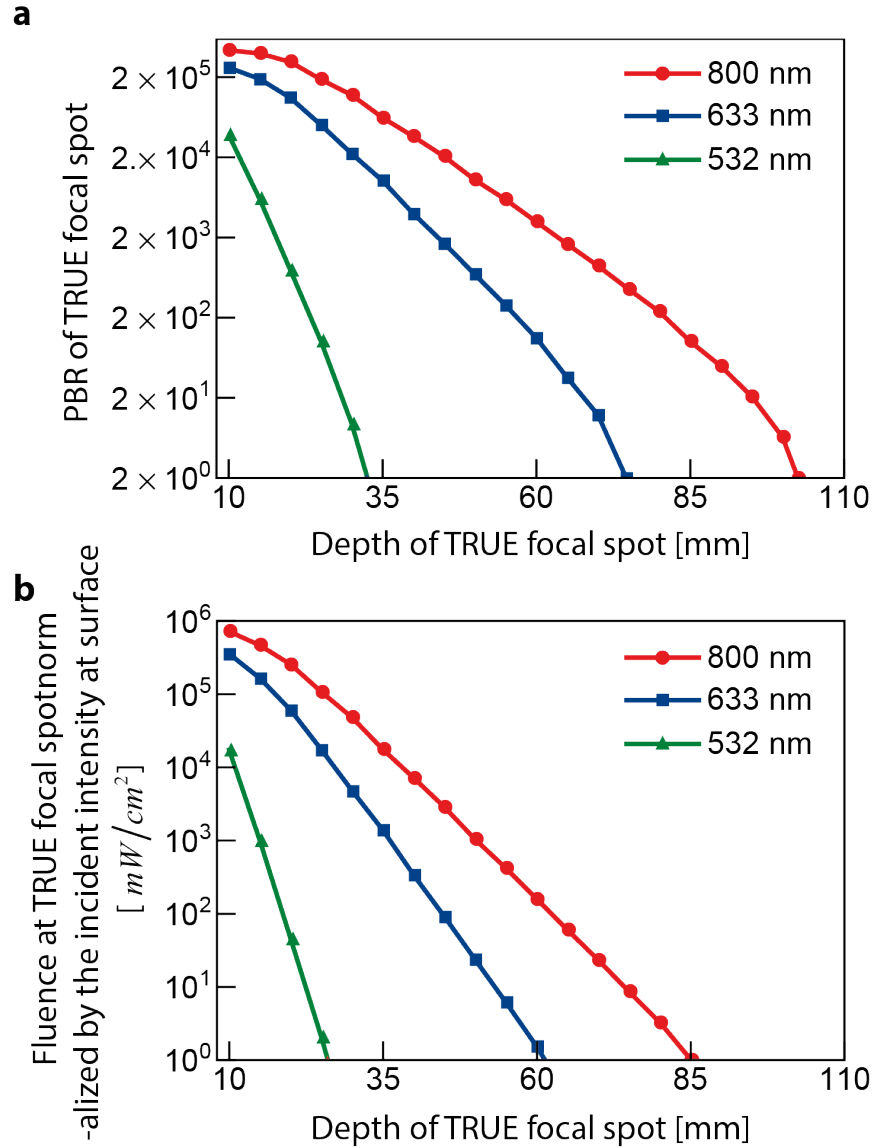
Figure 4.9: (a) Dependence of PBR of TRUE focal spot on the target depth. Penetration depth limit is $\sim 103\,\mathrm{mm}$ ($depth_{local}$ where $PBR_{TRUE} = 2$) with $800\,\mathrm{nm}$ (red line, circle marker). (b) Dependence of fluence at TRUE focal spot normalized by the incident playback light intensity at surface. Light power on the TRUE focal spot becomes weaker than the incident light power from $\sim 85\,\mathrm{mm}$ ($depth_{fluence}$) for $800\,\mathrm{nm}$. Penetration depth limits for both standards are reduced to $\sim 34\,\mathrm{mm}$ and $\sim 75\,\mathrm{mm}$ ($depth_{local}$), $\sim 25\,\mathrm{mm}$ and $\sim 62\,\mathrm{mm}$ ($fluence_{depth}$), for $532\,\mathrm{nm}$ (green line, triangle marker) and $633\,\mathrm{nm}$ (blue line, square marker) light, respectively.

Figure 4.9(a) shows the dependence of PBR_{TRUE} on the depth of the target spot.

The PBR nearly exponentially drops as the depth increases. We determined the two penetration depth limits ($dpeth_{local}$, $dpeth_{fluence}$), respectively. Based on the first standard ($PBR_{TRUE} \geq 2$), the TRUE focal spot can be created at up to $\sim 103\,\text{mm}$ ($depth_{local}$). For the 532 nm and 633 nm light sources, local depth is reduced to $\sim 34\,\text{mm}$ and $\sim 75\,\text{mm}$, respectively. For the second standard, Fig. 4.9(b) presents the fluence at the target spot (Φ_{TRUE}) normalized by the incident light intensity. Even though the TRUE focal spot can be created (peak contrast $PBR_{TRUE} \geq 2$), light (Φ_{TRUE}) is actually not more concentrated at TRUE focal spot compared to the incident light intensity of the phase-conjugated beam at the tissue surface for depths over $\sim 85\,\text{mm}$ ($depth_{fluence}$). The second condition for fluence depth is generally more restrictive than the first standard for local depth. The TRUE PBR is around 100 at fluence depth with the parameters under our consideration. $depth_{fluence}$ is decreased to $\sim 25\,\text{mm}$ and $\sim 62\,\text{mm}$ for 532 nm and 633 nm, respectively.

4.4   Summary and Outlook

In this study, we have developed a computational method to track the photon budget during the TRUE focusing process and investigate the fundamental limit in the penetration depth of the TRUE focusing technique.

As expected, the photon budget is decimated during light propagation from the tissue surface to the US spot, because the US spot is much smaller than the region covered by the diffuse light. We also found that an idealized OPC procedure can reconstruct the time-reversed focus even when the average photon number per mode is smaller than 1. At the low photon budget limit, the distribution of phase measurement error significantly spreads out to a large value. However, there still is a slight tendency for the error distribution to peak around 0. So, when the number of phase-conjugated modes is large, this subtle tendency results in the partially coherent addition of the OPC field from each optical mode on the DOPC plane.

We determined two penetration depth limits of TRUE focusing technique ($depth_{local}$, $depth_{fluence}$) from two separate standards: the PBR should be higher than 2, and

the photon fluence at the TRUE spot should be higher than the incident light intensity on the surface so that more light is actually delivered to the spot. For an 800 nm light source, a 50 MHz ultrasound frequency, and a 2.35 MPa ultrasonic pressure at the US spot, and with typical optical properties for chicken tissue (reduced scattering coefficient $\mu'_s = 0.17\,\mathrm{mm}^{-1}$, and absorption coefficient $\mu_a = 0.005\,\mathrm{mm}^{-1}$) the TRUE focusing technique can create focus up to $\sim 103\,\mathrm{mm}$ ($depth_{local}$). In terms of power delivery ($\Phi_{TRUE}(depth_{local}) = I_{playback}$ at the surface), the TRUE focusing technique is effective up to $\sim 85\,\mathrm{mm}$ ($depth_{fluence}$). As 532 nm and 633 nm light sources are more scattering and the light is absorbed through the biological tissue, the penetration depths are reduced to $\sim 34\,\mathrm{mm}$ and $\sim 75\,\mathrm{mm}$ ($depth_{local}$), and $\sim 25\,\mathrm{mm}$ and $\sim 62\,\mathrm{mm}$ ($depth_{fluence}$), respectively.

The result will vary depending on the parameters used in the numerical model. For instance, we performed the simulation for 10 MHz ultrasound frequency, as the ultrasound of 50MHz is expected to be attenuated dramatically ($0.54\,\mathrm{dB\,MHz}^{-1}\,\mathrm{cm}^{1}$ for soft tissue) [109]. First, more photons pass through the US spot as the spot becomes larger with lower frequency. Then, more photons can be collected during wavefront measurement, and this results in a higher number of reliable optical modes on the DOPC plane. Thus, even though the optimized power is distributed to a larger number of optical modes at the US spot (M_{mode}), the PBR_{TRUE} is enhanced. The depth limits are calculated as $\sim 139\,\mathrm{mm}$ and $\sim 100\,\mathrm{mm}$ for $depth_{local}$ and $depth_{fluence}$, respectively (an 800 nm light source is assumed). We can conduct further analyses on other parameters (light wavelength, incident light power, beam width of incident light, ultrasound pressure, physical size of the DOPC system) and it would be useful to find optimal parameters for different configurations. Moreover, it might be interesting to see how the penetration depth changes for different types of tissue.

Though we used the diffusion approximation with a zero-boundary condition for simplicity, a more accurate method to simulate light propagation simulation (such as a numerical solution of RTE, the Monte-Carlo method) can be used. It also would be worthwhile to develop our model to simulate a more realistic case with a practical design such as finite well depth and finite sensitivity of the sensor, and a large pixel

size for the DOPC system.

Chapter 5

Enhancing Resolution of Deep Tissue Light Focusing Method

The Time-Reversed Ultrasound-Encoded (TRUE) light focusing technique enables noninvasive focusing deep inside scattering media. However, the contrast and resolution of the spot is far from ideal as the structured wavefront optimizes the light field at the ultrasound focus, which is composed of thousands of optical modes, rather than a single optical mode inside deep tissue. In this chapter, we propose two methods to effectively reduce the number of optical modes composing the guide-star, resulting in improved contrast and resolution of the ultrasound-aided deep-tissue light focusing method.[1]

5.1   Iterative TRUE Optical Focusing Technique

In the TRUE light focusing technique, the time-reversal procedure usually has a low signal-to-noise ratio because the intensity of ultrasound-encoded light is intrinsically low. Consequently, the contrast and resolution of TRUE focus is far from ideal, es-

---

[1]The first section of this chapter is reproduced with some adaptations from the manuscript Ruan, H.*, Jang, M.*, Judkewitz, B. & Yang, C. Iterative time-reversed ultrasonically encoded light focusing in backscattering mode. Sci. Rep. 4, 7156 (2014). *: equal contributions. MJ contributed to developing the idea, designing and conducting the experiments, analyzing the experimental results, and preparing the manuscript. The second section of this chapter is reproduced with some adaptations from the manuscript Ruan, H.*, Jang, M.* & Yang, C. Optical focusing inside scattering media with time-reversed ultrasound microbubble encoded light. Nat. Commun. 6, 8968 (2015). *: equal contributions. MJ contributed to developing the idea, designing and conducting the experiments, analyzing the experimental results, and preparing the manuscript.

pecially in the backscattering geometry, which is more practical in many biomedical applications. To improve the light intensity and resolution of the TRUE focus, we developed an iterative TRUE (iTRUE) light focusing technique that employs the TRUE focus itself as a signal source (rather than diffused light) for subsequent TRUE procedures. Importantly, this iTRUE technique enables light focusing in backscattering configuration. We demonstrate the concept by focusing light in between scattering layers in a backscattering configuration and show that the light intensity at the focus is progressively enhanced by a factor of $\sim$20. By scanning across a fluorescent bead between these two scattering layers, the focusing resolution in the ultrasound axial and lateral directions was improved 2-fold and 3-fold, respectively. We further explore the application of iTRUE in biological samples by focusing light between 1-mm thick chicken tissue and cartilage, and observe the enhancement of light intensity in the same order.

5.1.1   Challenges in TRUE focusing technique

Focusing light inside scattering media such as biological tissues is attractive, especially in biomedical applications. However, this is a challenging task because optical scattering must be overcome. The iterative optimisation based technique [12] has been developed to focus light to an area of interest. This technique optimises the spatial light modulator by maximising the feedback signal. Transmission matrix measurement [13] is another technique that enables light focusing through scattering media. Instead of iteratively optimising a wavefront or measuring a transmission matrix, phase conjugation techniques directly obtain the required wavefront at high speed, using nonlinear media [19,26] or imaging sensor arrays via Digital Optical Phase Conjugation (DOPC) [42]. DOPC records the optical wavefront from the target and plays back the phase-conjugated light, which traces back to its origin due to time-reversal symmetry. However, all of these techniques require a guide star or sensors behind or inside the scattering medium. These guide stars could be direct light sources [77,86], photoacoustic based objects [110], optical nonlinear particles [111], or an ultrasound

focus [45, 93, 94, 112]. Among these sources, an ultrasound focus is the best fit for noninvasive operation because it creates a virtual source inside the scattering medium by modulating the frequency of the scattered light.

Time-reversed ultrasound-encoded light was first demonstrated using a photore-fractive crystal as a wavefront recording and modulating medium [93]. However, the crystal provided low optical gain and thus had limited potential for applications requiring focusing deep inside a highly scattering medium. Although nonlinear poly-mer films are able to enhance the optical gain [113], the gain is still much lower than that obtained by the DOPC method, which has a theoretically infinite optical gain that is practically limited by the damage threshold of the optics [42]. Using DOPC as a phase conjugation engine for TRUE, deep tissue fluorescence imaging has been demonstrated [45, 94]. Moreover, digital TRUE allows for manipulation of the mea-sured phase map and thus provides advantages such as resolution improvement [41].

One of the factors that limits the applications of the TRUE method is the low focusing peak intensity to the background intensity (with uncontrolled light illumina-tion) ratio (peak-to-background ratio; PBR) resulting from the low detected intensity of ultrasound modulated light. In deep tissue imaging applications, for example, only a small proportion of light will travel through the ultrasound focus, which is very tight (typically, $100\,\mu$m), to obtain a high resolution image. Of the light that is in the focus, only a small proportion will be modulated by ultrasound with an intensity at diagnostic ultrasound levels [114]. Therefore, it is challenging to measure an accu-rate phase map of the ultrasound modulated light because of the low signal-to-noise ratio (SNR). The low SNR limits the applications of TRUE, such as focusing in the backscattering mode that is more practical in biological applications. Although ana-logue TRUE in reflection mode has been demonstrated [115], it also has the problem of low optical gain.

An intuitive approach to solve the low ultrasound modulation efficiency in TRUE would be using the TRUE technique itself because it can deliver stronger light at the focus of the ultrasound. This method would in return result in a more accurate phase map and, consequently, higher light intensity at the ultrasound focus. By iter-

ating this process, the light intensity at the ultrasound focus would be significantly enhanced. Technically, this requires DOPC to simultaneously record the ultrasound modulated light and play back its amplified phase-conjugated copy. A dual-DOPC-based TRUE setup was proposed for this purpose [95], but the system was redundant and was difficult to fit in the backscattering mode, which is critical in many applications such as biomedical imaging. Very recently, a continuous scanning-based TRUE scheme was demonstrated to be able to enhance light intensity with a single DOPC-based setup [116]. This work focused on a novel scanning scheme but did not demonstrate or quantify the light intensity enhancement and resolution improvement capabilities in backscattering mode.

The subsequent sections present an iterative time-reversed ultrasound-encoded (iTRUE) light focusing technique that can be used to focus light in backscattering mode. We observed a significant enhancement of the light intensity at the ultrasound focus and resolution improvement in images obtained using this technique. It should be noted that the terms iterative/iteration here refer to the repeating of the ultrasound modulation and phase conjugation process and should not be confused with that used for searching for an optimised wavefront based on feedback signals.

The subsequent sections are structured as follows. The next section describes the detailed principle of iTRUE light focusing technique, including the simulation result on SNR of the ultrasound modulated light. We will then present the experimental result of direct visualization of the reconstructed optical focus and imaging of fluorescent beads. Finally, we further demonstrate the advantage of the backscattering mode operation by focusing light between biological tissue and cartilage.

5.1.2 Principle
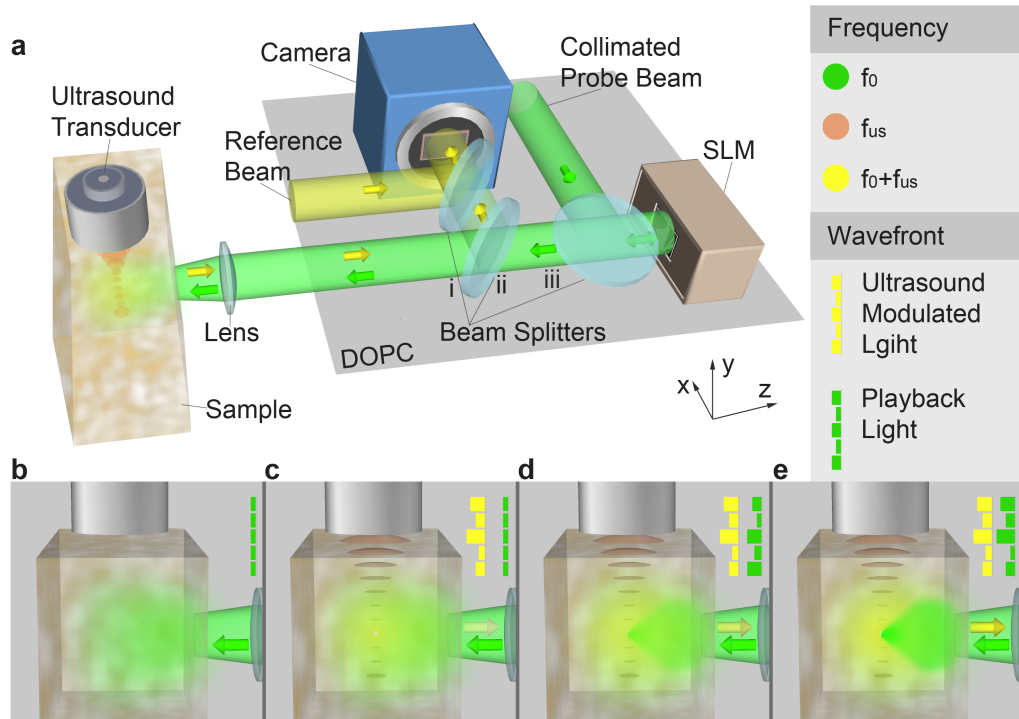
Figure 5.1: Principle of iTRUE. (a) Experimental setup. The probe beam reflected off the SLM is scattered by the sample and modulated by the ultrasound. The phase map of the ultrasound modulated light is measured by the camera. The conjugated phase map is displayed on the SLM, which modulates the probe beam again. (b)–(e) Schematic demonstration of signal enhancement with iTRUE. (b) Without ultrasound modulation, the probe beam diffuses inside the scattering sample when the SLM is initially uncontrolled. (c) With ultrasound modulation, a small fraction of the probe beam is shifted in frequency and back-scattered to the DOPC system. (d) The phase-conjugated copy of the measured ultrasound-modulated light is sent back to the sample. The playback light creates a focus at the focus of the ultrasound. This playback light focus is modulated simultaneously by the ultrasound, and a more accurate wavefront can be measured for the next step. (e) By repeating the playback and recording process, the light intensity focused at the focus of the ultrasound can be progressively increased.

The working principle of iTRUE is shown in Fig. 5.1. The setup consists of a DOPC module and an ultrasound modulation module (Fig. 5.1a). A collimated laser beam (frequency f_0) is launched to the phase-only SLM with an arbitrary or blank (Fig.

5.1b wavefront) phase display. The reflected light, serving as a probe beam, enters the scattering sample and diffuses, as shown in Fig. 1b. As the first step of TRUE (recording), ultrasound modulates the probe beam by shifting its frequency by the ultrasound frequency f_{US} (Fig. 5.1c). The backscattered ultrasound-modulated light as well as the unmodulated portion travel back to the beam splitter (ii) and then to the camera. In order to selectively measure the phase of the ultrasound-modulated light (Fig. 5.1c wavefront), a reference beam with a frequency tuned to $f_0 + f_{US}$ is used to interfere with the backscattered light, resulting in a static fringe pattern for the modulated light, while the unmodulated portion does not interfere coherently. In this case, a 4-phase stepping method [44] or off-axis holography can be used to record the phase map of the ultrasound-modulated light. In the second step (playback), the recorded wavefront is phase-conjugated (Fig. 5.1d wavefront) and sent to the SLM. The collimated probe beam is then modulated by the SLM and creates a focus at the ultrasound focus due to the time-reversal symmetry (Fig. 5.1d). The first step is then repeated, but this time stronger ultrasound-modulated light is generated (Fig. 5.1d) due to the results of the previous step. This procedure leads to a more accurate phase map (Fig. 5.1e wavefront) and, consequently, higher playback light intensity at the focus (Fig. 5.1e). As can be seen from the iTRUE setup, the iTRUE process requires that playback of the phase-conjugated light and the next recording of the wavefront occur simultaneously.

To better understand the steps of the iTRUE process, we carried out a simulation. In this simulation, the performance of the system in terms of noise was shot-noise limited. We assumed the average number of ultrasound-modulated photons per pixel is 10^{-2} and that of the unmodulated photons is 100. The average number of photons of the reference beam was 10^4, which is ~100 times higher than the signals (modulated and unmodulated light). These assumptions are based on estimations from a typical hologram captured in our TRUE system. In this simulation, only the shot noise from the reference beam was considered because the reference beam intensity is much higher than the intensity of the modulated and unmodulated photons. Therefore, shot noise from the unmodulated light could be neglected in the simulation. The

interference between the modulated light and the reference beam is given by

$$I_i = I_0 + I_{US} + 2\sqrt{I_0 I_{US}} \cos{(\phi_0 + \phi_{us})}, \tag{5.1}$$

where I_0 and I_{US} are the reference beam intensity and the modulated light intensity, respectively, in the units of photons; ϕ_0 and ϕ_{us} are the corresponding phases. The SNR of this interferogram can then be defined as [114]

$$SNR = \frac{2\sqrt{I_0 I_{US}}}{\sqrt{I_0 + I_{US}}} \simeq 2\sqrt{I_{US}}. \tag{5.2}$$

Plugging in the number of ultrasound modulated photons, we have $SNR \simeq 0.2$.
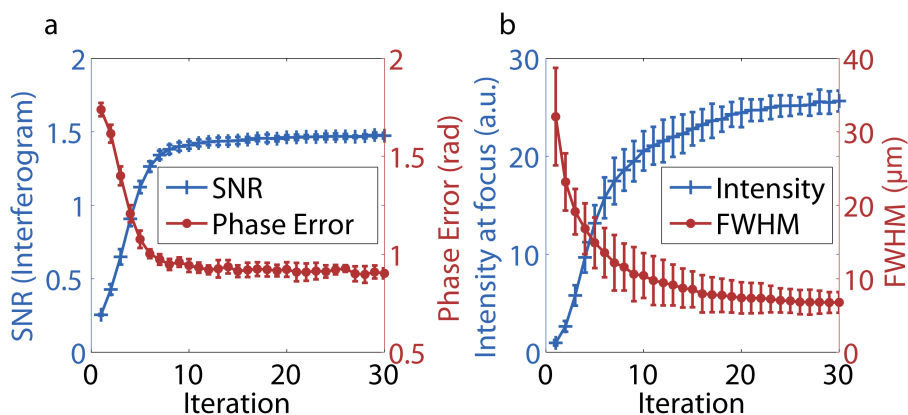
Figure 5.2: Simulation results of the iTRUE process. (a) SNR of the interferogram and the phase error (mean absolute) at the imaging sensor plane over the sequence of iterations. (b) Intensity enhancement and resolution improvement at the focus of the ultrasound over the sequence of iterations.

Although the SNR is very low at the beginning of the iTRUE iterations, light focusing at the focus of ultrasound can still be obtained because DOPC has a high tolerance for phase error. The playback focus then contributes to a higher modulated light intensity while the shot noise level is maintained, thus yielding a higher SNR measurement and a more accurate phase map, which in return creates a stronger focus at the ultrasound focus. Repeating this process in the simulation gave an iterative increase of SNR and a reduction in the phase error (Fig. 5.2a). As a result, a progressively enhanced light focus over the number of iterations was obtained (Fig.

5.2b). By fitting a Gaussian function to the scattered field in the virtual ultrasound focus, the full width at half maximum (FWHM) of the light focus was obtained during each iteration (Fig. 5.2b). A reduction of FWHM was observed during iteration because a Gaussian ultrasound profile was defined in this simulation. In this case, the multiplication of the profile during each iteration results in a narrower width. The error bars shown in Fig. 5.2 were calculated based on the standard deviation of 10 simulations.

5.1.3 Results

Direct Visualisation of the Optical Focus
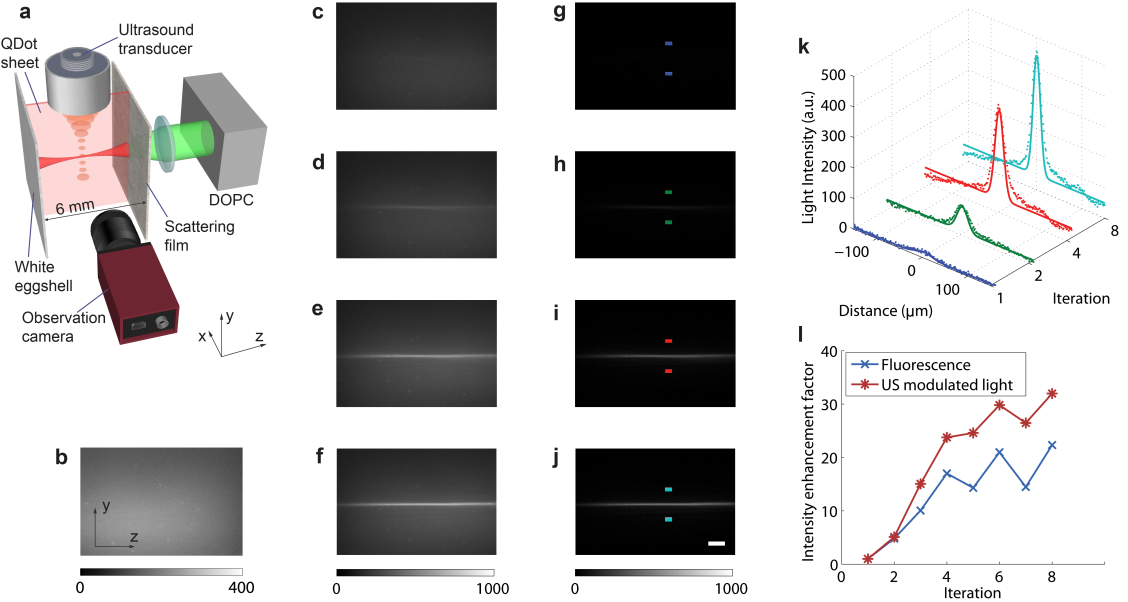
Figure 5.3: Demonstration of intensity enhancement using iTRUE. (a) A 500 mm thick quantum dot sheet made of agarose was sandwiched between a layer of scattering film and a piece of white eggshell. The probe beam of the DOPC system entered the sample via the film side. An observation camera with a fluorescence filter was used to observe the cutaway view of the emission light from the quantum dot sheet. This camera imaged at the focus of the ultrasound, which was located in the centre of the quantum dot sheet. (b) The emission light without TRUE (the SLM was loaded with a random pattern). (c–f) Emission beam profiles with iTRUE iterations of 1, 2, 4 and 8 times, respectively. (g–j) Light beam profiles with background subtraction. (k) One-dimensional images and the corresponding Gaussian fitting curves at the focus of the ultrasound (the area between the colour blocks of g–j). (l) The light intensity enhancement factor, measured based on the fluorescence intensity observed by the observation camera and the ultrasound-modulated light measured by the DOPC system. The scale bar is 200 μm.

In order to demonstrate intensity enhancement with iTRUE, we used a quantum dot sheet to visualise the focusing profile of the phase conjugated light between two scattering media. The design of the sample is shown in Fig. 5.3a. A quantum dot

sheet with a thickness of $500\,\mu$m was embedded in a block of clear agarose gel. The gel was placed between two scattering media, with a layer of scattering film on the front and a piece of white eggshell on the back. The distance between the two scattering media was $\sim 6\,$mm. A camera (Stingray F145, Allied vision technologies, Germany) with its imaging plane at the focus of the ultrasound transducer was used to image the light emission light profile from the quantum dot sheet. Without TRUE, the probe beam was scattered by the scattering film and the eggshell, resulting in a diffused background (Fig. 5.3b). By implementing TRUE, a weak light focus can be observed, as shown in Fig. 5.3c. The light focus here was much weaker than what has been demonstrated in transmission mode because the detected ultrasound-modulated light in backscattering mode is much weaker. By implementing iTRUE, significant light intensity enhancement was observed on the fluorescent quantum dot sheet, as shown in Fig. 5.3d-f, in which 2, 4 and 8 iterations were performed, respectively. To further enhance the contrast of the light foci, background subtraction was implemented for each image of the light focus. In this case, the background for each image was measured when the conjugated phase map on the SLM was shifted by 50×50 pixels during each iteration. Corresponding images with background subtraction are shown in Fig. 5.3g-j.

To quantify the intensity enhancement with iTRUE, we analysed the emission light intensity at the ultrasound focal zone. In this case, an area of interest with 200 pixels ($323\,\mu$m) in the y direction and 50 pixels ($81\,\mu$m) in the z direction was applied to the area, as shown in between the colour blocks of Fig. 5.3g-j. One-dimensional images were then taken by averaging these areas of interest in the z direction, as shown in Fig. 5.3k, in which significant light intensity enhancement can be observed. A Gaussian profile was fitted to each of these one-dimensional images, as shown in Fig. 5.3k. Taking the peak of each fitted Gaussian profile for the one-dimensional images from the first 8 iTRUE iterations, the intensity enhancement factor (the ratio between the peak intensity at each iteration to that at the first TRUE light focus) was quantified (Fig. 5.3l). For comparison, the intensity enhancement factor calculated based on the ultrasound-modulated light intensity detected by the DOPC system

using digital holography is also shown in Fig. 5.3l. The intensity enhancement factor at the ultrasound focus after 8 iterations was $\sim$22 based on the fluorescent signals and $\sim$32 based on the holography measurement.

Theoretically, the light intensity enhancement factor measured based on fluorescent signals and holography should be identical. However, the difference in the light intensity enhancement factors can be observed in Fig. 5.3l. One of the possible reasons for the inaccuracy could be the low light intensity at the first TRUE light focus compared with the considerable background. The other possible reason could be the nonlinearity of the two approaches. Light intensity oscillation can also be observed in Fig. 5.3l. One explanation for this oscillation is that the size of the ultrasound focus is much larger than that of an optical speckle. In this case, two sets of optical modes can oscillate during the iTRUE process. Another possible reason is that light travels through different channels of the scattering sample before and after ultrasound modulation during one iteration. To reduce this effect, one solution would be to combine the measured phase map with the previous measured phase maps for iTRUE playback at each iteration, rather than complete replacement of the phase map. However, the intensity optimisation process would be slower in this case.

Image Scanning
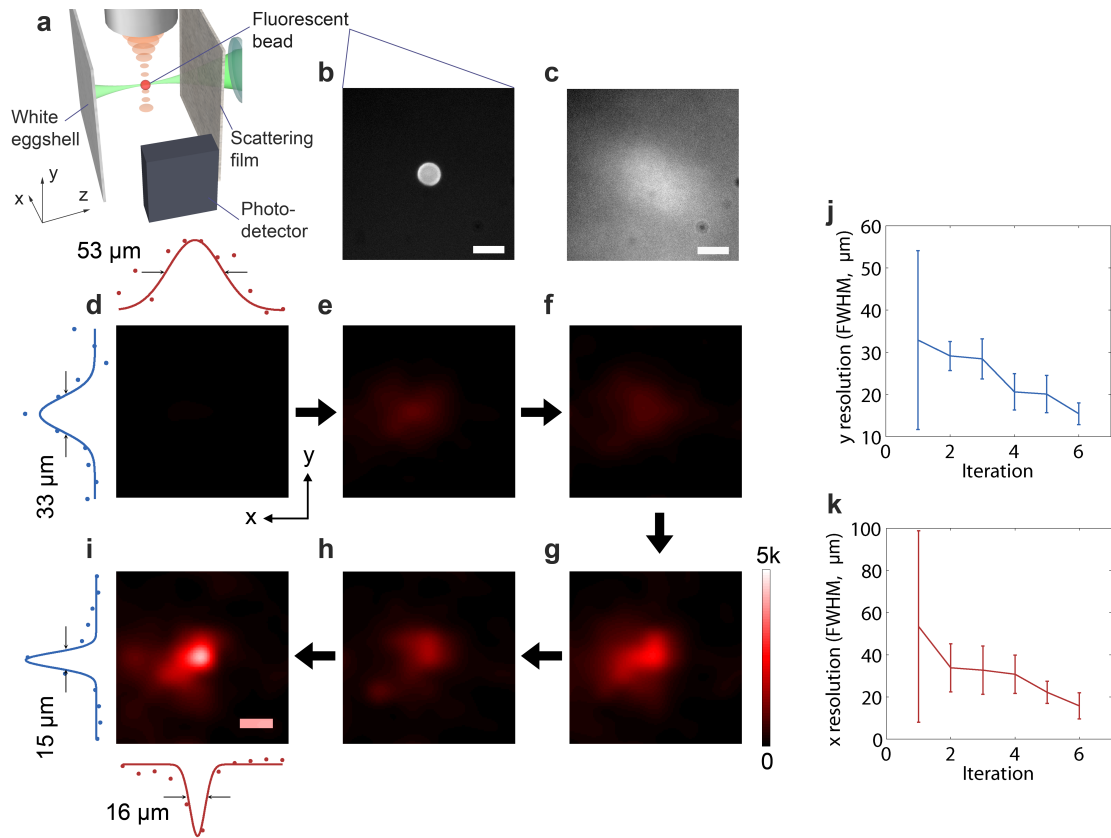
Figure 5.4: Image scanning of a fluorescent bead. (a) Experimental setup. The ultrasound focus scanned the sample in the x-y plane. At each step, 6 iTRUE iterations were implemented. The fluorescence intensity was measured at each iteration using the photodetector. (bc) Microscopic images of the fluorescent bead without and with the scattering film. (di) Intensity map of the fluorescent signals (11311 scanning points with cubic interpolation). A Gaussian profile was fitted to the data points across the centre of the bead in both the x and y directions. (j, k) The resolution (FWHM of the Gaussian profile) in the y direction and the x direction of the fluorescent bead image over 6 iterations. The error bars indicate the 95% confidence bound. All scale bars are $20\,\mu$m.

To quantify the resolution improvement using our iTRUE system, we imaged a $15\,\mu$m fluorescent bead by raster scanning. The experimental setup was the same as that used for direct visualisation of the focal beam, except that the quantum dot sheet

was replaced with a fluorescent bead and the observation camera was used as a single channel photodetector (Fig. 5.4a). Microscopic images of the fluorescent bead on a microscope slide without and with the scattering film are shown in Fig. 5.4b and c. It should be noted that the image shown in Fig. 5.4c was taken with scattering film attached to a piece of conventional microscope cover glass that covered the fluorescent bead. In the sample, the bead was placed 3 mm behind the scattering film. In order to scan the iTRUE focus across the fluorescent bead, the ultrasound transducer was moved in the x-y plane with a $10\,\mu$m step size and 11 steps in each direction ($110\,\mu$m $\times$ $110\,\mu$m in total). At each step, 6 iterations were carried out. In order to compare the performance of conventional TRUE and iTRUE with different numbers of iterations, the SLM was loaded with a random pattern at the beginning of each scanning step. The fluorescent intensity was measured when the random pattern was displayed on the SLM (background) and during each iteration. Background subtraction and cubic interpolation were applied to each intensity map. Fig. 5.4d-i show the scanned fluorescence images from the 1st iteration (conventional TRUE) to the 6th iteration with a global colour map. The image resolution in the ultrasound axial direction (y) and the lateral direction (x) were quantified by a fitting Gaussian profile to the one-dimensional bead images in both directions, as shown in Fig. 5.4d and i. The FWHMs of these Gaussian profiles were used to define the image resolution here. The axial and lateral resolutions of the fluorescent bead images are shown in Fig. 5.4j and k, respectively. It can be observed that the axial resolution and lateral resolution were improved by $\sim$2 times and $\sim$3 times, respectively. The error bars shown in Fig. 5.4j and k indicate the 95% confidence bound of the curve fitting. Large error bars were observed at the first iteration because the light intensity was too low to provide a small fitting error.

Light Focusing between Biological Samples
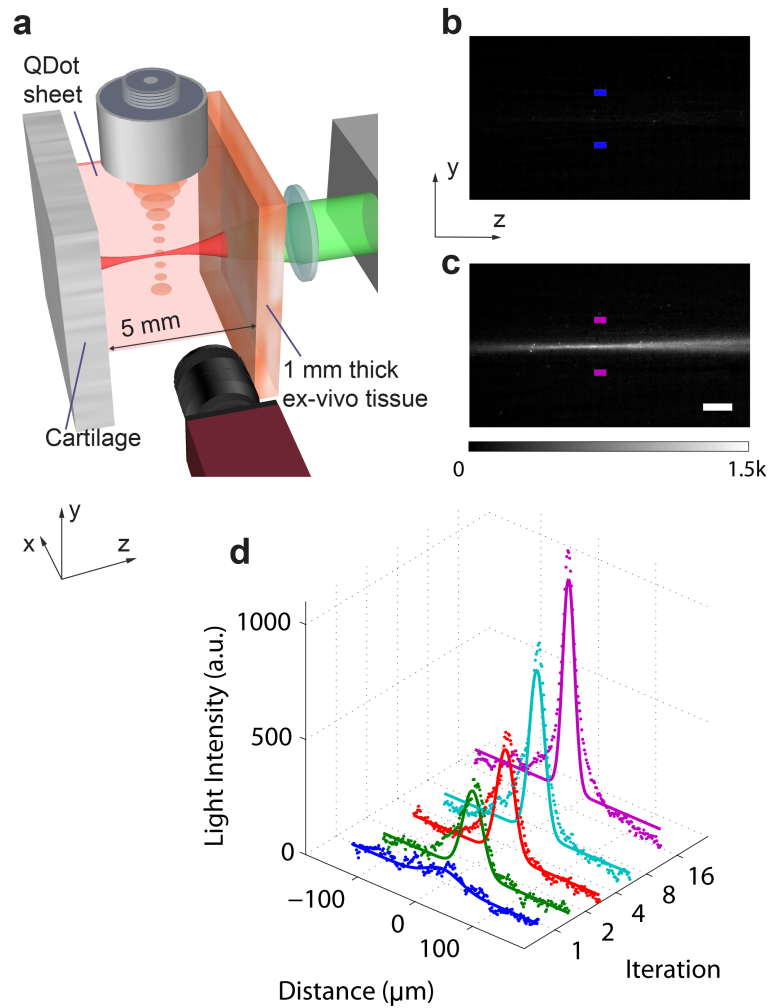
Figure 5.5: Observation of light intensity enhancement in biological samples. (a) Sample setup. The sample consisted of a piece of chicken tissue (1 mm thick) and cartilage, with a quantum dot sheet sandwiched between them for visualisation purpose. (bc) Image observed by the camera after the 1st iteration (b) and the 16th iteration (c) of iTRUE. (d) One dimensional images of the light foci after the 1st, 2nd, 4th, 8th and 16th iterations. These images were taken from the corresponding area between the two colour coded blocks shown in (b) and (c) (only the 1st and 16th images are shown). The scale bar is 200 μm.

Focusing light in tissue in backscattering mode has a great potential in biological applications, where thick tissue or highly backscattering tissues like bone or are involved. Here, we investigated the light focusing capability of iTRUE in biological

samples consisting of muscle tissue and cartilage. In order to directly visualise the focusing beam profile, a quantum dot sheet was also sandwiched between chicken muscle tissue (1 mm thick) and cartilage (Fig. 5.5a). By implementing iTRUE, the light intensity at the ultrasound focus increased progressively. The observation camera imaged the focusing beam profiles, as shown in Fig. 5.5b and c, in which images after the 1st iteration and the 16th iteration are compared. In order to measure the light intensity at the foci quantitatively, one dimensional images across the foci were taken using the same method as that used for Fig. 5.3k. It should be noted that two dimensional images at the 2nd, 4th and 8th iterations are not shown here. Gaussian functions were also fitted to these one dimensional images (Fig. 5.5d). By taking the ratio between the Gaussian profile amplitude of the 16th iteration and the 1st iteration, an intensity enhancement factor of 18 was achieved. The light intensity was saturated after $\sim$12 iterations, which is more than those required in the previous case with the scattering film and eggshell sample ($\sim$8 iterations). One reason for this difference is that the chicken muscle tissue scatters more light than the scattering film. Therefore, the initial ultrasound-encoded light intensity is lower and more iterations are required before saturation.

5.1.4 Summary and Outlook

The TRUE technique provides a non-invasive approach to focus light inside scattering media such as biological samples. This technique can be applied to a wide variety of applications such as deep tissue fluorescence imaging, photodynamic therapy, laser surgery and optogenetics. Some of the key factors making TRUE practical for these applications are its high focusing efficiency, higher resolution and the capability for backscattering mode operation. The proposed iTRUE technique provides an elegant solution for signal enhancement, resolution improvement and backscattering mode operation. The tissue-cartilage sample used in the experiment here mimics the structure that can be found in many parts of biological bodies. This is a significant step to move TRUE toward biological laboratories and clinics.

We explained the intensity enhancement mainly in terms of SNR throughout the Principle section. However, there could be other mechanisms that also contribute to the intensity enhancement. One potential mechanism is the reduction of the optical mode at the ultrasound focus, because iTRUE reduces the size of the optical focus. In this case, the ratio between the number of controllable optical modes and the number of optical modes contained in the ultrasound focus increases [12, 45]. The intensity of the background light also increases over iterations (Fig. 5.3c-f). This effect could be attributed to the possibility that the light intensity tends to be redistributed on the transmission channels with a higher transmission coefficient during the iteration process [83]. The maximum achievable PBR with iTRUE is limited by the noise present on the measured phase map, the size of the ultrasound focus and the number of controllable optical modes. In practice, the PBR of iTRUE is also limited by the achievable PBR of the DOPC system and the profile of the ultrasound focus.

Resolution improvement with iTRUE has been demonstrated experimentally and theoretically. The resolution can be improved because the profile of the ultrasound focus can be approximated to be Gaussian. The photons tend to focus back to the strongest modulated optical mode, which gives the highest modulated signals. In practice, the ultrasound profile is very flat compared to the size of an optical speckle. Therefore, the resolution improvement is limited. The resolution was improved less in the experiment than in the simulation, possibly because of the timing jitter between the ultrasound and laser pulses in our experiment.

Although only the backscattering mode is demonstrated here, we expect it would not be difficult to implement the iTRUE system in transmission mode. One simple solution would be to place a mirror on the other side of the sample when the transmission mode is needed. In transmission mode, the sample is usually thin and most of the light is forward scattered. In this case, the mirror would effectively reflect the forward scattered light back to the camera. This approach is similar to the case of folding one of the DOPC setups along the mirror plane in a 2-DOPC TRUE system [95], but the key difference is the capability of simultaneous playback and recording in a single DOPC system.

Currently, the operation time of TRUE (for a single iteration of wavefront measurement and playback) is approximately 1 s. This limits its biomedical applications to ex-vivo tissue samples or immobilised living tissue due to optical speckle decorrelation [62]. The overall implementation time of iTRUE increases by a factor of the iteration number. However, iterations will not make the decorrelation problem worse than it is for the TRUE case because iTRUE updates the phase map during each iteration. The decorrelation problem is only limited by the duration of a single iTRUE iteration, which is the same as that of TRUE. Therefore, similar to TRUE, the timing issue can be further improved by reducing the averaging frames for the phase recording using an off-axis holography for phase measurement and a faster SLM. For biomedical imaging, the overall scanning speed of the current iTRUE technique limits its application to a low number of sampling points. However, the overall image scanning speed of iTRUE can be further improved by using a continuous scanning scheme [116]. Importantly, focusing light inside biological tissue is also useful for other applications, such as photodynamic therapy, laser surgery and optogenetics, in which fewer scanning points are required.

5.2 Time-reversed Ultrasound Microbubble Encoded Optical Focusing

In this chapter, we present a new technique, time-reversed ultrasound microbubble encoded (TRUME) optical focusing, which can focus light with improved efficiency and sub-ultrasound wavelength resolution. This method ultrasonically destroys microbubbles, and measures the wavefront change to compute and render a suitable time-reversed wavefront solution for focusing. We demonstrate that the TRUME technique can create an optical focus at the site of bubble destruction with a size of $\sim 2\,\mu$m. We further demonstrate a two-fold enhancement in addressable focus resolution in a microbubble aggregate target by exploiting the nonlinear pressure-to-destruction response of the microbubbles. The reported technique provides a deep

tissue-focusing solution with high efficiency, resolution, and specificity.

5.2.1 Ultrasound Microbubble as a Guidestar

Creating an optical focus inside a scattering medium such as biological tissue has great potential in various applications. However, optical scattering, a dominant lightmatter interaction within biological tissue, poses a very significant challenge. Recent developed wavefront shaping techniques have begun to address this [20, 21, 76, 117, 118] by exploiting the deterministic and time-symmetric nature of scattering. Focusing light through scattering media has been realized by iterative optimization methods [12, 76], optical phase conjugation (OPC) [19, 42, 119–122], and direct measurement of the transmission matrix at large scale [13, 110, 123].

Determining the correct wavefront to focus light from outside of a scattering medium to a point within requires a feedback or tagging mechanism. Typically, these mechanisms arise from a physically localized guidestar point. Examples include second harmonic generation [111], fluorescence [124, 125] and kinetic [126, 127] targets. However, if dense and randomly distributed sets of guidestars are present, these techniques fundamentally lack addressability .

Alternatively, ultrasound-assisted techniques, such as photoacoustic-guided [110, 128–130] and time-reversed ultrasonically encoded (TRUE) [45, 93, 94] optical focusing techniques, employ a focused ultrasound beam as a 'virtual guidestar'. Unlike the above techniques, it is easy to move or scan an ultrasound focus to new positions. While TRUE has a speed advantage over the photoacoustic approach, the TRUE guidestar is generally weak and typically $< 1\%$ of the probe light field that passes through the ultrasound focus is tagged [114, 131]. Moreover, the resolution achieved is limited by the ultrasound focus size. Although more advanced TRUE techniques, such as iterative TRUE [95, 116, 132] and time reversal of variance-encoded light [41], may break this resolution barrier, it comes at the expense of time. For practical biological applications with tight time constraints, efficient and fast techniques are highly desired.

Here we present a high resolution, deep tissue optical focusing technique termed time-reversed ultrasound microbubble encoded (TRUME) optical focusing. Microbubbles have been widely used in ultrasonic imaging as ultrasound contrast agents because they generate stronger echoes and nonlinear acoustic signals compared with surrounding tissue [133,134]. Several other advantages of microbubbles are their small size compared with typical ultrasound wavelengths, which enables acoustic super-resolution imaging [135–137], and their ability to enable ultrasound modulated optical imaging inside scattering media [138–140]. Furthermore, like fluorescent markers, microbubbles can be modified to bind to selected biomarkers, suggesting promise for functional imaging and therapeutic applications [133].

We demonstrate that the selective nonlinear destruction of microbubbles with a focused ultrasound beam can serve as an effective, highly localized and freely addressable guidestar mechanism. In brief, TRUME works by measuring the scattered optical field before and after the ultrasonic destruction of the microbubble. Subsequently, by playing back the phase conjugate version of the difference of these two fields, TRUME can generate a focus at the location of the destroyed microbubble. Although multiple foci could be created at the same time when multiple microbubbles are present within the original ultrasound focus, we show that careful selection of the ultrasound pressure can lead to destruction of microbubbles in an addressable volume that is smaller than the ultrasound focus. This is a result of the nonlinear pressure-to-destruction response curve associated with the microbubbles. This technique combines the advantages of both physical and virtual guidestars to provide efficient, fast and addressable deep tissue optical focusing.

5.2.2 Principle
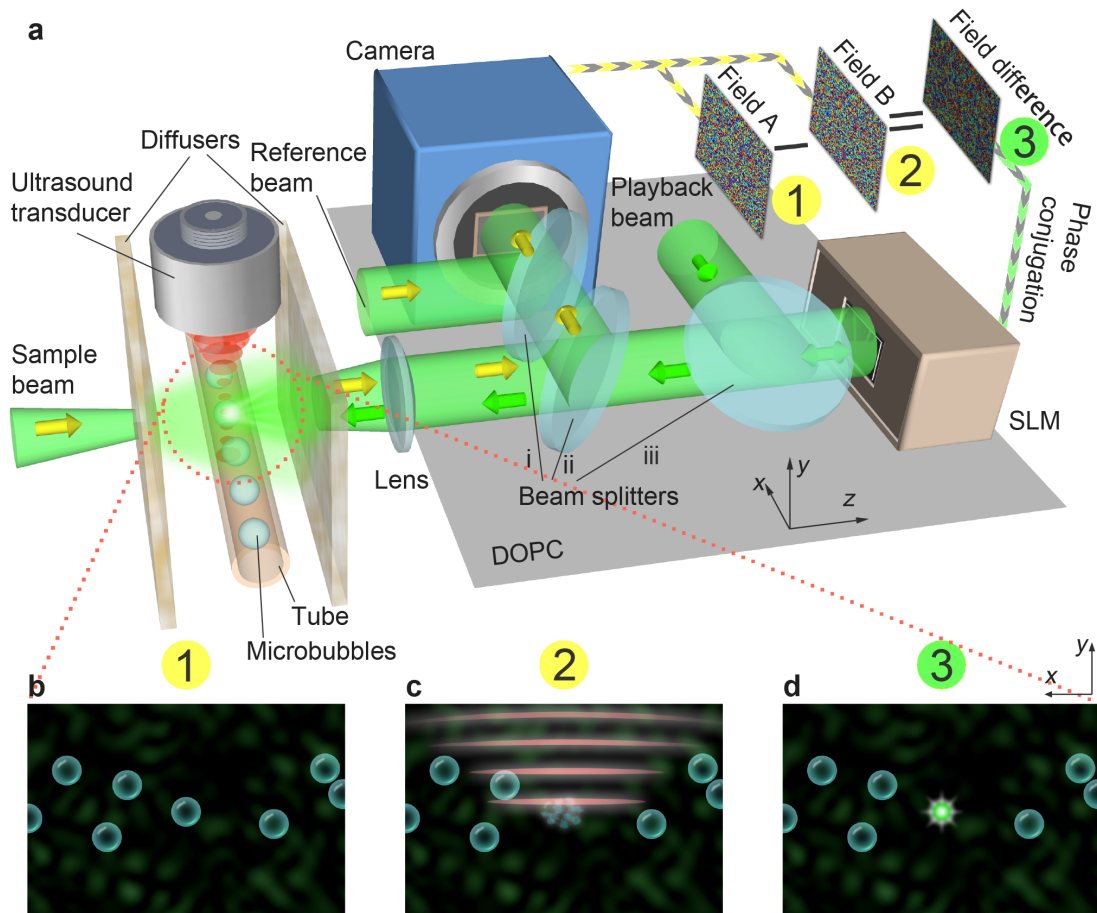
Figure 5.6: Principle of TRUME technique. (a) Experimental setup. The microbubbles perfuse inside an acrylic tube, which is sandwiched between two diffusers. A DOPC system is used as a phase conjugation mirror to time-reverse the light back to the sample. (bd) Illustration of TRUME optical focusing technique in three steps. At the first step, the camera of the DOPC system captures a transmitted optical field (Field A) before applying ultrasound to the sample (b). Ultrasound bursts are then used to destroy the targeted microbubble (c), resulting in a different optical field (Field B). The difference between two fields yields an optical field that appears to emerge from the destroyed microbubble. The conjugated phase of the difference field is then sent to the SLM to create a playback beam, which focuses light at the position of microbubble destruction (d). Yellow arrows, numbers and signal flows indicate recording process; green ones represent playback.

Our TRUME set-up uses a digital OPC (DOPC) system as its wavefront recording and playback engine [42, 132] (Fig. 5.6a). In the recording phase, the scattered field from the sample is recorded by the camera of the DOPC system. In the playback step, a phase-conjugated version of the recorded phase is displayed on the spatial light modulator (SLM) and a collimated blank beam is modulated to form the playback light field. Precise alignment of the camera and SLM allows high fidelity phase conjugate playback of the record field. Experimentally, this DOPC system is able to control $\sim 10^5$ optical modes simultaneously [91].

Here we demonstrate TRUME in transmission geometry (Fig. 5.6a), in which a sample beam transmits through the sample in the z direction and part of the scattered light is measured by the camera on the other side of the sample. An ultrasound beam is focused on the microbubbles embedded between two diffusers through water coupling. TRUME operates in three steps. First, an optical field (Field $\mathbf{A}$) is measured by the camera (Fig. 5.6b) with phase shifting digital holography [44]. Second (Fig. 5.6c), ultrasound is applied to destroy the targeted microbubble, immediately followed by the measurement of a second optical field (Field $\mathbf{B}$). The difference of the fields (Fields $\mathbf{A} - \mathbf{B}$) is the scattered field solution associated with the microbubble. The DOPC system computes this difference field and plays back a phase conjugate copy. Since the difference field primarily contains only information from the microbubble, the conjugated beam focuses to the position of the destroyed microbubble (Fig. 5.6d).

TRUME shares the same mathematical framework as guidestar techniques using kinetic objects [126, 127]. The optical field on the target plane $\mathbf{E}_t$ can be decomposed into a microbubble diffracted field $\mathbf{E}_m$ and a background field $\mathbf{E}_b$, which describes the field after microbubble destruction: $\mathbf{E}_t = \mathbf{E}_m + \mathbf{E}_b$. Since the camera and SLM contain discrete components, it is convenient to discretize $\mathbf{E}_m$ and $\mathbf{E}_b$ as column vectors with n complex elements, with each element mapping to an optical mode on the two-dimensional target plane. We may then connect this target field to the field on the measurement plane $\mathbf{E}'_t$ through a matrix equation: $\mathbf{E}'_t = \mathbf{T}\mathbf{E}_t = \mathbf{T}\left(\mathbf{E}_m + \mathbf{E}_b\right)$. Here $\mathbf{T}$ is an $m \times n$ matrix describing the scattering medium and $\mathbf{E}'_t$ is a column vector

of m elements, with each element mapping to an optical mode on the two-dimensional measurement plane. Similarly, the field measured after microbubble destruction can be given by $\mathbf{E}'_b = \mathbf{T}\mathbf{E}_b$. The difference field on the measurement plane is thus,

$$
\begin{aligned}
\mathbf{E}'_d &= \mathbf{E}'_t - \mathbf{E}'_b \\
&= \mathbf{T}\left(\mathbf{E}_m + \mathbf{E}_b\right) - \mathbf{T}\mathbf{E}_b \\
&= \mathbf{T}\mathbf{E}_m.
\end{aligned}
\tag{5.3}
$$

Here subtraction effectively removes the impact of the background field on the measurement plane, resulting in a field that appears to be scattered from the microbubbles only. Finally, we playback the conjugated field $\mathbf{E}'^{*}_d$ with an optical gain as provided by the playback beam (Fig. 5.6a). Assuming time-reversal symmetry, we may express playback as a multiplication with $\mathbf{T}$ from the left with the conjugate transpose of the difference field. Therefore, the playback field $\mathbf{E}_p$ on the target plane takes the form:

$$
\begin{aligned}
\mathbf{E}_p &= \alpha \mathbf{E}'^{*}_d \mathbf{T} = \alpha \left(\mathbf{T}\mathbf{E}_m\right)^{*}\mathbf{T} \\
&= \alpha \mathbf{E}_m^{*}\mathbf{T}^{*}\mathbf{T} \simeq \alpha\beta\mathbf{E}_m^{*}.
\end{aligned}
\tag{5.4}
$$

Here we assume minimal absorption within the sample to apply the approximation $\mathbf{T}^{*}\mathbf{T} \simeq \beta\mathbf{I}$, in which β is the fraction of scattered light field that is measured in the DOPC system and $\mathbf{I}$ is an identity matrix. The playback light effectively cancels out the random transmission matrix to refocus at the location of microbubble destruction.

The TRUME technique relies on a novel guidestar mechanism, popping a gas-filled microbubble using ultrasound, to generate the optical field difference. This mechanism leverages both the optical and acoustic refractive index mismatch between gas and liquid to accomplish efficient conversion of acoustic signal to optical signal. Given the fact that microbubbles have excellent biocompatibility, this guidestar combines advantages in optics, acoustics and biology to provide a solution for focusing light inside biological tissue.

5.2.3 Results

Direct Visualization of the Optical Focus
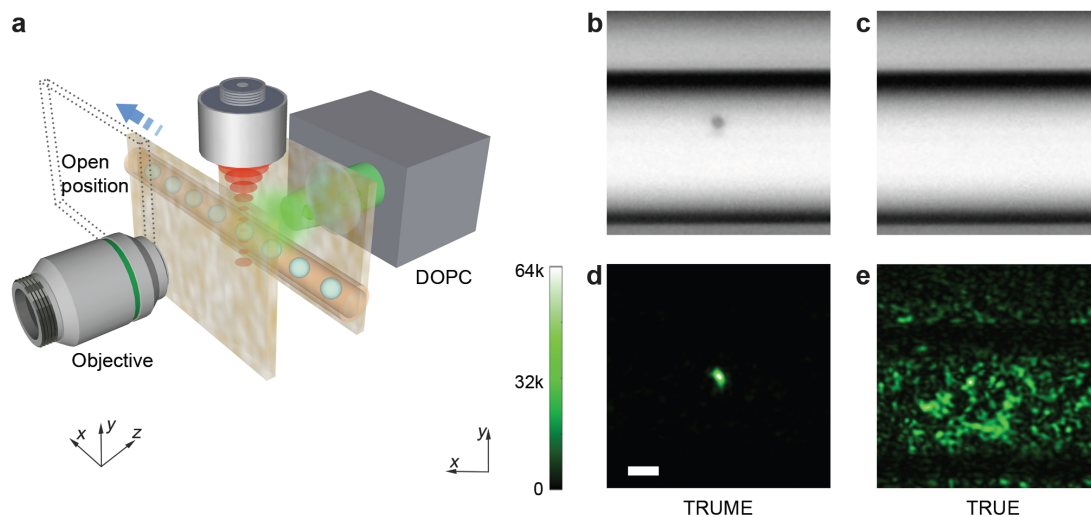
Figure 5.7: Visualization of the target plane. (a) Illustration of the observation set-up. The front diffuser was shifted to the open position before and after TRUME for direct visualization. A ×10 microscope system was used to observe the target plane. (b,c) Images of a microbubble before and after applying ultrasound. (d) Optical focus created at the position of microbubble destruction. (e) Focusing results of TRUE technique. Scale bar, $10\,\mu$m.

To validate TRUME focusing, we directly visualized the target plane using a × 10 microscope system (see Methods section) before and after the TRUME procedure. In this experiment, we shifted the front diffuser along the x direction (to the open position in Fig. 5.7a) for direct imaging of the target plane during the focusing phase. The target sample here is composed of microbubbles embedded in agarose gel within an acrylic capillary tube as shown in Fig. 5.7b. Immediately after measuring the first optical field, a 20-MHz focused ultrasound beam was used to destroy one microbubble, followed by the measurement of the second field. We then imaged the target plane again to confirm the destruction of the microbubble (Fig. 5.7c) and directly visualized the focus created at the position of the destroyed microbubble (Fig. 5.7d). The measured peak intensity to background intensity ratio (PBR) of the

TRUME focus in Fig. 5.7d is ~ 510.

For comparison, we also measured the focusing profile of TRUE (Fig. 5.7e). The PBR of the TRUME focus is around two orders of magnitude higher than that of TRUE (PBR~ 2 in Fig. 5.7e), since the TRUME concentrates light at fewer optical modes and has a stronger modulation efficiency per mode.

We separately measured the modulation efficiency of ultrasound in a clear medium, and found that $\sim 0.5\%$ of light passing through the ultrasound focus (2 MPa peak pressure) is modulated. In comparison, the proportion of light passing through the location of the bubble that is modulated by bubble destruction reaches $\sim 25\%$. This large difference in modulation efficiency is the primary reason why the TRUME guidestar offers a stronger focus.

Deep Tissue Optical Focusing
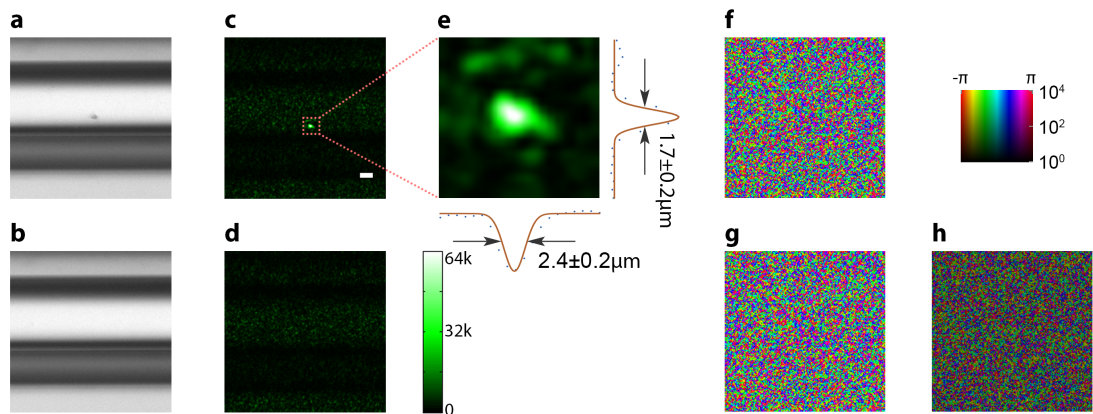
Figure 5.8: Optical focusing in 2-mm-deep chicken tissue. Two pieces of 2-mm-thick chicken tissue were used as diffusers. (a) A microbubble in a tube before destruction. (b) After destruction. (c) A light focus was created at the position of the destroyed microbubble (PBR $\sim$23). (d) The optical focus vanished as the SLM shifts 10 pixels in both x and y directions. (e) $10\times$ zoom-in image of the optical focus with quantified resolution. (f,g) Central part (200 pixels by 200 pixels) of the optical fields captured before (f) and after (g) the destruction of the microbubble. (h) Difference of the fields in f and g. Scale bar, $10\,\mu$m.

To study the performance of TRUME for focusing through biological tissue, we used two pieces of 2-mm-thick biological tissue as our diffusive medium. The experimental set-up matches that shown in Fig. 5.7a. The images of the microbubble before and after destruction are shown in Fig. 5.8a and b. We directly observed the target plane (Fig. 5.8c-e) after the TRUME process. An optical focus (Fig. 5.8c and e) was created using TRUME, with PBR of $\sim$23. Fitted Gaussian profiles (to the one-dimensional data through the centre of the focus in the x and y directions) show the focus full width at half maximum (FWHM; Fig. 5.8e) is 2.4 ± 0.2 mm in the x direction and 1.7 ± 0.2 mm in the y direction (95% confidence bounds). To confirm that this optical focus was created due to OPC, we shifted the SLM phase pattern in both x and y directions by 10 pixels. As shown in Fig. 5.8d, the optical focus vanishes as expected. The optical fields measured before and after microbubble destruction, as well as the subtracted field, are shown in Fig. 5.8f-h, respectively.

Demonstration of Flow Stream Monitoring
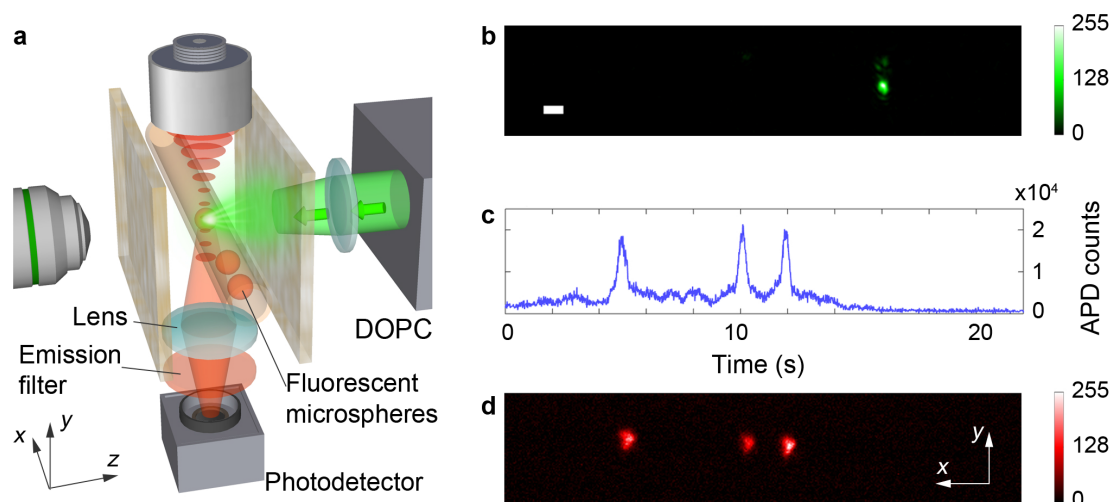
Figure 5.9: Demonstration of flow stream monitoring through a scattering sample. (a) Illustration of the experimental set-up. An external single-photoncounting module (SPCM) was used to detect the excited fluorescence through the fluorescence filter. (b) A light focus was created with TRUME. (c) Photon counts recorded by the SPCM as the optical focus probed the flowing microspheres. (d) Image of the fluorescent microspheres after passing through the optical focus in the x direction. Scale bar, $10\,\mu$m.

One application of the TRUME focusing technique may be to perform cytometry behind a scattering media by using microbubbles, which are currently used as contrast agents in blood circulation ultrasound imaging [133]. To demonstrate this potential application (Fig. 5.9a), we mixed fluorescent microspheres (4 mm) and microbubbles in 1× phosphate buffered saline and pumped the solution through an acrylic tube. We first formed an optical focus, as shown in Fig. 5.9b, by implementing the TRUME technique to focus on a microbubble at the target location. Fluorophores that subsequently flow across the focus then interact with the focused light spot to emit fluorescence. The fluorescence was filtered with an emission filter and detected by a single-photon-counting module outside the scattering medium. The resulting signal is shown in Fig. 5.9c. After counting, the front diffuser was shifted to the open position and the fluorescent microspheres were imaged with an emission filter

for verification (Fig. 5.9d). The agreement of the results positively validates this proof-of-concept.

Addressable Focus Resolution Improvement

Our demonstrations of TRUME thus far destroy an isolated microbubble with a relatively large ultrasound focus (one to two orders of magnitude larger), forming one sharp optical focus. If multiple microbubbles are clustered together, then the ultrasound focus may destroy more than one bubble. In this scenario, TRUME will generate an optical 'focus' significantly broader than the focus we have discussed thus far. To distinguish the two focus types, we will use the term addressable focus to refer to the achievable TRUME focus in the scenario where microbubbles are dense.

The addressable focus size is statistically determined by the pressure-to-destruction response of the bubbles. Interestingly, the probability of microbubble destruction varies nonlinearly as a function of pressure. In the ideal case where all microbubbles have the same destruction threshold, one could set the peak ultrasound pressure to be right at the threshold so that only the microbubble at the centre of the ultrasound focus will be destroyed and therefore obtain an addressable focus size that is equal to the single bubble TRUME focus size. In practice, however, the actual pressure-to-destruction response curve is not a simple step function. Nevertheless, the more nonlinear the response curve is, the sharper the addressable focus we can achieve with TRUME.
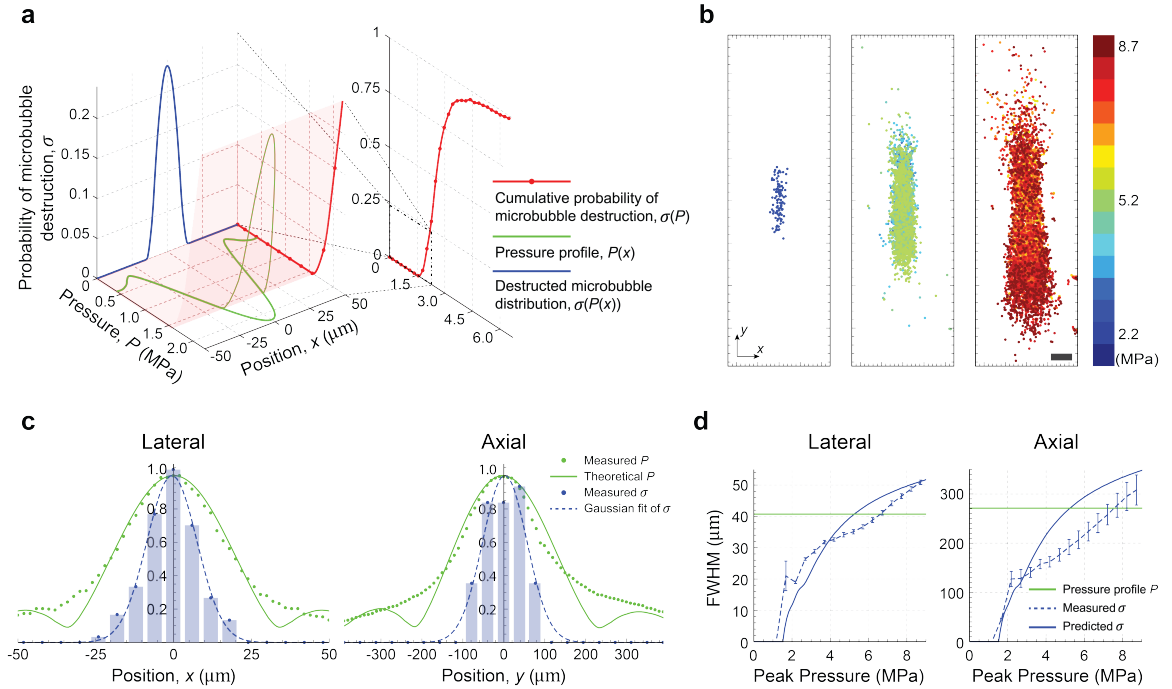
Figure 5.10: Addressable focus resolution improvement by exploiting nonlinear microbubble destruction. (a) Calculation of microbubble destruction probability distribution over position (blue) based on the measured cumulative distribution function of the microbubble destruction $\sigma(P)$ (red) and the theoretical ultrasound pressure profile $P(x)$ (green). (b) Two-dimensional distribution map of TRUME foci over pressure levels. This distribution map aggregates centroids of the TRUME foci from 135 sets of data. (c) Comparison of the TRUME focus probability distribution (histograms, with Gaussian fit) and the ultrasound pressure profile (green) in both lateral (left) and axial (right) directions. The histograms were calculated from the low-pressure map (left figure in b). (d) Theoretical (for example, FWHM of the blue curve in a) and experimental (for example, FWHM of the blue curve in c) TRUME addressable focus resolution over pressure. Green lines mark the FWHM of the ultrasound profile. Error bar indicates 95% confidence bounds. Scale bar in b, 50 μm.

To better characterize the pressure-to-destruction response and determine the TRUME addressable focus resolution achievable with our system, we experimentally measured the cumulative distribution function of the microbubble destruction $\sigma(P)$ by counting the number of microbubbles destroyed as a function of pressure. As shown in Fig. 5.10a (red), the cumulative distribution function reveals a strong nonlinear relationship between destruction probability and pressure. Given a focused

ultrasound profile $P(x)$ (Fig. 5.10a, green), we were able to calculate the microbubble destruction probability over position $\sigma(P(x))$ (Fig. 5.10a, blue), which predicts the addressable focus resolution of TRUME. The resulting profile is significantly narrower than the ultrasound pressure profile, implying that the nonlinear relationship would effectively improve the addressable focus resolution of TRUME.

To experimentally confirm the improvement of addressable focus resolution of TRUME, we used a thin microbubble sheet to visualize the distribution of the foci as ultrasound pressure increases. To cover the entire ultrasound focus $(-6\,\mathrm{dB})$ with the current observation system and further improve the resolution, we used a 45-MHz, high numeric-aperture ultrasound beam with a measured beam diameter of $\sim 40\,\mu\mathrm{m}$ and focal zone of $\sim 270\,\mu\mathrm{m}$ $(-6\,\mathrm{dB})$ in this experiment. We applied 15 levels of ultrasound pressure (linearly from 1.7 to 8.7 MPa) to the sample and measured the fields before and after each insonation. We then played back the corresponding field difference sequentially, recorded the resulting focus patterns, and applied a watershed algorithm to extract each focus centroid. To collect meaningful statistics, this process was repeated 135 times at different unaffected regions of the microbubble sheet. We aggregated the measured TRUME focus centroids into a statistical map as shown in Fig. 5.10b, where foci are displayed in three pressure groups. The profile of the foci broadens as the ultrasound pressure becomes higher, confirming the nonlinearity effect in TRUME.

To quantify the addressable focus resolution improvement, we calculated the FWHM of Gaussian profiles that are fitted to the histograms of each statistical map along both lateral (x) and axial (y) directions. Figure 5.10c shows the Gaussian fits and histograms of the lower pressure group $(< 2.2\,\mathrm{MPa}$, Fig. 5.10b, left) where microbubbles start to collapse. We also measured the ultrasound pressure profiles, which closely match with their theoretical profiles in both directions. The FWHM of the Gaussian fit to the centroid histogram in the lateral (x) direction is $19\,\mu\mathrm{m}$, while that of the theoretical ultrasound focus is $40\,\mu\mathrm{m}$. Likewise, the FWHM of the TRUME addressable focus along the axial (y) direction is $130\,\mu\mathrm{m}$, which is also lower than that of the ultrasound focus $(270\,\mu\mathrm{m})$. We further studied the effect of

ultrasound pressure on the nonlinearity-induced resolution improvement by calculating the FWHMs of the Gaussian fits of both the theoretical microbubble destruction distribution (for example, blue curve in Fig. 5.10a) and TRUME focus histogram profiles (for example, blue curve in Fig. 5.10c) at various pressure levels. As shown in Fig. 5.10d, both experimental and theoretical FWHMs are lower than that defined by the ultrasound focus (green line) when the ultrasound pressure is $<\sim 5\,\mathrm{MPa}$. The discrepancy between these two curves is attributable to variations between the samples.

5.2.4   Summary and Outlook

Combining the advantages of a physical and a virtual guidestar, TRUME can selectively focus light to a micron-sized spot in deep tissue, if the distribution of microbubbles it targets is sufficiently sparse. When the microbubble distribution is dense, we show that TRUME may still achieve an addressable focus resolution ~ 2 times higher than that defined by its ultrasound focus. As this method simply requires two measurements and no iterations, it is intrinsically fast and a good match with in vivo applications. Next, we list several factors that affect TRUME performance and outline several of its potential applications.

The size of an individual focus depends on that of the microbubble that is typically at micrometre scale, approximately tenfold smaller than a TRUE focus. Although ultrasound focus could cover multiple microbubbles, TRUME further confines the targeting range by taking the advantage of the nonlinear relationship between microbubble destruction probability and ultrasound pressure. The addressable focus resolution improvement was largely limited by the broad size distribution of the microbubbles, and thus can be enhanced by reducing the standard deviation of the radius of microbubbles, via separation techniques [141] or methods based on established protocols [142, 143]. Alternatively, simultaneously focusing to multiple microbubble locations might also be a desired experimental goal, as when using microbubbles as selective markers (for example, binding to certain disease markers) [133].

The PBR of TRUME is measured to be two orders of magnitude greater than that of TRUE (~ 510 versus ~ 2, using a ground glass diffuser sample and the set-up in Fig. 5.7). Two factors lead to this large PBR increase. First, TRUME practically encodes significantly fewer optical modes, even if multiple microbubbles are present within the ultrasound focus. Second, the modulation efficiency of TRUME is much higher than TRUE. In our experiment, we found $\sim 25\%$ modulation of the light passing through the TRUME guidestar. In comparison, a TRUE guidestar with a peak pressure of $2\,\text{MPa}$ only modulates $\sim 0.5\%$ of its contained light.

The time needed to destroy a microbubble depends on the mechanisms of microbubble destruction, which can be classified into fragmentation and diffusion [144]. Fragmentation occurs when ultrasound pressure is relatively high and the microbubble is destroyed on a timescale of microseconds, which suggests the TRUME mechanism is likely applicable to in vivo tissue experiments. In the case where low ultrasound pressure is used, acoustic driven diffusion is the dominant destruction mechanism. This process typically spans tens of microseconds, depending on both the ultrasound parameters (pressure, frequency, cycles and so on) and microbubble properties (size, shell material and encapsulated gas) [144]. In this paper, the ultrasound pulse duration was $28.6\,\text{ms}$ (one camera frame period), within which incomplete gas dissolution was also observed under certain circumstances, such as with low ultrasound pressure and a large microbubble diameter. This effect results in a size decrease rather than complete disappearance of the microbubble. Intriguingly, decreasing the size of the microbubble between the capturing of two optical fields also enables TRUME to form an optical focus at the targeted microbubble, because it shares the same effect as the complete microbubble destruction-inducing difference between two optical fields.

It should be noted that the lifetime of a TRUME focus depends on the tissue decorrelation time. To achieve a longer focusing duration, one may need to use the incomplete destruction approach. In this case, the TRUME focus can be repeatedly created by decreasing the size of the microbubble each time until complete destruction. Alternatively it is also possible to dynamically maintain the optical focus by using the ultrasound-driven microbubble oscillation effect [145], which is also able to induce

optical field variation.

Taking advantage of parallel field measurement, this DOPC-based technique creates optical foci in hundreds of milliseconds (~ 280 ms in our experiments), a timescale short enough for ex vivo or even some in vivo biological applications with appropriate tissue immobilization methods [146]. It should be noted that no frame averaging was needed for any of our TRUME experiments. Like other field subtraction approaches, the background fields need to remain highly correlated as the light intensity fraction encoded by the microbubble is typically very small. This requirement suggests that we must capture the two fields in a sufficiently short time period to overcome in vivo tissue decorrelation given that microbubbles can induce field variation during this time interval. Technically, this can be achieved by using a high speed camera. Off-axis holography-based field measurement or binary phase measurement would further improve the system speed by reducing the number of frames needed for field measurement [121, 147].

Microbubbles are usually made with albumin or lipid, which stabilizes high molecular weight gases, such as perflutren. Microbubbles like these have been widely used as ultrasound contrast agents and proven for some applications in the human body. Their biocompatibility makes them a promising optical guidestar in biological tissue. Besides ultrasonic imaging, microbubbles also have promising applications in gene and drug delivery [148], where their ultrasonic destruction can release a therapeutic payload. Furthermore, microbubbles can also be targeted to regions of disease by surface conjugation of specific ligands or antibodies, which bind to the disease markers [133]. Recently, genetically encoded gas nanostructures from microorganisms have been demonstrated as a promising candidate as molecular reporters [149]. All these applications imply that microbubbles have high specificity and selectivity, with which TRUME focusing may provide precise optical mediation for drugs, cells or molecules. Example applications range from selective photo-thermal therapy for targeting tumour cells [150, 151] to specific light delivery in optogenetics [152].

The prospect of using TRUME to perform imaging is less obvious and deserves some elaboration. Like other physical guidestar-assisted wavefront shaping tech-

niques, the TRUME focus position is collocated with the physical guidestar location and cannot be freely repositioned to perform raster scans. TRUME may potentially be combined with a newly described optical memory effect [153] to perform scanning and imaging. Specifically, it has been demonstrated that lateral translation of the input optical wavefront can retain some of its focusing ability through scattering media with high scattering anisotropy. TRUME can potentially be used to generate the initial focus that can then be freely scanned within a small proximal region using this optical memory effect.

Appendix to Section 5.1

Setup

The iTRUE system was custom-built, and the full system diagram is shown in the supplementary document. In our experiment, a 2.7 W, 532 nm wavelength Q-switch laser (Navigator, Spectra-Physics, USA) generated pulses with a 20 kHz repetition rate, a 7 ns pulse width and a 7 mm coherent length. The laser beam was split into a reference beam and probe beam. Both beams were spatially filtered by single mode fibres and collimated.

Ultrasound pulse trains were generated by a focused ultrasound transducer (50 MHz central bandwidth, 6.35 mm element diameter, 6 mm focal length; V3330, Olympus, USA), which provided a focal width of $\sim 30\,\mu$m (-6 dB). The ultrasound pulses were synchronised with the laser pulses, and a delay was added to make them coincide at the focus of the ultrasound transducer.

The collimated probe beam was coupled to an SLM (Pluto, Holoeye, Germany) by a 50/50 beam splitter. The reflected light from the SLM entered the sample through a 50 mm focal lens whose focus was located around the focal point of the transducer. The back scattered light from the sample was then reflected to an sCMOS camera (PCO.edge, PCO, Germany) by a 50/50 plate beam splitter (High-Energy Nd:YAG Laser, Newport Cooperation, USA). The camera plane and the SLM plane were

virtually matched through this beam splitter. The reference beam was combined with the backscattered modulated light using a 90/10 transmission-reflection beam splitter, creating an interfering pattern on the camera.

Phase Recording

In order to selectively detect the ultrasound-modulated light using a camera, the frequency of the reference beam was shifted by 50.010 MHz using an acousto optic modulator (AFM-502-A1, IntraAction, USA). Consequently, the unmodulated light was washed out because the 20 kHz laser pulses cannot lock at this beating frequency (50.010 MHz). However, the ultrasound pulses from the transducer were inverted one after another so that the beating frequency between the ultrasound modulated light and the reference beam could be locked [154, 155]. A 4-phase stepping digital holography method [44] was used to measure the phase of the ultrasound-modulated light. In this case, two clock sources were used in our system. The first was generated by a digital delay generator (DG645, Stanford Research Systems, USA), which generates a 20 kHz trigger signal for the laser and ultrasound. The pulse inversed ultrasound signal was generated by a function generator (AFG 3252, Tektronix, USA) and amplified by a RF power amplifier (30W1000B, Amplifier Research, USA). The reference beam signal was generated by another function generator of the same model, which was also synchronised with a digital delay generator. The other clock source was generated by a digital acquisition DAQ board (PCI6111, National Instruments, USA), which was used to synchronise the camera and the phase-shifting signal for digital hologram recording. This phase-shifting signal modulated the phase of the reference beam signal through the function generator by 0, $\pi/2$, π and $3\pi/2$. Therefore, four interfering patterns (I_0, $I_{\pi/2}$, I_π and $I_{3\pi/2}$) were captured on the camera (28 ms exposure time, 25 frames/s, 5 frames for each phase for averaging purposes). The complex field can then be calculated as $E = (I_0 - I_\pi) + i\left(I_{\pi/2} - I_{3\pi/2}\right)$, where i denotes the imaginary part.

Alignment

A protocol [91] was previously developed for the alignment of a DOPC system, which is the core of the iTRUE system. The DOPC system used in iTRUE differs from the previous system in that a separated reference beam and playback beam are required for simultaneous playback and recording in the iTRUE system. This requirement poses a larger challenge in aligning the DOPC system because more variables are involved. Three major steps were implemented to align the DOPC system. First, the flatness between the SLM and the collimated probe beam was assured by searching for an optimised compensation phase map. This step minimised problems due to aberration of the collimated lens and unevenness of the SLM surface. In this case, the SLM pixels were scanned for the maximum light intensity through the single mode fibre, which spatially filtered the probe beam before collimation. Second, the camera plane and the SLM plane were roughly aligned such that a discernable DOPC focus could be obtained through a thin scattering medium. Third, a digital wave propagation method was used to tune the virtual position of the camera or the SLM subject to the maximum light intensity of the DOPC focus.

Simulation

The simulation was based on a shot noise limited model. Starting with the initial probe beam, whose phase was uniformly distributed over 0–2π, the scattered light field inside a scattering medium could be obtained by multiplying the probe beam vector with a transmission matrix. An ultrasound profile with a Gaussian function shape was used to modulate the scattered field vector by scalar multiplication. The width of this Gaussian function was chosen such that the ratio between the number of controllable modes and the number of modes within the ultrasound focus was ~100, which is a typical number in TRUE [45]. The ultrasound modulated field was then propagated back through the scattering medium by multiplying the transpose of the transmission matrix. The resulting field was added to shot noise with a Poisson distribution, resulting in phase error. The phase of the conjugated field was used to

imprint a blank probe beam, which is the starting point of another iteration loop. Assuming that the recorded field is measured by 4-phase stepping digital holography, the SNR of the recorded interferogram, the phase error of the recorded field and the light intensity at the ultrasound focus can be simulated and recorded during each iteration loop.

Sample Preparation

To make a quantum dot sample, quantum dots (Qtracker 655 non-targeted quantum dots, Invitrogen) were mixed with a 1.5% agarose gel in the aqueous phase. The mixture was cast in a $500\,\mu$m thick mould and transferred to a glass cuvette. The empty space in the glass cuvette was filled with clear agarose gel of the same concentration.

To make a fluorescence bead sample, a $15\,\mu$m fluorescent bead (FluoSpheres 580/605 polystyrene microsphere, Invitrogen) was placed on top of a block of agarose gel in the solid phase. After verifying placement with a fluorescence microscope, the fluorescent bead was secured with extra agarose gel of the same concentration.

The cartilage was excised from the joint of a fresh chicken leg. The size of the cartilage was $10\,\text{mm}\,(x) \times 5\,\text{mm}\,(y) \times 2\,\text{mm}\,(z)$ in the coordinates shown in Fig. 5a. The muscle tissue was excised from a piece of chicken breast. The size of the tissue was approximately $10\,\text{mm}\,(x) \times 5\,\text{mm}\,(y) \times 1\,\text{mm}\,(z)$ in the same coordinate system.

Appendix to Section 5.2

Setup

The TRUME experiment was carried out in a custom-built set-up. A pulsed laser beam (532 nm wavelength, 7 ns pulse width, 20 kHz repetition rate and 7 mm coherent length) generated from a Q-switch laser (Navigator, Spectra-Physics) was spilt into three beams: a sample beam, a reference beam and a playback beam. Both of the sample beam and the reference beam were shifted by 50 MHz using an acousto-optical modulator (AFM-502-A1, IntraAction). The interference between the transmitted

sample beam and reference beam was measured by the camera (PCO.edge, PCO) of the DOPC system. The playback beam was modulated with the conjugated phase of the subtracted field by an SLM (Pluto, Holoeye), which was precisely aligned to the camera through a beam splitter.

The 20-MHz ultrasound burst was generated by a transducer with a 12.7-mm focal length and 6.35mm element diameter (V317, Olympus), and the 45-MHz ultrasound burst was generated by a transducer that has a 6-mm focal length and 6.35 mm element diameter (nominal frequency at 50 MHz, calibrated peak frequency at 44.4 MHz, V3330, Olympus). Both transducers were driven by an RF power amplifier (30W1000B, Amplifier Research).

To directly visualize the results, a custom-built microscope with a $20\times$ objective (SLMPlan N, Olympus) and a tube lens of 100 mm focal length was used to image the target plane to a charge-coupled device camera (Stingray F145, Allied Vision Technologies). To demonstrate the cytometry application, the fluorescent signals were filtered by a 561-nm long-pass (LP02-561RE-25, Semrock) and a 582/75-nm band-pass filter (FF01-582/75-25, Semrock) and detected by a single-photon-counting module (SPCM-AQRH-14, Perkinelmer).

Signal flow

The sample beam and reference beam were modulated by 50 MHz signals generated from two channels of a function generator (AFG 3252, Tektronix). The optical field transmitted through the sample was measured by the camera (exposure time: 20 ms, framerate: 35 fps) of the DOPC system using 4-phase shifting-based digital holography [44]. The phase shifting was synchronised with the camera exposure by controlling signals from a data acquisition card (PCI-6281, NI). The ultrasound burst signal (10 cycles, 10 μs interval) was generated by another function generator (4065, BK Precision) and time-gated (28.6 ms) by the data acquisition card.

Sample preparation

The microbubbles (Optison, GE health care) was diluted to 10% ($v/v\%$) in 1% ($w/w\%$) agarose gel in aqueous phase or $1\times$ phosphate buffered saline (demonstration of flow stream monitoring) and perfused in an acrylic capillary tube (inner diameter: $50\,\mu$m, outer diameter: $100\,\mu$m, Paradigm Optics), which was positioned inside a clear polystyrene cuvette. Polyacrylamide gel (10%) was used to fill the space in the cuvette to secure the capillary tube. Two diffusers ($10\times10\,$mm, 220 grit ground glass, Edmund Optics) were placed outside the cuvette in parallel with $\sim 10\,$mm distance in between. The microbubble sheet was $\sim 20\,\mu$m thick and sandwiched between two blocks of agarose gel with dimensions of $10\,$mm (x) $\times$ $10\,$mm (y) $\times$ $3\,$mm (z). The microbubble sheet was positioned between and parallel to the diffusers. The ultrasound beam was aligned to the microbubble sheet by maximizing the amplitude of the echo received from the focus.

In the flow stream monitoring experiment, fluorescent microspheres with $4\,$mm diameter (FluoSpheres 580/605, Life Science) were used as targets. In the ex vivo tissue experiment, fresh chicken breast tissue was used as the diffusive medium. For each tissue diffuser, a piece of 2-mm-thick chicken breast tissue slice ($10\,$mm (x) $\times 10\,$mm (y)) was sandwiched between two pieces of cover glass separated by a 2-mm spacer.

Ultrasound beam characterization

We calculated the theoretical ultrasound pressure field using the fast near-field method [156]. We first calculated the pressure fields at different single frequencies ranging from 1 to $100\,$MHz, and summed the profiles with a weight accounting for transducer response and frequency spectrum of ultrasound pulse train.

The ultrasound pressure was measured in room temperature water using a calibrated hydrophone (HGL-0085, Onda). To characterize the profile of the ultrasound beam, we operated the transducer in pulse-echo mode using a pulserreceiver (5900PR, Olympus) and scanned a line target (air filled polycarbonate tube, inner diameter

$22.5\,\mu$m, outer diameter $25\,\mu$m, Paradigm Optics) by translating the transducer in the lateral and axial directions, respectively [157]. This method provides a more accurate measurement than using the hydrophone because the active diameter of the hydrophone is larger than the waist of the ultrasound beam generated by the V3330 transducer. The peak-peak voltages of the echoes were measured by an oscilloscope (DPO 3012, Tektronix). Because the measurement was based on single cycle burst, side lobes were not shown.

Watershed Algorithm

We first binarized the image with a threshold that was seven times higher than the background intensity. This step outputs a binary image in which only the pixels around the peak have the value of 1. We then segmented the binary image with a watershed algorithm and extracted the centroid of each focal spot.

Chapter 6

Time-reversed Focusing Through Dynamic Scattering Media: Relation between Speckle Decorrelation and Time-reversal Fidelity

In living tissue, scatterers are highly movable and the movement can disrupt time-reversal symmetry when there is a latency in the OPC playback. In this chapter, we show that the motion-induced degradation of the OPC turbidity-suppression effect through a dynamic scattering medium shares the same decorrelation time constant as that determined from speckle intensity autocorrelation - a popular conventional measure of scatterer movement. We investigated this decorrelation characteristic time through a 1.5-mm-thick dorsal skin flap of a living mouse and found that it varies depending on the level of immobilization. This study provides information on relevant time scales for applying OPC to living tissues.[1]

---

[1]This chapter is reproduced with some adaptations from the manuscript Jang, M.*, Ruan, H.*, Vellekoop, I. M., Judkewitz, B., Chung, E. & Yang, C. Relation between speckle decorrelation and optical phase conjugation (OPC)-based turbidity suppression through dynamic scattering media: a study on in vivo mouse skin. Biomed. Opt. Express 6, 72 (2014). *: equal contributions. MJ contributed to developing the idea, deriving the theoretical relations, designing and conducting the experiments, analyzing the experimental results, and preparing the manuscript.

6.1 Time-reversal of Light through Dynamic Scattering Media
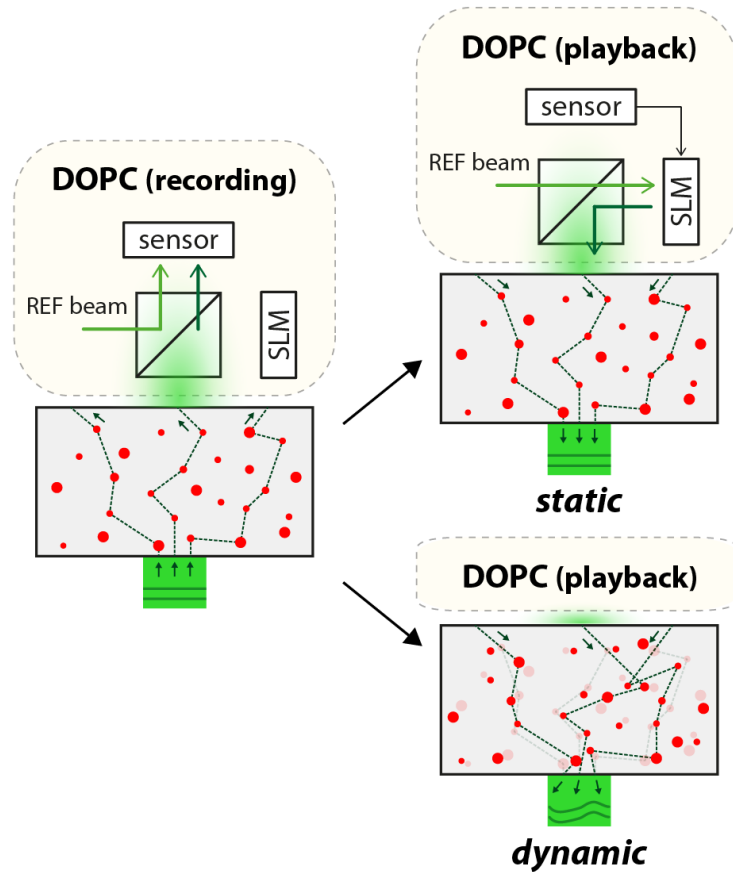
Figure 6.1: DOPC process through moving scatterers. As the first step of the DOPC process, the signal light beam (collimated beam) is incident on the multiple-scattering sample and its disordered wavefront is recorded from the sensor on the other side of the sample (left). Then, if the scatterers' configuration is static during the DOPC process-wavefront calculation and playback on the spatial light modulator (SLM) the OPC beam retraces the original scattering trajectories, which in turn reconstructs the signal light field from the opposite side (right top). However, if the scatterers move during the DOPC process, the time-reversal symmetry is broken so that the OPC beam cannot retrace its original trajectory. Thus, the original signal light field is not properly reconstructed (right bottom).

Despite recent technical improvements, in vivo application of the turbidity suppression technique remains quite limited. The primary obstacle is the movement

of scatterers inside tissue caused by essential physiological processes such as blood flow/pulsation, breathing and the tissues' fluidic environment. More specifically, when movement significantly changes the configuration of scatterers in the time interval between OPC wavefront recording and playback, the time symmetry is broken and the turbidity suppression effect is diminished (Fig. 6.1, right bottom).

In this study, we aim to show theoretically and experimentally that the degradation of OPC turbidity suppression shares the same decorrelation characteristic as the speckle intensity autocorrelation. We achieved $100\,\mathrm{ms}$ DOPC system latency by employing off-axis holography [84] for single-shot wavefront measurement and fast graphics processing unit (GPU) computation of the optical phase. Using the fast system (overall $200\,\mathrm{ms}$ system latency with the auto-alignment method [91]), we observed the equivalence between the fidelity of turbidity suppression and speckle intensity autocorrelation with tissue phantoms decorrelating at various time scales ranging from $50\,\mathrm{ms}$ to $\sim 10\,\mathrm{s}$. We then investigated the decorrelation characteristic of 1.5-mm-thick dorsal skin of a living mouse at different levels of immobilization and found that it ranged from $50\,\mathrm{ms}$ to $2\,\mathrm{s}$. Furthermore, we found that turbidity suppression can be achieved even at an extremely low-intensity autocorrelation (< 0.05), albeit its contrast is reduced correspondingly.

6.2 Relation between Speckle Decorrelation and Time-reversal Fidelity

6.2.1 Theory

In this section, we define two quantities: the speckle intensity autocorrelation function and the fidelity of OPC turbidity suppression, and we derive their theoretical equivalence. First, the normalized speckle intensity autocorrelation function, the correlation between speckle patterns at time t_0 and $t_0 + \tau$, is calculated from the temporal

sequence of multi-speckle images captured from the camera [158]:

$$g_2\left(\tau\right) \equiv \frac{\sum_m I_m\left(t_0\right) I_m\left(t_0+\tau\right)/M}{\left(\sum_m I_m\left(t_0\right)/M\right)\left(\sum_m I_m\left(t_0+\tau\right)/M\right)} - 1, \tag{6.1}$$

where $I_m\left(t\right)$ is the intensity of the transmitted scattered light, as recorded by the mth pixel of the sensor at time t, and M is the total number of pixels on the sensor. t_0 is the reference time at which the OPC wavefront is recorded. Here, $g_2\left(\tau\right)$ ranges from 0 to 1 as the "1" term is appended [158]. In our experiment, the time-lapse speckle pattern is captured in transmission geometry (with the signal beam). Assuming that the average transmittance does not change over time ($\overline{I} = \overline{I}\left(t_0\right) = \overline{I}\left(t_0+\tau\right)$), Eq. (6.1) is simplified to

$$g_2\left(\tau\right) \equiv \frac{\sum_m I_m\left(t_0\right) I_m\left(t_0+\tau\right)/M}{\overline{I}^2} - 1, \tag{6.2}$$

where $\overline{I}\left(t\right)$ is the average intensity, $\sum_m I_m\left(t\right)/M$. Assuming the scattering process is ergodic, this equation can be written in the ensemble-averaged form [158]

$$g_2 \equiv \frac{\langle I\left(t_0\right)\langle I\left(t_0+\tau\right)\rangle}{\langle I\rangle^2} - 1. \tag{6.3}$$

On the other hand, the fidelity of OPC turbidity suppression is quantified by the intensity of the phase-conjugated beam returning to the original input mode. In our experiment, the signal beam (input) was collimated. Thus, the time-reversed beam would also be collimated after it has counter-propagated through the scattering medium. We measured the intensity of the time-reversed beam on the input side of the sample (where the signal beam entered) by focusing it on the avalanche photo-diode (APD). We refer to the spot being focused on as the OPC spot. The OPC system records the wavefront at time t_0, and after some latency τ, it displays the phase conjugated wavefront. Using a transmission matrix formulation, the OPC spot

intensity is (assuming an input intensity of unity)

$$I_{OPC}\left(\tau\right) = A \frac{\left|\sum_m T_m\left(t_0 + \tau\right)T_m^*\left(t_0\right)\right|^2}{\left|\sum_m T_m\left(t_0\right)T_m^*\left(t_0\right)\right|^2} - 1, \tag{6.4}$$

where A is the OPC amplification. Thus, if there is no latency ($\tau = 0$), the reconstructed input mode has an intensity of A. $T_m\left(t\right)$ is the transmission matrix component relating the electric field of the original input mode to the transmitted electric field at the mth pixel on the OPC plane. The same transmission matrix component governs the field propagation in the reverse direction from the OPC plane to the input side of the sample due to the time-reversal symmetry of the scattering events. The transmission matrix component varies temporally because we assume that a dynamic sample was used. Then, we define the turbidity suppression fidelity as

$$F\left(\tau\right) = \frac{I_{OPC}\left(\tau\right)}{I_{OPC}\left(0\right)}. \tag{6.5}$$

The normalization term, $I_{OPC}\left(0\right)$, is the intensity of the OPC spot that would be obtained with a perfectly static sample. In our study, we experimentally determined the normalization factor by measuring the OPC spot intensity through the fully-cured tissue phantom (for the first part of the experiment) and the euthanized mouse (for the second part of the experiment).

To show the equivalence between $g_2\left(\tau\right)$ and $F\left(\tau\right)$, we use the Siegert relation [159]

$$g_2\left(\tau\right) = \beta \left|g_1\left(\tau\right)\right|^2, \tag{6.6}$$

which relates the intensity autocorrelation function to the field autocorrelation function, $g_1\left(\tau\right)$. β is an experimental constant, which is ideally 1 [159]. The constant accounts for the reduction in speckle contrast due to various factors, such as the number of sensor pixels per speckle and system noise [158, 159].

Here, $g_1\left(\tau\right)$, the field autocorrelation function, is given by

$$g_1\left(\tau\right) = \frac{\sum_m E_m^*\left(t_0\right) E_m\left(t_0 + \tau\right)}{\sqrt{\sum_m E_m^*\left(t_0\right) E_m^*\left(t_0\right)}\sqrt{\sum_m E_m^*\left(t_0 + \tau\right) E_m^*\left(t_0 + \tau\right)}}, \tag{6.7}$$

where $E_m(t)$ is the field of the transmitted scattered light at the mth pixel of the sensor. With the assumption of time-invariant average transmittance, the field auto-correlation function is

$$g_1(\tau) \equiv \frac{\sum_m T_m^*(t_0) T_m(t_0 + \tau)}{\sum_m T_m^*(t_0) T_m(t_0)}. \tag{6.8}$$

Using the Eqs. (6.4), (6.5) and (6.8) we then get:

$$F(\tau) = |g_1(\tau)|^2 \tag{6.9}$$

From Eqs. (6.6) and (6.9), the speckle intensity autocorrelation function is proportional to the normalized OPC spot intensity:

$$g_2(\tau) = \beta F(\tau). \tag{6.10}$$

Since $F(0) = 1$ by definition, β can be determined experimentally from the captured speckle pattern using the relation $\beta = g(0)$. It ranges from 0.8 to 1.0. Such high experimental values of $g_2(0)$ indicate that the camera exposure (9 ms in our case) is much faster than the sample dynamics. If the camera exposure is comparable to or slower than the scatterer movement, each pixel on the sensor integrates a temporal sequence of independent speckle fields so that the value of $g_2(0)$ that is effectively measured will be reduced. The temporal integration of many speckle fields will also correspondingly degrade the turbidity suppression fidelity $F(\tau)$ because the wavefront measured for the optical phase conjugation will be blurred.

6.2.2 Experimental Setup

We first performed a synchronized measurement of the speckle intensity autocorrelation, $g_2(t)$, and the turbidity suppression fidelity, $F(\tau)$, to show the equivalence between them. This set of experiments is performed with tissue phantoms and we will describe the details of the experimental scheme in this section.

Figure 6.2 shows the experimental setup. We used a 150-mW, 532-nm diode-pumped solid state laser as the light source. The laser beam is split into two beam paths: the signal beam and the reference beam. The signal beam is split into two paths for the digital OPC procedure and the speckle decorrelation measurement. Each signal beam has an intensity of $\sim 5\,\mathrm{mW}$ and its beam waist is $\sim 1\,\mathrm{mm}$. Figure 2(a) shows the beam paths for the OPC wavefront measurement. One of the signal beams is propagated through the scattering medium (here, a tissue phantom) and is guided to the sCMOS camera (pco.edge 5.5, PCO) through a $1\times$ telescope system composed of a pair of 15-cm focal length plano-convex lenses. The telescope system optically conjugates the DOPC plane to the back-focal plane of the signal collecting lens (2.5-cm focal length plano-convex lens). By obliquely guiding ($\sim 1.8\,^{\circ}$) the signal beam to the sensor plane (while the collimated reference beam is normally incident), we are able to use the off-axis holographic method. Thus, we calculate the signal beam's wavefront from a single interferogram which is captured from the sCMOS camera (sCMOS1) [84]. The speckle size of the signal beam is set to $\sim 6 \times 6$ and the camera's ROI is 1920×1080. In turn, we measure and conjugate the phase of around 50,000 optical modes.

Figure 6.2(b) shows the beam paths for the OPC playback. A phase-conjugated copy of the measured wavefront is displayed on the phase-only spatial light modulator (PLUTO phase only, Holoeye); next the SLM-reflected reference beam (OPC beam) retraces the signal beam's original scattering trajectories (Fig. 6.2(b)) and leaves the sample as a collimated beam that is directed onto an APD (SPCM-AQRH-14, PerkinElmer) and a CCD sensor (pixelfly qe, PCO). We quantified the turbidity suppression fidelity from the OPC beam intensity measured from the APD. The CCD is used to directly confirm the presence of the OPC spot.

The latency of the DOPC system - the time required for the wavefront measurement (30 ms), data processing (30 ms), and display on the SLM (30 ms) - is around 100 ms. The off-axis configuration reduces the time for the wavefront measurement as it requires a single interferogram for a wavefront measurement. However, compared to the phase-stepping methods, it measures a smaller number of optical modes. Be-

cause the off-axis methods involve the Fourier transform as well as an inverse Fourier transform of a large matrix (1920 × 1080), the computation load was significant. Therefore we used a high-end GPU (GeForce GTX TITAN, NVIDIA) to enhance the data processing speed. In this study, we employed a digital auto-alignment method to maximize the DOPC performance, which requires an additional 100 ms of computation time [91]. The overall system latency is therefore around 200 ms.
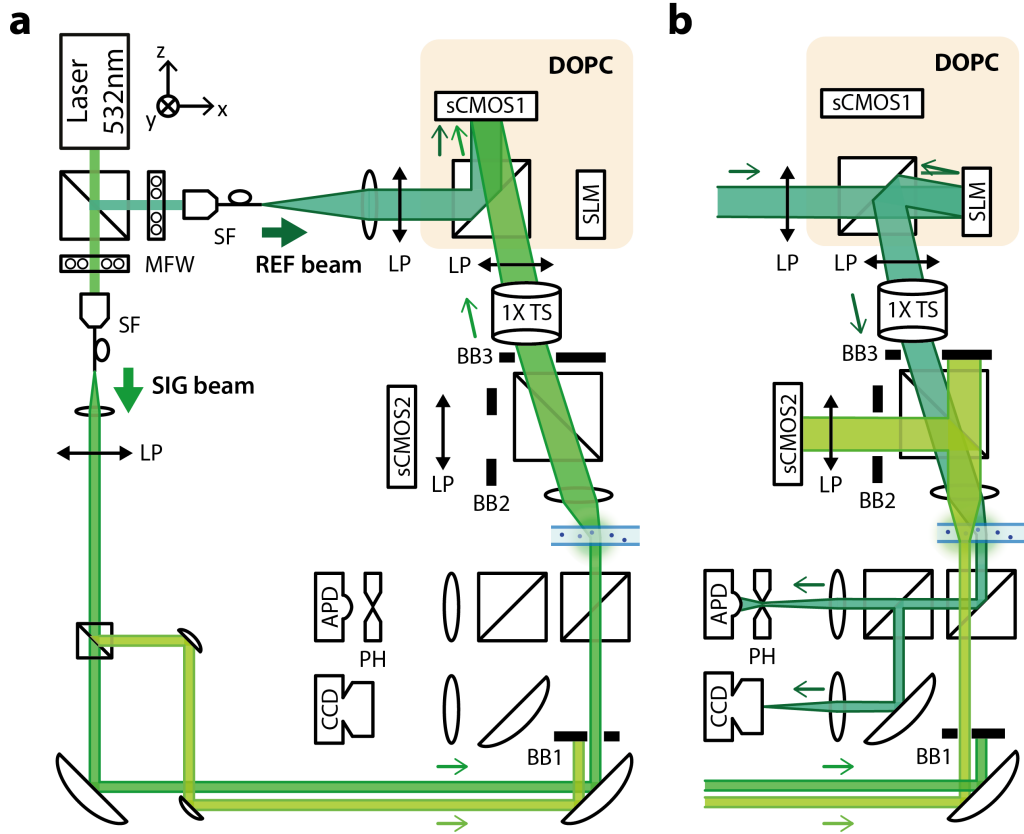
Figure 6.2: Experimental setup. (a) The experimental setup used for the tissue phantom and the beam paths used for wavefront measurement. The laser beam is split into two beam paths: the signal beam and reference beam. The signal beam is split into two paths: one for the speckle autocorrelation measurement and one for the DOPC procedure. The signal beam for the DOPC procedure propagates through the tissue phantom and is obliquely guided (1.8°) on the sensor plane (sCMOS camera 1) so that we are able to use the off-axis holographic method. (b) The experimental setup and beam paths used for the synchronized measurement of the speckle autocorrelation function and OPC spot intensity. The phase-conjugated copy of the measured wavefront is displayed on the SLM. The reconstructed OPC beam is measured from the APD and the CCD. sCMOS camera 2 capturing the transmitted speckle pattern.

Because light transmittance through scattering media is low, we adjust the motorized filter wheel (FW103, Thorlabs) to switch the light intensity between the phase recording and the playback. When we play back the phase-conjugated beam, we increase the reference light intensity so that we can clearly measure the reconstructed input mode from the other side of the scattering medium. When we record the wave-

front, we decrease the reference light with the motorized filter wheel so that we do not saturate the camera pixels. For the off-axis methods, we set the intensity ratio between the reference beam and the signal beam to roughly 5:1.

During the DOPC procedure, the other signal beam path, which is not used for the DOPC procedure, is guided to the sCMOS2 through the scattering media. sCMOS2 simultaneously captures the time-lapse multi-speckle pattern from which we calculate the speckle autocorrelation function. The speckle size is $\sim 6 \times 6$ pixels and the camera's region of interest is 160×160 pixels. Statistical stability is assured by the large number of speckles (~ 700 speckles). The exposure time and frame rate is set to $9\,\mathrm{ms}$ and $100\,\mathrm{s}^{-1}$, respectively. Because the beam paths for the DOPC procedure and speckle decorrelation measurement are spatially separated, we can block the problematic back-reflections and observe the clear speckle pattern with the sCMOS camera on one side of the sample while simultaneously observing the OPC spot with the CCD camera and the APD on the other side of the sample. This approach is only valid when the sample's dynamics are spatially homogeneous, as we have employed two different beam paths. Therefore we are able to perform the synchronized measurement with an artificial-tissue phantom.
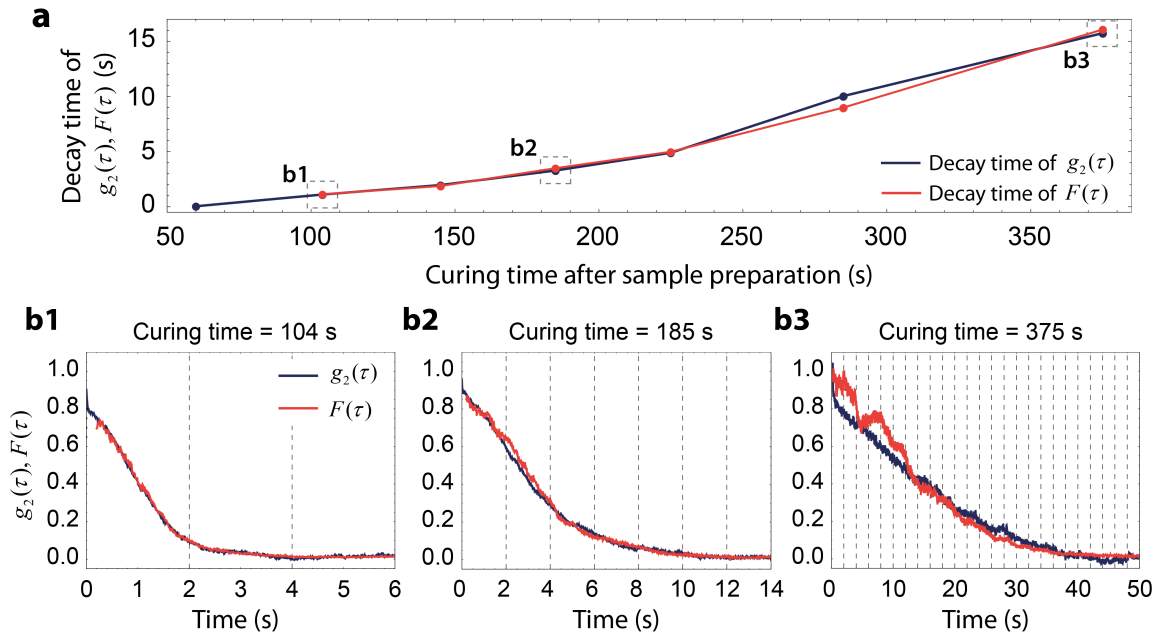
6.2.3 Result

Figure 6.3: Simultaneously-measured speckle intensity autocorrelation function and the OPC spot intensity through a tissue phantom. (a) $1/e$ decay time of the speckle intensity autocorrelation function and OPC spot intensity. As gel is cured at room temperature, the decay time becomes longer. This shows that the degradation of the OPC turbidity suppression shares the same time constant as the speckle decorrelation. For the first measurement, after $60\,\mathrm{s}$ of curing time, the OPC decay time could not be measured because the decorrelation is faster than the system latency. (b1–b3) The speckle autocorrelation function (blue) and the turbidity suppression (red) at different curing times: the time axis in b1, b2 and b3 are referenced at the curing time of $104\,\mathrm{s}$, $185\,\mathrm{s}$ and $375\,\mathrm{s}$ respectively. For different time scales, the two curves show close agreement in the time characteristic. In b3, greater fluctuation in the OPC spot intensity and the speckle autocorrelation function are observed as a result of the interference between the stable portion (changing slowly) and the decorrelating portion of the sample-transmitted light field.

The 3.5-mm-thick tissue phantom sample was made with 1% agar gel (Invitrogen) with 2% Intralipid (Invitrogen). The corresponding scattering/absorption coefficient and anisotropy constant are $9\,\mathrm{mm}^{-1}$, $0.002\,\mathrm{mm}^{-1}$, and 0.85, respectively [160]. We mixed the Intralipid with the agar in an aqueous phase and performed several sets of synchronized measurements before the gel was completely cured. Figure 6.3(a) shows

the decay time of the speckle intensity autocorrelation function (blue line) and the OPC turbidity suppression fidelity (red line) measured over the course of curing. Here, the decay time is defined as the time in which the speckle autocorrelation function and the turbidity suppression fidelity drops to $1/e$. The decay time becomes longer as the gel solidifies. As theoretically derived, we observed a good match between the two time constants. The profile of turbidity suppression fidelity shows a significant match to the profile of speckle autocorrelation function in various time scales as well (Fig. 6.3(b)). Each curve from the synchronized measurement is referenced at a different curing time (104 s, 185 s and 375 s). Because of the DOPC system latency and the computation time required for digital auto-alignment, the OPC spot intensity is observed ~ 200 ms after the wavefront measurement.

6.3 Decorrelation Characteristic of Dorsal Skin Flap of Mouse

6.3.1 Experimental Setup
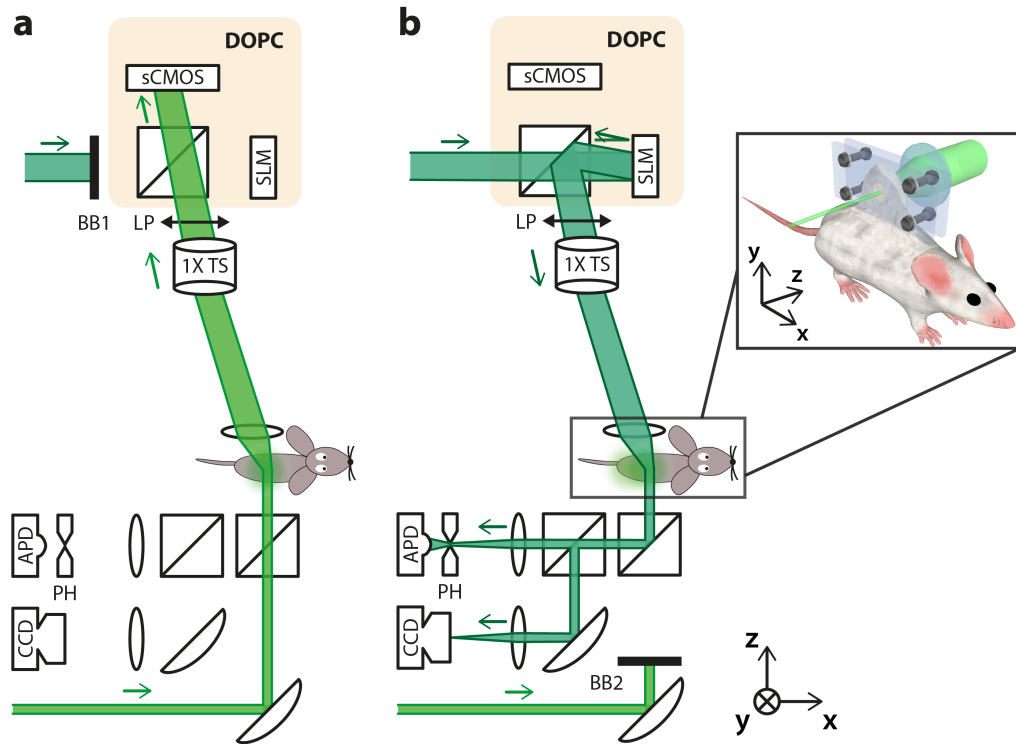
Figure 6.4: Experimental setup. The laser source, spatial filters, collimation lens shown in Fig. 6.2 are omitted. (a) The experimental setup used for the mouse dorsal skin flap and the beam paths used for the speckle measurement. The signal beam path used for the DOPC procedure was used for speckle measurement as well for the mouse dorsal skin flap. The time-lapse speckle pattern is measured with the sCMOS camera in the DOPC system. The reference beam is blocked. (b) The experimental setup and beam paths used for the measurement of the OPC spot intensity. The reconstructed OPC beam is measured from the APD and the CCD. The inset shows the mouse dorsal skin flap model we used. 1× TS = 1× telescope; PH = pinhole; BB = beam block; LP = linear polarizer; SLM = spatial light modulator; sCMOS = scientific CMOS camera; CCD = CCD camera; APD = avalanche photodiode.

We characterized the speckle decorrelation time of the mouse dorsal skin flap with three different configurations: 1) a laser beam incident on the skin flap ($\sim 1.5\,\mathrm{ms}$ thick) pinched by a pressure of $\sim 5\,\mathrm{psi}$, 2) the skin flap where its surrounding region is pinched by a pressure of $\sim 5\,\mathrm{psi}$, and 3) the unclamped skin with minimal immobilization. We also reconstructed the OPC spot and measured its intensity decay. However, because the synchronized measurement setup (in Fig. 6.2) is not valid for the spatially inhomogenous sample (the mouse dorsal skin flap), we separately measured the speckle autocorrelation and the OPC spot intensity. All of these procedures were approved by the Institutional Animal Care and Use Committee at the California Institute of Technology.

Figure 6.4 shows the experimental setup. First, to measure the speckle intensity autocorrelation, the time-lapse multi-speckle pattern is captured from the sCMOS camera while blocking the reference beam (Fig. 6.4(a)). For the measurement of the turbidity suppression fidelity, we generated the time-reversed beam using the same procedure as described in Section 6.2 and monitored the OPC spot intensity with the APD as shown in Fig. 6.4(b). The measurement parameters, including the speckle size, exposure time and frame rate, are the same parameters we used in the experiment with the artificial tissue phantom.

The inset in Fig. 6.4 presents the schematics of the dorsal skin flap model (CD-1 mouse). The mouse was anesthetized using isoflurane gas and the hair of the dorsal skin was shaved to expose the skin. We pinched the dorsal skin ($\sim 1.5\,\mathrm{mm}$ thick, scattering coefficient and anisotropy constant of $\sim 8\,\mathrm{mm}^{-1}$ and ~ 0.8, respectively, for a 488-nm light source [161, 162]) with two acrylic plates and applied a pressure of $\sim 5\,\mathrm{psi}$ (as measured by Prescale, Fujifilm) with four screws holding the plates in place. We selected the pressure level so that it would be sufficiently higher than the animal's blood pressure ($\sim 2\,\mathrm{psi}$) [163].

6.3.2   Result
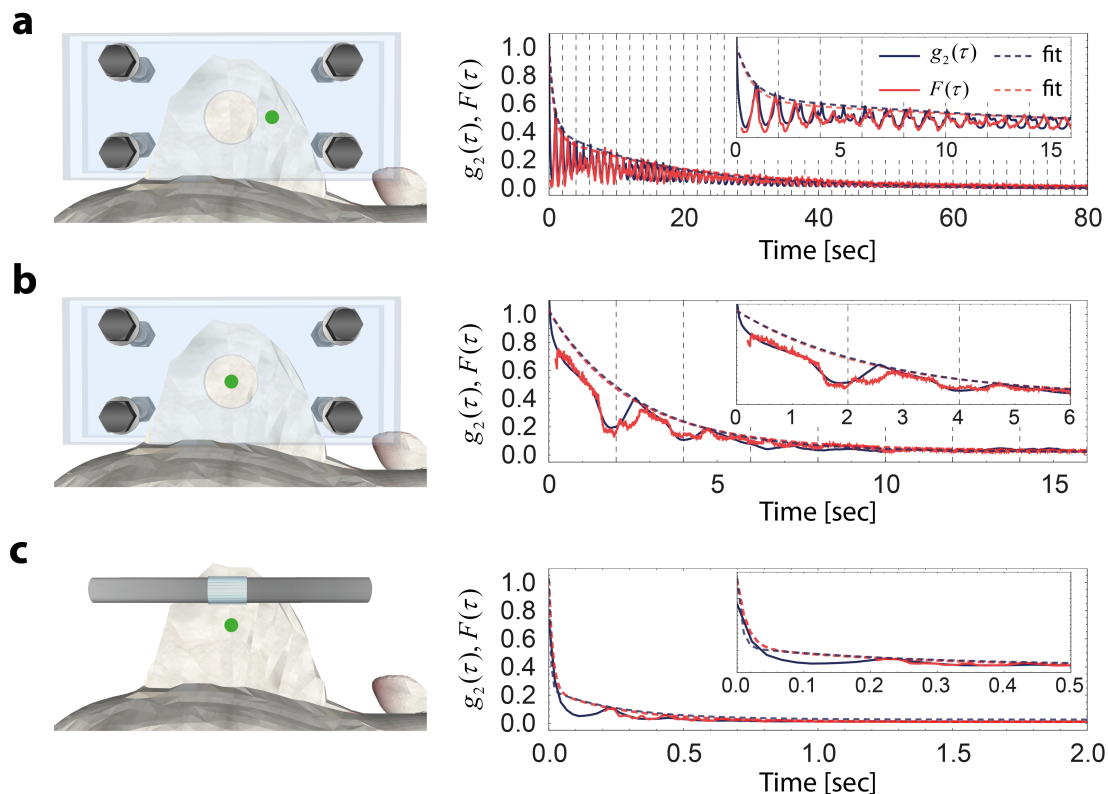
Figure 6.5: Speckle intensity autocorrelation function and turbidity suppression fidelity measured through a mouse dorsal skin flap. The solid lines (blue: speckle autocorrelation function, red: turbidity suppression fidelity) present the measured data and the dotted lines present two term exponential fit curves. (a) Because the dorsal skin is significantly immobilized (directly pinched with pressure of $\sim 5\,\text{psi}$), both the autocorrelation function and the OPC turbidity suppression fidelity decrease slowly ($\tau_{1/e} \sim 2\,\text{s}$). The periodic oscillation of the signal is caused by respiratory movement. (b) When only the surrounding region is pinched, the decorrelation characteristic time is only slightly changed. However, the autocorrelation function and the OPC spot intensity is not observed after $\sim 10\,\text{s}$. (c) If the skin is not immobilized by any physical means (tip of skin is glued to a rod) the decorrelation characteristic time is decreased significantly ($\tau_{1/e} \sim 50\,\text{ms}$). For all three cases, we observed a high level of agreement between the speckle intensity autocorrelation and the turbidity suppression fidelity profile. 12 profiles were averaged to sample different breathing and heartbeat phases.

The decorrelation characteristic varied significantly depending on the degree of immobilization. Figure 6.5 shows the averaged data profile and fit profile. For all three

cases, the profile is oscillating because of the scatterers' movement caused by the heartbeat and breathing. We first find a local maximum for each data trace and fit the peak points to the two-term exponential function. The two-term exponential function is based on a simple physical model in which the dynamics of the scatterers are composed of a fast part and slow part [164]. The decorrelation characteristic time is determined as the time in which the fit curve drops to $1/e$.

When the skin was pinched directly, as in Fig. 6.5(a), the decorrelation characteristic time of both curves is approximately $2.5\,\text{s}$; however, considerable correlation between speckle (> 0.1) patterns was observed until $\sim 30\,\text{s}$ after the wavefront measurement step. The turbidity suppression fidelity followed a similar tendency. When the surrounding region was pinched as in Fig. 6.5(b), the characteristic time decrease does not change significantly. This implies that the scatterer dynamics is not significantly affected in the time scale of a few seconds even though the scatterer is less immobilized. However, the autocorrelation function and the OPC spot intensity drops to the noise level after $\sim 10\,\text{s}$. For the unclamped skin, the decorrelation characteristic time is reduced to $\sim 50\,\text{ms}$ and the profiles drop to the noise level after $\sim 1\,\text{s}$ (Fig. 6.5(c)). In Fig. 6.5(a) and (b), as the scatterers moved from and return to their original position due to breathing, the intensity autocorrelation function and the turbidity suppression fidelity oscillate along with breathing frequency of 0.5–$1.0\,\text{Hz}$ (which may vary depending on the anesthetization conditions [165]). For the mouse dorsal skin flap, the measurement of the OPC spot intensity is not synchronized with the measurement of the speckle intensity autocorrelation function. Instead, we measured twelve sets of two profiles (on the same part of the skin flap) in an alternating way and averaged the profiles (Fig. 6.5(a)-(c)). The starting time of each measurement is randomly chosen to sample different breathing and heartbeat phases. Again, we observed a good match of the two curves for all three cases. We note that the relative phase between the measurement and breathing (or heartbeat) only affects the shape of the oscillating profile but not the phase and frequency, so that the peaks are still prominent in the averaged profiles.
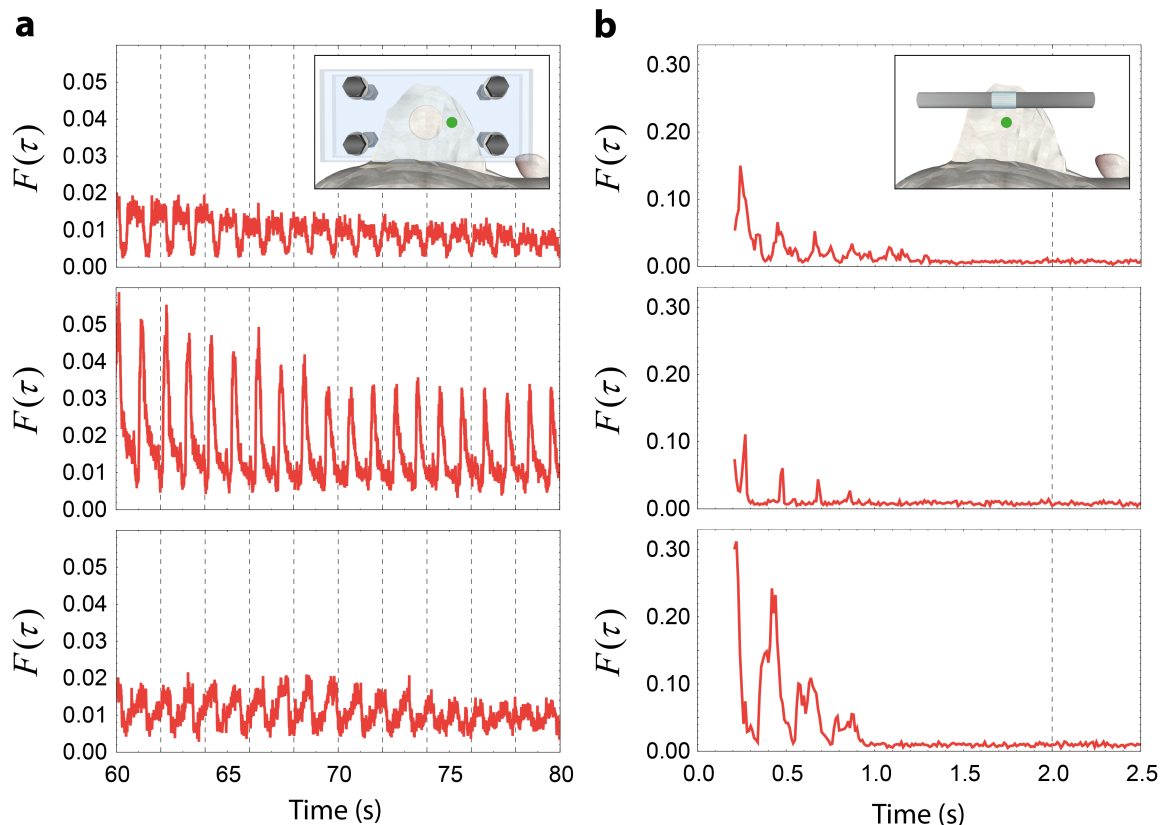
Figure 6.6: Three typical time traces of the turbidity suppression fidelity (without averaging) in the low speckle intensity correlation regime. (a) The dorsal skin is pinched directly, as in Fig. 6.5(a). (b) The dorsal skin is not immobilized as in Fig. 6.5(c). The shape of the profiles varies depending on the breathing and heartbeat phase.

In Fig. 6.6, we present the normalized OPC spot intensity in the low correlation regime without averaging (single data trace). Because the initial spot contrast was much greater than 1 (around 10^4, shown in Fig. 6.7), we expected to observe the OPC spot even with the correlation below 5%. Figure 6.6(a) shows the case when the dorsal skin is directly pinched (Fig. 6.5(a)). The spot oscillating along with a breathing frequency could still be clearly seen after 60 s from the wavefront measurement. The spot decayed very slowly in this regime. We believe that this is because a portion of the scattered light passes through a relatively stationary portion of the tissue and this portion preserves the time-reversal symmetry. For the unclamped skin (Fig. 6.6(b)), the OPC spot also survived with a low speckle autocorrelation but the decorrelation

characteristic time is much shorter than 1 s. It also shows the periodic oscillation with a frequency of about 5 Hz that is not easily seen in the averaged profile in Fig. 6.5(c). The frequency is consistent with the typical heart rate of an anesthetized mouse [165]. Because the oscillation at heartbeat frequency was not present in Fig. 6.6(a), we speculate that the oscillation observed through the unclamped skin originates from the pulsatory motion of the blood and vessels rather than from the whole-body movement caused by the heart beating. The main reason for the difference between the averaged profile and the single data profile is that each profile may change depending on the breathing and heartbeat phase when we record the OPC wavefront (Fig. 6.6).
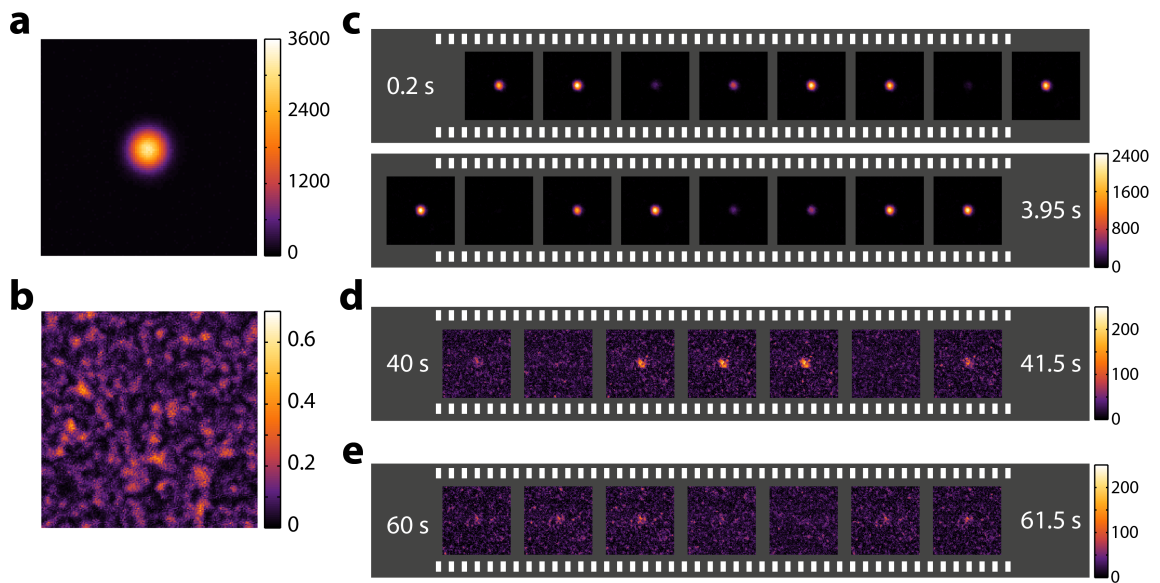
Figure 6.7: (a) The OPC reconstructed spot and (b) the background measured through the dorsal skin of the euthanized mouse. (c-e) Time-lapse images of the OPC reconstructed spot captured 0.2 s, 40 s, 60 s after the OPC wavefront measurement. The spot decays over time and oscillates at the breathing frequency. The frame rate is around 4 Hz.

The reconstructed OPC spot is also observed on the CCD camera. Figure 6.7(a) and (b) show the reconstructed spot and background pattern captured through the dorsal skin of the euthanized mouse. The background intensity was measured after we shifted the pattern (OPC wavefront) displayed on the SLM by 100 pixels in both directions. The actual background signal was very low and dominated by ambient

scattering light. We characterized the background intensity by averaging out many frames and subtracting the contribution from the ambient scattering. Figure 6.7(b) shows the background intensity after the subtraction of the experimental noise. The OPC spot contrast is estimated at $\sim 10^4$ from the measured intensities.

In Fig. 6.7(c)-(e), we present the time-lapse images of the OPC spot through the directly pinched dorsal skin. The starting time of each image sequence is $0.2\,\mathrm{s}$ (system latency), $40\,\mathrm{s}$ and $60\,\mathrm{s}$ after measuring the OPC wavefront. As measured from the APD, the spot decays over time and oscillates at the breathing frequency. The spot was observed after $60\,\mathrm{s}$. Because the background in Fig. 6.7(c)-(e) is dominated by the ambient scattering light, the spot contrast is not seen to be as high as expected. However, we note that the spot contrast should be estimated based on the properly measured background intensity (in Fig. 6.7(b)). For example, in Fig. 6.7(e), the spot contrast is $\sim$300 where the peak value is $\sim$100 and the averaged background intensity in Fig. 6.7(b) is $\sim$0.3. This value is well matched with the turbidity suppression fidelity of $\sim$3%, which is measured from the APD.

6.4   Summary and Outlook

We theoretically and experimentally investigated the relation between the speckle intensity autocorrelation function and the fidelity of the OPC turbidity suppression and found them to be equivalent. Based on this finding, we performed measurements through a live mouse dorsal skin flap ($\sim 1.5\,\mathrm{mm}$ thick) that underwent varying levels of immobilization. The decorrelation characteristic time ranged from $50\,\mathrm{ms}$ to $2.5\,\mathrm{s}$. The high initial spot contrast ($\sim 10^4$) naturally led to the survival of the spot at a low speckle autocorrelation. This implies that the OPC spot can survive for even longer when the initial spot contrast is high enough, which can simply be achieved by increasing the number of controllable optical modes (pixel number) in the DOPC system. This indicates the potential for using the OPC process for turbidity suppression of biological tissue because the feasibility of the OPC system can even be extended into the regime where the scatterer dynamics are much faster than the OPC system

speed.

We also found that the decorrelation time changes significantly depending on the level of immobilization. When the dorsal skin flap was directly pinched, we expected the scatterers' movements caused by blood flow/pulsation and its fluidic environment to be significantly limited. However, it resulted in the survival of the OPC spot for over 1 min, whereas the spot disappears in $\sim 50\,\mathrm{ms}$ for the unclamped dorsal skin. In other words, when tissue is immobilized, the stationary part of the tissue preserves the time-reversal property for a longer period. The characteristic time may vary depending on the thickness of tissue (number of scattering events), the type of tissue, and light collection geometry, as well as the level of immobilization. Interestingly, the unclamped skin presented a signal that oscillated along with heart rate while the immobilized (clamped) skin only presented oscillation along with the mouse's breathing rate. We believe that the heart rate oscillation is caused by a pulsatory motion involving blood and vessels that are limited by the pressure applied onto the dorsal skin. For practical biomedical applications, the wavefront at different phases of breathing and heartbeat may be averaged to create the non-oscillating OPC spot.

We optimized the DOPC system latency to $\sim 200\,\mathrm{ms}$ (with the auto-alignment method [91]) employing single-shot wavefront measurement (based on off-axis holography) and a fast computing unit. If a fast display device (e.g., a digital micromirror device) is utilized, the latency can be further shortened. We expect the one cycle of the DOPC procedure can be shortened by one order of magnitude if we optimize the data transfer time, memory read out time and display time. More specifically, the system operation time can be optimized in the following way. First the interferogram is directly transferred from the sensor to the field-programmable gate array (FPGA) board. Next the binarized wavefront of the signal beam is calculated on the board and transferred to the DMD control board. Finally the DMD displays the processed wavefront. Potentially, the integration of image sensor and spatial light modulator will also reduce the time required for the DOPC procedure [166]. Additionally, if more pixels (currently, around 10^6) are coordinated for the OPC process as indicated above, it seems highly probable that the OPC-based turbidity suppression technique

may be applicable to highly dynamic biological tissue, such as brain tissue.

Bibliography

[1] Yariv, A. & Yeh, P. *Photonics: optical electronics in modern communications* (Oxford University Press, 2006).

[2] Born, M. & Wolf, E. *Principles of optics: electromagnetic theory of propagation, interference and diffraction of light* (CUP Archive, 2000).

[3] Hecht, E. *Optics* (Addison Wesley, 2002).

[4] Lakowicz, J. R. *Principles of fluorescence spectroscopy* (Springer Science & Business Media, 2013).

[5] Vo-Dinh, T. *Biomedical Photonics Handbook: Biomedical Diagnostics* (CRC press, 2014).

[6] Wang, L. V. & Wu, H.-i. *Biomedical optics: principles and imaging* (John Wiley & Sons, 2012).

[7] Akkermans, E. & Montambaux, G. *Mesoscopic physics of electrons and photons* (Cambridge University Press, 2007).

[8] Freitas, R. A. *Nanomedicine, volume I: basic capabilities* (Landes Bioscience, 1999).

[9] Macovski, A. *Medical imaging systems* (Prentice Hall, 1983).

[10] Goodman, J. *Speckle phenomena in optics: theory and applications* (Roberts and Company Publishers, 2007).

[11] Beenakker, C. W. J. Random-matrix theory of quantum transport. *Reviews of modern physics* **69**, 731 (1997).

[12] Vellekoop, I. M. & Mosk, A. P. Focusing coherent light through opaque strongly scattering media. *Optics letters* **32**, 2309–2311 (2007).

[13] Popoff, S. M. *et al.* Measuring the Transmission Matrix in Optics: An Approach to the Study and Control of Light Propagation in Disordered Media. *Physical Review Letters* **104**, 100601 (2010).

[14] Dorokhov, O. On the coexistence of localized and extended electronic states in the metallic phase. *Solid State Communications* **51**, 381–384 (1984).

[15] Pendry, J. B., MacKinnon, A. & Pretre, A. B. Maximal fluctuationsA new phenomenon in disordered systems. *Physica A: Statistical Mechanics and its Applications* **168**, 400–407 (1990).

[16] Pendry, J. Universality classes and fluctuations in disordered systems. *Proc. R. Soc. Lond. A* **437**, 67–83 (1992).

[17] van Rossum, M. C. W. & Nieuwenhuizen, T. M. Multiple scattering of classical waves: from microscopy to mesoscopy and diffusion. *Reviews of Modern Physics* **71**, 86 (1998). arXiv:9804141.

[18] Marčenko, V. A. & Pastur, L. A. Distribution of eigenvalues for some sets of random matrices (1967).

[19] Yaqoob, Z., Psaltis, D., Feld, M. S. & Yang, C. Optical Phase Conjugation for Turbidity Suppression in Biological Samples. *Nature photonics* **2**, 110–115 (2008).

[20] Mosk, A., Lagendijk, A., Lerosey, G. & Fink, M. Controlling waves in space and time for imaging and focusing in complex media. *Nature photonics* **6**, 283–292 (2012).

[21] Horstmeyer, R., Ruan, H. & Yang, C. Guidestar-assisted wavefront-shaping methods for focusing light into biological tissue. *Nat Photon* **9**, 563–571 (2015).

[22] Efron, U. *Spatial light modulator technology: materials, devices, and applications*, vol. 47 (CRC Press, 1994).

[23] Rai-Choudhury, P. *MEMS and MOEMS Technology and Applications*, vol. 85 (SPIE Press, 2000).

[24] Tyson, R. K. *Principles of adaptive optics* (CRC press, 2015).

[25] Hardy, J. W. *Adaptive optics for astronomical telescopes* (Oxford University Press, 1998).

[26] Yariv, A. Phase Conjugate Optics and Real-Time Holography. *IEEE Journal of Quantum Electronics* **14**, 650–660 (1978).

[27] Akbulut, D., Huisman, T. J., van Putten, E. G., Vos, W. L. & Mosk, A. P. Focusing light through random photonic media by binary amplitude modulation. *Optics express* **19**, 4017–4029 (2011).

[28] Hellwarth, R. W. Generation of time-reversed wave fronts by nonlinear refraction. *JOSA* **67**, 1–3 (1977).

[29] Wang, V. & Giuliano, C. R. Correction of phase aberrations via stimulated Brillouin scattering. *Optics letters* **2**, 4–6 (1978).

[30] Lind, R. C. & Steel, D. G. Demonstration of the longitudinal modes and aberration-correction properties of a continuous-wave dye laser with a phase-conjugate mirror. *Optics letters* **6**, 554–556 (1981).

[31] Pepper, D. M., Fekete, D. & Yariv, A. Observation of amplified phase-conjugate reflection and optical parametric oscillation by degenerate four-wave mixing in a transparent medium. *Applied Physics Letters* **33**, 41–44 (1978).

[32] Auyeung, J., Fekete, D., Pepper, D. M. & Yariv, A. A theoretical and experimental investigation of the modes of optical resonators with phase-conjugate mirrors. *Quantum Electronics, IEEE Journal of* **15**, 1180–1188 (1979).

[33] Yariv, A., Fekete, D. & Pepper, D. M. Compensation for channel dispersion by nonlinear optical phase conjugation. *Optics Letters* **4**, 52–54 (1979).

[34] Gower, M. C. & Caro, R. G. KrF laser with a phase-conjugate Brillouin mirror. *Optics letters* **7**, 162–164 (1982).

[35] Dunning, G. J. & Lind, R. C. Demonstration of image transmission through fibers by optical phase conjugation. *Optics letters* **7**, 558–560 (1982).

[36] Bloom, D. M. & Bjorklund, G. C. Conjugate wave-front generation and image reconstruction by four-wave mixing. *Applied Physics Letters* **31**, 592–594 (1977).

[37] Levenson, M. D. High-resolution imaging by wave-front conjugation. *Optics letters* **5**, 182–184 (1980).

[38] Zel'Dovich, B. Y., Popovichev, V. I., Ragul'Skii, V. V. & Faizullov, F. S. Connection between the wave fronts of the reflected and exciting light in stimulated Mandel'shtam-Brillouin scattering. In *Landmark Papers On Photorefractive Nonlinear Optics*, 303–306 (1995).

[39] Fisher, R. *Optical phase conjugation.*

[40] Suzuki, Y., Lai, P., Xu, X. & Wang, L. High-sensitivity ultrasound-modulated optical tomography with a photorefractive polymer. *Optics letters* **38**, 899–901 (2013).

[41] Judkewitz, B., Wang, Y. M., Horstmeyer, R., Mathy, A. & Yang, C. Speckle-scale focusing in the diffusive regime with time reversal of variance-encoded light (TROVE). *Nature Photonics* **7**, 300–305 (2013).

[42] Cui, M. & Yang, C. Implementation of a digital optical phase conjugation system and its application to study the robustness of turbidity suppression by phase conjugation. *Optics express* **18**, 3444–55 (2010).

[43] Bellanger, C., Brignon, a., Colineau, J. & Huignard, J. P. Coherent fiber combining by digital holography. *Optics letters* **33**, 2937–9 (2008).

[44] Yamaguchi, I. & Zhang, T. Phase-shifting digital holography. *Optics letters* **27**, 1108–10 (1997).

[45] Wang, Y. M., Judkewitz, B., Dimarzio, C. a. & Yang, C. Deep-tissue focal fluorescence imaging with digitally time-reversed ultrasound-encoded light. *Nature communications* **3**, 928 (2012).

[46] Goodman, J. *Introduction to Fourier optics* (Roberts and Company Publishers, 2005).

[47] Li, J., Peng, Z. & Fu, Y. Diffraction transfer function and its calculation of classic diffraction formula. *Optics Communications* **280**, 243–248 (2007).

[48] Matsushima, K., Schimmel, H. & Wyrowski, F. Fast calculation method for optical diffraction on tilted planes by use of the angular spectrum of plane waves. *JOSA A* **20**, 1755–62 (2003).

[49] Feng, S., Kane, C., Lee, P. & Stone, A. Correlations and fluctuations of coherent wave transmission through disordered media. *Physical review letters* **61**, 834–837 (1988).

[50] Hell, S. W. Far-field optical nanoscopy. *science* **316**, 1153–1158 (2007).

[51] Hell, S. W., Schmidt, R. & Egner, A. Diffraction-unlimited three-dimensional optical nanoscopy with opposing lenses. *Nature Photonics* **3**, 381–387 (2009).

[52] Pawley, J. *Handbook of biological confocal microscopy* (Springer, 2006).

[53] Grier, D. G. A revolution in optical manipulation. *Nature* **424**, 810–816 (2003).

[54] de Nes, A. S., Braat, J. J. M. & Pereira, S. F. High-density optical data storage. *Reports on Progress in Physics* **69**, 2323 (2006).

[55] Hell, S. & Stelzer, E. H. K. Properties of a 4Pi confocal fluorescence microscope. *JOSA A* **9**, 2159–2166 (1992).

[56] Bahlmann, K., Jakobs, S. & Hell, S. W. 4Pi-confocal microscopy of live cells. *Ultramicroscopy* **87**, 155–164 (2001).

[57] von Bally, G. & Khanna, S. Optics in Medicine, Biology and Environmental Research. *Series on Optics Within Life Sciences, Elsevier Publishing Company* **1** (1993).

[58] Gu, M. & Sheppard, C. J. R. Three-dimensional transfer functions in 4Pi confocal microscopes. *JOSA A* **11**, 1619–1627 (1994).

[59] Leith, E. N. & Upatnieks, J. Holographic imagery through diffusing media. *JOSA* **56**, 523 (1966).

[60] McDowell, E. J. *et al.* Turbidity suppression from the ballistic to the diffusive regime in biological tissues using optical phase conjugation. *Journal of biomedical optics* **15**, 25004 (2010).

[61] Mudry, E., Le Moal, E., Ferrand, P., Chaumet, P. C. & Sentenac, A. Isotropic diffraction-limited focusing using a single objective lens. *Physical review letters* **105**, 203903 (2010).

[62] Cui, M., McDowell, E. J. & Yang, C. An in vivo study of turbidity suppression by optical phase conjugation (TSOPC) on rabbit ear. *Optics express* **18**, 25–30 (2010).

[63] Van Staveren, H. J., Moes, C. J. M., van Marie, J., Prahl, S. A. & Van Gemert, M. J. C. Light scattering in lntralipid-10% in the wavelength range of 400–1100 nm. *Applied optics* **30**, 4507–4514 (1991).

[64] Müllenborn, M., Dirac, H. & Petersen, J. W. Three-dimensional nanostructures by direct laser etching of Si. *Applied surface science* **86**, 568–576 (1995).

[65] Von Freymann, G. *et al.* Three-Dimensional Nanostructures for Photonics. *Advanced Functional Materials* **20**, 1038–1052 (2010).

[66] Lang, M. C., Staudt, T., Engelhardt, J. & Hell, S. W. 4Pi microscopy with negligible sidelobes. *New Journal of Physics* **10**, 43041 (2008).

[67] Commander, L. G., Day, S. E. & Selviah, D. R. Variable focal length microlenses. *Optics Communications* **177**, 157–170 (2000).

[68] Berge, B. & Peseux, J. Variable focal lens controlled by an external voltage: An application of electrowetting. *The European Physical Journal E* **3**, 159–163 (2000).

[69] Sato, S. Liquid-Crystal Lens-Cells With Variable Focal Length. *Japanese journal of applied physics* **18**, 1679–1684 (1979).

[70] Kuiper, S. & Hendriks, B. H. W. Variable-focus liquid lens for miniature cameras. *Applied Physics Letters* **85**, 1128–1130 (2004).

[71] Anselmi, F., Ventalon, C., Begue, A., Ogden, D. & Emiliani, V. Three-dimensional imaging and photostimulation by remote-focusing and holographic light patterning. *Proceedings of the National Academy of Sciences* **108**, 19504–19509 (2011).

[72] Curtis, J. E., Koss, B. A. & Grier, D. G. Dynamic holographic optical tweezers. *Optics Communications* **207**, 169–175 (2002).

[73] Nikolenko, V. SLM microscopy: scanless two-photon imaging and photostimulation using spatial light modulators. *Frontiers in Neural Circuits* **2**, 1–14 (2008).

[74] Szabo, V., Ventalon, C., De Sars, V., Bradley, J. & Emiliani, V. Spatially Selective Holographic Photoactivation and Functional Fluorescence Imaging in Freely Behaving Mice with a Fiberscope. *Neuron* **84**, 1157–1169 (2014).

[75] Vellekoop, I. M., Lagendijk, A. & Mosk, A. P. Exploiting disorder for perfect focusing. *Nature photonics* **4**, 320–322 (2010).

[76] Vellekoop, I. M. Feedback-based wavefront shaping. *Optics Express* **23**, 12189 (2015).

[77] Vellekoop, I. M. & Aegerter, C. M. Scattered light fluorescence microscopy: imaging through turbid layers. *Optics letters* **35**, 1245–1247 (2010).

[78] Hsieh, C.-L., Pu, Y., Grange, R., Laporte, G. & Psaltis, D. Imaging through turbid layers by scanning the phase conjugated second harmonic radiation from a nanoparticle. *Optics express* **18**, 20723–20731 (2010).

[79] Van Putten, E. G. *et al.* Scattering Lens Resolves Sub-100 nm Structures with Visible Light. *Physical Review Letters* **106**, 193905 (2011).

[80] Yang, X., Hsieh, C.-L., Pu, Y. & Psaltis, D. Three-dimensional scanning microscopy through thin turbid media. *Optics Express* **20**, 2500 (2012).

[81] Ghielmetti, G. & Aegerter, C. M. Scattered light fluorescence microscopy in three dimensions Abstract. *Optics Express* **20**, 110–115 (2012).

[82] Freund, I., Rosenbluh, M. & Feng, S. Memory effects in propagation of optical waves through disordered media. *Physical Review Letters* **61**, 2328–2331 (1988).

[83] Vellekoop, I. & Mosk, A. P. Universal Optimal Transmission of Light Through Disordered Materials. *Physical Review Letters* **101**, 120601 (2008).

[84] Cuche, E., Marquet, P. & Depeursinge, C. Spatial filtering for zero-order and twin-image elimination in digital off-axis holography. *Applied optics* **39**, 4070–5 (2000).

[85] Lin, J. Y., Lin, M. Z., Steinbach, P. & Tsien, R. Y. Characterization of Engineered Channelrhodopsin Variants with Improved Properties and Kinetics. *Biophysical Journal* **96**, 1803–1814 (2009).

[86] Jang, M., Sentenac, A. & Yang, C. Optical phase conjugation (OPC)-assisted isotropic focusing. *Optics Express* **21**, 8781 (2013).

[87] Booth, M. J., Neil, M. A. A., Juskaitis, R. & Wilson, T. Adaptive aberration correction in a confocal microscope. *Proceedings of the National Academy of Sciences of the United States of America* **99**, 5788–5792 (2002).

[88] Chung, K. *et al.* Structural and molecular interrogation of intact biological systems. *Nature* **497**, 332–337 (2013).

[89] Deisseroth, K. Optogenetics. *Nature Methods* **8**, 26–29 (2011).

[90] Wang, K. *et al.* Rapid adaptive optical recovery of optimal resolution over large volumes. *Nature Methods* **11**, 625–628 (2014).

[91] Jang, M., Ruan, H., Zhou, H., Judkewitz, B. & Yang, C. Method for auto-alignment of digital optical phase conjugation systems based on digital propagation. *Optics Express* **22**, 14054 (2014).

[92] Ntziachristos, V. Going deeper than microscopy: the optical imaging frontier in biology. *Nature methods* **7**, 603–14 (2010).

[93] Xu, X., Liu, H. & Wang, L. V. Time-reversed ultrasonically encoded optical focusing into scattering media. *Nature Photonics* **5**, 154–157 (2011).

[94] Si, K., Fiolka, R. & Cui, M. Fluorescence imaging beyond the ballistic regime by ultrasound-pulse-guided digital phase conjugation. *Nature photonics* **6**, 657–661 (2012).

[95] Si, K., Fiolka, R. & Cui, M. Breaking the spatial resolution barrier via iterative sound-light interaction in deep tissue microscopy. *Scientific reports* **2**, 748 (2012).

[96] Wang, L. Mechanisms of Ultrasonic Modulation of Multiply Scattered Coherent Light: An Analytic Model. *Physical Review Letters* **87**, 043903 (2001).

[97] Laser Institute of America. *American National Standard for Safe Use of Lasers ANSI Z136.1-2000* (American National Standards Institute Inc., New York, 2000).

[98] Vellekoop, I. M. & Aegerter, C. M. Focusing light through living tissue. In Izatt, J. A., Fujimoto, J. G. & Tuchin, V. V. (eds.) *Proceedings of SPIE*, vol. 7554, 755430 (2010).

[99] Conkey, D., Caravaca-Aguirre, A. & Piestun, R. High-speed scattering medium characterization with application to focusing light through turbid media. *Optics express* **20**, 1733–40 (2012).

[100] Marquez, G., Wang, L. V., Lin, S. P., Schwartz, J. a. & Thomsen, S. L. Anisotropy in the absorption and scattering spectra of chicken breast tissue. *Applied optics* **37**, 798–804 (1998).

[101] Dalecki, D. Mechanical bioeffects of ultrasound. *Annual review of biomedical engineering* **6**, 229–48 (2004).

[102] U.S. Department of Health and Human Services. Guidance for Industry and FDA StaffInformation for Manufacturers Seeking Marketing Clearance of Diagnostic Ultrasound Systems and Transducers (2008).

[103] Martelli, F., Bianco, S. D., Ismaelli, A. & Zaccanti, G. *Light propagation through biological tissue and other diffusive media: theory, solutions, and software* (Bellingham: SPIE Press, 2010). URL `http://ebooks.spiedigitallibrary.org/book.aspx?bookid=83`.

[104] Haskell, R., Svaasand, L. & Tsay, T. Boundary conditions for the diffusion equation in radiative transfer. *JOSA A* **11**, 2727–41 (1994).

[105] Riley, W. & Klein, W. Piezo Optic Coefficients of Liquids. *The Journal of the Acoustical Society of America* **42**, 1258–1261 (1967).

[106] Moharam, M., Gaylord, T. & Magnusson, R. Criteria for Raman-Nath regime diffraction by phase gratings. *Optics Communications* **32**, 19–23 (1980).

[107] Gaylord, T. & Moharam, M. Thin and thick gratings: terminology clarification. *Applied Optics* 3271–3273 (1981).

[108] Huang, J., Nissen, J. a. & Bodegom, E. Diffraction of light by a focused ultrasonic wave. *Journal of Applied Physics* **71**, 70–75 (1992).

[109] Culjat, M. O., Goldenberg, D., Tewari, P. & Singh, R. S. A review of tissue substitutes for ultrasound imaging. *Ultrasound in medicine & biology* **36**, 861–73 (2010).

[110] Chaigne, T. *et al.* Controlling light in scattering media non-invasively using the photoacoustic transmission matrix. *Nature Photonics* **8**, 58–64 (2014).

[111] Hsieh, C., Pu, Y., Grange, R. & Psaltis, D. Digital phase conjugation of second harmonic radiation emitted by nanoparticles in turbid media. *Optics Express* **18**, 533–537 (2010).

[112] Tay, J. W., Lai, P., Suzuki, Y. & Wang, L. V. Ultrasonically encoded wavefront shaping for focusing into random media. *Scientific reports* **4**, 3918 (2014).

[113] Suzuki, Y., Xu, X., Lai, P. & Wang, L. V. Energy enhancement in time-reversed ultrasonically encoded optical focusing using a photorefractive polymer. *Journal of biomedical optics* **17**, 805071–805073 (2012).

[114] Jang, M., Ruan, H., Judkewitz, B. & Yang, C. Model for estimating the penetration depth limit of the time-reversed ultrasonically encoded optical focusing technique. *Optics express* **22**, 5787–807 (2014).

[115] Lai, P., Xu, X., Liu, H., Suzuki, Y. & Wang, L. V. Reflection-mode time-reversed ultrasonically encoded optical focusing into turbid media. *Journal of Biomedical Optics* **16**, 80505 (2011).

[116] Suzuki, Y., Tay, J. W., Yang, Q. & Wang, L. V. Continuous scanning of a time-reversed ultrasonically encoded optical focus by reflection-mode digital phase conjugation. *Optics letters* **39**, 3441–4 (2014).

[117] Kim, M., Choi, W., Choi, Y., Yoon, C. & Choi, W. Transmission matrix of a scattering medium and its applications in biophotonics. *Optics express* **23**, 12648–12668 (2015).

[118] Yu, H. *et al.* Recent advances in wavefront shaping techniques for biomedical applications. *Current Applied Physics* **15**, 632–641 (2015).

[119] Papadopoulos, I. N., Farahi, S., Moser, C. & Psaltis, D. Focusing and scanning light through a multimode optical fiber using digital phase conjugation. *Optics express* **20**, 10583–10590 (2012).

[120] Hillman, T. R. *et al.* Digital optical phase conjugation for delivering two-dimensional images through turbid media. *Scientific reports* **3** (2013).

[121] Wang, D. *et al.* Focusing through dynamic tissue with millisecond digital optical phase conjugation. *Optica* **2**, 728–735 (2015).

[122] Lee, K., Lee, J., Park, J.-H., Park, J.-H. & Park, Y. One-wave optical phase conjugation mirror by actively coupling arbitrary light fields into a single-mode reflector. *Physical review letters* **115**, 153902 (2015).

[123] Yu, H. *et al.* Measuring large optical transmission matrices of disordered media. *Physical review letters* **111**, 153902 (2013).

[124] Vellekoop, I. M., Cui, M. & Yang, C. Digital optical phase conjugation of fluorescence in turbid tissue. *Applied physics letters* **101**, 81108 (2012).

[125] Katz, O., Small, E., Guan, Y. & Silberberg, Y. Noninvasive nonlinear focusing and imaging through strongly scattering turbid layers. *Optica* **1**, 170 (2014).

[126] Zhou, E. H., Ruan, H., Yang, C. & Judkewitz, B. Focusing on moving targets through scattering samples. *Optica* **1**, 227 (2014).

[127] Ma, C., Xu, X., Liu, Y. & Wang, L. V. Time-reversed adapted-perturbation (TRAP) optical focusing onto dynamic objects inside scattering media. *Nature Photonics* **8**, 931–936 (2014).

[128] Kong, F. *et al.* Photoacoustic-guided convergence of light through optically diffusive media. *Optics letters* **36**, 2053–5 (2011).

[129] Caravaca-Aguirre, A. M. *et al.* High contrast three-dimensional photoacoustic imaging through scattering media by localized optical fluence enhancement. *Optics Express* **21**, 26671 (2013).

[130] Lai, P., Wang, L., Tay, J. W. & Wang, L. V. Photoacoustically guided wavefront shaping for enhanced optical focusing in scattering media. *Nature Photonics* **9**, 126–132 (2015).

[131] Kothapalli, S.-R. & Wang, L. V. Ultrasound-modulated optical microscopy. *Journal of biomedical optics* **13**, 54046 (2008).

[132] Ruan, H., Jang, M., Judkewitz, B. & Yang, C. Iterative time-reversed ultrasonically encoded light focusing in backscattering mode. *Scientific reports* **4**, 7156 (2014).

[133] Lindner, J. R. Microbubbles in medical imaging : current applications and future directions **3**, 527–532 (2004).

[134] Goertz, D. E. *et al.* High frequency nonlinear B-scan imaging of microbubble contrast agents. *Ultrasonics, Ferroelectrics, and Frequency Control, IEEE Transactions on* **52**, 65–79 (2005).

[135] Viessmann, O. M., Eckersley, R. J., Christensen-Jeffries, K., Tang, M. X. & Dunsby, C. Acoustic super-resolution with ultrasound and microbubbles. *Physics in medicine and biology* **58**, 6447 (2013).

[136] O'Reilly, M. A. & Hynynen, K. A super-resolution ultrasound method for brain vascular mapping. *Medical physics* **40**, 110701 (2013).

[137] Desailly, Y., Couture, O., Fink, M. & Tanter, M. Sono-activated ultrasound localization microscopy. *Applied Physics Letters* **103**, 174107 (2013).

[138] Benchimol, M. J. *et al.* Phospholipid/Carbocyanine Dye-Shelled Microbubbles as Ultrasound-Modulated Fluorescent Contrast Agents. *Soft matter* **9**, 2384–2388 (2013).

[139] Liu, Y., Feshitan, J. A., Wei, M.-Y., Borden, M. A. & Yuan, B. Ultrasound-modulated fluorescence based on fluorescent microbubbles. *Journal of biomedical optics* **19**, 085005 (2014).

[140] Ruan, H., Mather, M. L. & Morgan, S. P. Ultrasound modulated optical tomography contrast enhancement with non-linear oscillation of microbubbles. *Quantitative imaging in medicine and surgery* **5**, 9–16 (2015).

[141] Shekhar, H., Rychak, J. J. & Doyley, M. M. Modifying the size distribution of microbubble contrast agents for high-frequency subharmonic imaging. *Medical physics* **40**, 82903 (2013).

[142] Pancholi, K. P., Farook, U., Moaleji, R., Stride, E. & Edirisinghe, M. J. Novel methods for preparing phospholipid coated microbubbles. *European biophysics journal : EBJ* **37**, 515–20 (2008).

[143] Palanchon, P., Klein, J. & de Jong, N. Production of standardized air bubbles: Application to embolism studies. *Review of scientific instruments* **74**, 2558–2563 (2003).

[144] Chomas, J. E., Dayton, P., Allen, J., Morgan, K. & Ferrara, K. W. Mechanisms of contrast agent destruction. *IEEE transactions on ultrasonics, ferroelectrics, and frequency control* **48**, 232–48 (2001).

[145] Thomas, D. H., Sboros, V., Emmer, M., Vos, H. & De Jong, N. Microbubble oscillations in capillary tubes. *Ultrasonics, Ferroelectrics, and Frequency Control, IEEE Transactions on* **60** (2013).

[146] Jang, M. *et al.* Relation between speckle decorrelation and optical phase conjugation (OPC)-based turbidity suppression through dynamic scattering media: a study on in vivo mouse skin. *Biomedical optics express* **6**, 72–85 (2015).

[147] Ma, C., Zhou, F., Liu, Y. & Wang, L. V. Single-exposure optical focusing inside scattering media using binarized time-reversed adapted perturbation. *Optica* **2**, 869–876 (2015).

[148] Ferrara, K., Pollard, R. & Borden, M. Ultrasound microbubble contrast agents: fundamentals and application to gene and drug delivery. *Biomedical Engineering* **9** (2007).

[149] Shapiro, M. G. *et al.* Biogenic gas nanostructures as ultrasonic molecular reporters. *Nature nanotechnology* **9**, 311–6 (2014).

[150] El-Sayed, I. H., Huang, X. & El-Sayed, M. A. Selective laser photo-thermal therapy of epithelial carcinoma using anti-EGFR antibody conjugated gold nanoparticles. *Cancer letters* **239**, 129–35 (2006).

[151] Schnarr, K. *et al.* Gold Nanoparticle-Loaded Neural Stem Cells for Photothermal Ablation of Cancer. *Advanced healthcare materials* **2**, 976–982 (2013).

[152] Gradinaru, V., Mogri, M., Thompson, K. R., Henderson, J. M. & Deisseroth, K. Optical deconstruction of parkinsonian neural circuitry. *Science (New York, N.Y.)* **324**, 354–9 (2009).

[153] Judkewitz, B., Horstmeyer, R., Vellekoop, I. M., Papadopoulos, I. N. & Yang, C. Translation correlations in anisotropically scattering media. *Nature Physics* 1–6 (2015). arXiv:`1411.7157`.

[154] Ruan, H., Mather, M. L. & Morgan, S. P. Pulsed ultrasound modulated optical tomography with harmonic lock-in holography detection. *JOSA A* **30**, 1409–1416 (2013).

[155] Ruan, H., Mather, M. L. & Morgan, S. P. Pulsed ultrasound modulated optical tomography utilizing the harmonic response of lock-in detection. *Applied optics* **52**, 4755–4762 (2013).

[156] Chen, D. & McGough, R. J. A 2D fast near-field method for calculating near-field pressures generated by apodized rectangular pistons. *The Journal of the Acoustical Society of America* **124**, 1526–37 (2008).

[157] Raum, K., Brien, W. & Others. Pulse-echo field distribution measurement technique for high-frequency ultrasound sources. *Ultrasonics, Ferroelectrics, and Frequency Control, IEEE Transactions on* **44**, 810–815 (1997).

[158] Viasnoff, V., Lequeux, F. & Pine, D. J. Multispeckle diffusing-wave spectroscopy: A tool to study slow relaxation and time-dependent dynamics. *Review of Scientific Instruments* **73**, 2336 (2002).

[159] Lemieux, P. & Durian, D. J. Investigating non-Gaussian scattering processes by using n th-order intensity correlation functions. *JOSA A* **16**, 1651–1664 (1999).

[160] Flock, S. T., Jacques, S. L., Wilson, B. C., Star, W. M. & van Gemert, M. J. Optical properties of Intralipid: a phantom medium for light propagation studies. *Lasers in surgery and medicine* **12**, 510–9 (1992).

[161] Samatham, R., Jacques, S. L. & Campagnola, P. Optical properties of mutant versus wild-type mouse skin measured by reflectance-mode confocal scanning laser microscopy (rCSLM). *Journal of biomedical optics* **13**, 041309 (2014).

[162] Jacques, S. L. Optical properties of biological tissues: a review. *Physics in medicine and biology* **58**, R37–61 (2013).

[163] Krege, J. H., Hodgin, J. B., Hagaman, J. R. & Smithies, O. A Noninvasive Computerized Tail-Cuff System for Measuring Blood Pressure in Mice. *Hypertension* **25**, 1111–1115 (1995).

[164] Pine, D., Weitz, D., Chaikin, P. & Herbolzheimer, E. Diffusing wave spectroscopy. *Physical Review Letters* **60** (1988).

[165] Ewald, A., Werb, Z. & Egeblad, M. Monitoring of vital signs for long-term survival of mice under anesthesia. *Cold Spring Harbor Protocols* **2011** (2011).

[166] Laforest, T. & Dupret, A. A 4000 Hz CMOS image sensor with in-pixel processing for light measurement and modulation. *New Circuits and Systems Conference, IEEE 11th International* 1–4 (2013).